UNIVERSITY OF LIVERPOOL

Department Of Engineering

PhD Thesis

A Predictive Thermal Dynamic Model for Parameter Generation in the Laser Assisted Direct Write Process

Thesis submitted in accordance with the requirements of the University of Liverpool for the degree of Doctor in Philosophy

By

Shuo Shang

2012

Declaration

I hereby declare that this submission is my own work and that, to the best of my knowledge and belief, it contains no material previously published or written by another person nor material which to a substantial extent has been accepted for the award of any other degree or diploma of the University or other institute of higher learning, except where due acknowledgment has been made in the text:

Signature…………………………………………………………………………………………………

Name: Shuo Shang……………………………………………………………………………

Date: Friday 17th August 2012…………………………………………………………………

Abstract

The Laser Assisted Direct Write (LADW) method can be used to generate electrical circuitry on a substrate by depositing metallic ink and curing the ink thermally by a laser. Laser curing has emerged over recent years as a novel yet efficient alternative to oven curing. This method can be used in-situ, over complicated 3D contours of large parts (eg. aircraft wings) and selectively cure over heat sensitive substrates, with little or no thermal damage.

In previous studies, empirical methods have been used to generate processing windows for this technique, relating to the several interdependent processing parameters on which the curing quality and efficiency strongly depend. Incorrect parameters can result a track that is cured in some areas and uncured in others, or in damaged substrates. This thesis addresses the strong need for a quantitative model which can systematically output the processing conditions for a given combination of ink, substrate and laser source; transforming the LADW technique from a purely empirical approach, to a simple, repeatable, mathematically sound, efficient and predictable process.

This thesis describes in detail a novel and generic Finite Element Method (FEM) model that for the first time predicts the evolution of the thermal profile of the ink track during laser curing and thus generates a parametric map which indicates the most suitable combination of parameters for process optimisation. Experimental data is compared with simulation results to verify the accuracy of the model.

This study also theoretically and experimentally investigates the curing process under different intensity profiles obtained with the SunShaper, a novel beam shaping device invented by Dr Wellburn, and thus predicts the performance of curing with various circular shaped beams.

Acknowledgements

The Author would like to express gratitude to the following people for assistance during the course of completing this thesis:

To my PhD supervisors Professor Ken Watkins and Dr Geoff Dearden for the numerous helpful discussions, constructive criticism, guidance and enthusiasm which made the experience successful and enjoyable.

To Dr Eamonn Fearon for suggestions and ideas which had a major effect on the direction of the work presented in this thesis. To Dr Dan Wellburn, who invented the SunShaper beam shaping device, for his assistance and support. To Dr Taku Sato whose previous study inspired a lot of work presented in this thesis.

To all the staff at Lairdside Laser Engineering Centre particularly Dr Stuart Edwardson and Doug Eckford for practical help of all kinds.

To Dr Robin Pittson and Dr Nina Biddle at Gwent Electronics group（GEM）for providing the inks that are used in this study.

To Dr Andrew Fogg for his assistance on utilising the STA instruments in the Department of Chemistry, University of Liverpool.

Finally to my family and friends who have been a constant source of support throughout.

List of Publications to Date

The Author has published the following two academic papers to date, in:

Journal of Physics D: Applied Physics

A predictive thermal dynamic model for parameter generation in the laser assisted direct write process

Shuo Shang, Eamonn Fearon, Dan Wellburn, Taku Sato, Stuart Edwardson, G Dearden and K G Watkins

2011 J. Phys. D: Appl. Phys. 44 435301

(http://iopscience.iop.org/0022-3727/44/43/435301)

Optics and Lasers in Engineering

Laser Assisted Direct Write Process with Novel Beam Profiles

Shuo Shang, Eamonn Fearon, Dan Wellburn, Shilian Yan, Stuart Edwardson, G Dearden and K G Watkins

DOI information: 10.1016/j.optlaseng.2012.11.005

Symbols and Notations

I [Wm^{-2}], laser intensity

I_0 [Wm^{-2}], the peak intensity at the centre of a Gaussian laser beam

[m], is the beam waist

r [m], is the distance away from the centre of the beam

P [W], is the power of laser

Q [J], the total energy required to cure unit volume of ink from room temperature

Q_i [J], energy required for a particular stage in a curing process

$_s$ [kgm^{-3}], solvent density

M_a, the molar mass of ethanol

N_A, the Avogadro constant.

C_p [$Jkg^{-1} K^{-1}$], is the heat capacity

k [$W \cdot m^{-1} \cdot K^{-1}$], thermal conductivity

T [K], local temperature on the sample

[$5.670373(21) \times 10^{-8}$ W m^{-2} K^{-4}], the Stefan-Boltzmann constant

is the emissivity

V [m^3], unit volume on the sample

I_n [10^6 Wm^{-3}], normalised Intensity of laser , defined as the average laser intensity per micron

H [m], thickness of the ink track

R [m], half track width

Pe, Peclet number

[$m^2 s$], thermal diffusivity of material

T_c [K], curing temperature

T_{ov} [K], the overcuring temperature

k_{D1}, k_C, k_{D58} and k_{Ag}, [Wm^{-1}K^{-1}], the thermal conductivity of cured D1 ink, pure graphite, cured D58 ink and silver, respectively

H_i, [Wm^{-2}], total heat flux

t [S], time of the process,

T [K], temperature increment

m [kg], sample mass

List of Abbreviations

DW: Direct Write

LADW: Laser Assisted Direct Write

FEM: Finite element Method

STA: Scanning Thermal Analysis

TGA: Thermo Gravimetric Analysis

DSC: Differential Scanning Calorimetry

PLD: Pulsed Laser Deposition

MAPLE: Matrix Assisted Pulsed Laser Evaporation

FIB: Focused Ion Beam

LIFT: Laser Induced Forward Transfer

SLS: Selective Laser Sintering

RLC: Resistance-Inductance-Capacity

CNC: Computer Numerically Controlled

PET: Polyethylene Terephthalate

CFC: Carbon Fire Composites

Table of Content

0. Introduction

As technology progresses, there is a tendency and requirement for electronics to become smaller, cheaper and more reliable. Further to this, in an energy conscious environment there is a desire for more efficient ways of manufacturing components with less material waste and shorter life cycles.

Direct Write (DW) process is able to fabricate components of different geometries and materials, from tissue scaffolds for cells to ceramics and piezoelectric materials. There is extensive growth in the area of DW research with numerous commercially available systems already in industrial usage. With the advent and growth of DW, there is a desire within industry for the development of these processes to be used to fabricate functional components for real world solutions. With many technologies each with their own merit, no single technology has become the sole solution for all fabrication needs.

Many DW processes were already well established before industrial lasers became ready. They are generally relatively easy to operate and are suitable for large quantity batch production. However some of such methods lack flexibility, therefore are unsuitable for prototyping or low volume manufacture. Also, the usage of volatile chemicals involved in some cases has strong negative environmental impacts.

A laser has the ability to direct variable amounts of energy precisely to where it is needed in a controllable way. Different types of lasers have been developed with new types constantly being introduced. Applications of lasers have been found in countless fields.

The Laser Assisted Direct Write (LADW) process is an additive deposition process which uses laser energy to thermally cure a pre-deposited conductive ink track pattern on a substrate.

As a potential substitution to photolithography, LADW technology has received attention in recent years for its wide range of applicability in modern electronics. LADW allows printing of various patterns without employing a mask or a resist. Deposition speed is enhanced with CNC integration. LADW has some advantages over conventional ink-jet methods, in that it is able to use higher viscosity liquids containing various sizes of micro particles. In a typical LADW process, ink is precisely deposited onto a substrate; the sample is then cured either in an oven, or by laser irradiation along the ink track. The potential uses of this technology cover applications in solar cells, Radio Frequency Identification-tags (RFID-tags), flexible-

electronics, Organic Light Emitting Diodes (OLED) displays, antenna, biological uses and many more.

However, there are a number of barriers to be overcome before Laser Assisted Direct Write can be fully implemented in the commercial arena:

1) Manufacture of conductive inks which are optimised for laser curing.
2) Reliably achieving efficient laser curing with satisfactory conductivity, and acceptable adhesion to the substrates.

One key technical aspect of LADW is the conductive ink used. A conductive ink is typically a fluid loaded with metallic (eg, silver) micro particles that have been fully suspended in resin. Solvent is added to reduce viscosity for printing. Once deposited, the solvent is evaporated by heating to leave a thin film of micro particles in resin. The composite is then further heated to a higher temperature at which the resin starts to cross-link, and hence reduce in volume. The silver particles are then closely packed together, yielding electrical conductivity. Traditionally, ovens are used to cure the deposited ink.

Another key factor of LADW is the mode of laser beam. A Gaussian beam intensity profile has been most commonly used for LADW. However, a Gaussian intensity distribution is not capable of providing uniform surface heat treatment desired by many laser processes, due to the large disparity between the intensity at the centre of the Gaussian beam and that at its outside edge.

The Novel beam shaping device designed by Wellburn is a dynamic possessing head capable of tuning the output intensity profile and/or beam geometry, with virtually no loss of input power. It converts a CO_2 laser beam of the Gaussian mode into a plateau filled annular ring shape, the relative level of plateau fill can be easily varied by calibrated manual adjustment of the device. The flexible beam profiles produced by the beam shaper enable study of process optimisation for a wide range of laser surface heat treatments.

Remarkable advances have been made regarding the manufacture of inks while much less study has been done on the development of a non-oven method of curing.

This study focuses on the construction of a predictive Finite Element Method (FEM) model for LADW in the COMSOL 4.0 environment. This model is proposed for efficient simulation of the curing process for different substrate/ink combinations, taking into account the properties of the ink, substrate, and laser beam profile, and generates a processing window

which will be useful as a guide to engineers for the optimisation of the process. Close approximation is made to generate an indicative parametric map which is validated with experimental results.

This model simulates the temperature evolution of the sample during the process. The results can be used to predict whether satisfactory curing has been achieved and thus indicate the suitability of the combination of curing parameters used. Laser intensity profiles can be defined in the model as analytical functions, or imported as interpolation functions, and one can therefore predict the optimised beam mode by running the model.

Experimental validations of simulation results have been performed in this study, along with comparisons of the results obtained by others.

1. Literature review

This chapter presents a literature review for the topic of study. The first part is intended to inform the reader of the current state of the art of technology used under the umbrella term õDirect Writeö, focusing on the LADW technology. This is followed by the second part which briefly introduces the background of Finite Element Method for mathematical modelling, which is a critical part of this thesis.

1.1 Overview of Direct Write technology and the purpose of this study

Additive manufacturing, for which Direct Write (DW) is a sub-category, is a well suited manufacturing tool. In general it allows for low material wastage and ease of modification. Due to its computer controlled nature, different designs can be easily made with just a change in programming and no requirement for hard tooling [1-8]. With no single dominant process, it is likely that several will emerge as the process of choice for any single component manufacturing process [10-17].

This overview is split into two sections. The first section broadly introduces commonly used õnon-laser basedö and õlaser basedö DW techniques. The second section focuses on Laser Assisted Direct Write and previous work that has been done in this particular field.

1.1.1 DW Technologies and their applications

This chapter firstly discusses the applications and potential of DW, starting with non-laser based additive manufacturing technologies and followed by principle of lasers and laser based DW technologies.

1.1.1.1 Applications of DW technology and need for research in this area

The term direct write (DW) is a general umbrella term for a range of flexible multi-scale, CAD/CAM controlled fabrication technologies which largely involve ÷point of processø deposition and which can be used to produce 2D and/or 3D structures on pre-existing substrates for a wide range of materials [22-25]. They can be used to form simple 2D components or complex 3D architectures on curved surfaces.

Though there are many technologies encompassed within Direct Write, an effort has been

made to restrict the scope of this review to the generation of electrically significant components on 3D substrates with no damage to the substrate. For example, sensors or electrical components in metallic parts [13, 16, 26-35]. Some technologies are included which may be of use in relatively large scale deposition of a desired set of materials, though these may require some finishing processes. These are included due to the higher deposition rates which may be useful in conjunction with the more accurate systems and for completeness.

1.1.1.2 Non-laser based DW technologies

Many DW processes were already well established before industrial lasers became ready in the 1980s. These methods all involve flow and chemical processes in some way. They are generally relatively easy to operate (do not require staff to be trained in the laser optics), and are suitable for large quantity batch production.

1.1.1.2.1 Syringe based technologies

The advantage of syringe deposition is the ability to conformally deposit a desired ink over a surface and its capability of coping with a wide range of viscosity. Flow-based DW requires high precision micro-dispensing technology which could be in the form of a precise pneumatic pump or an extrusion process. A precision instrument that enables deposition of liquid droplets spanning from 2 nano litre to 300 micro litre has been developed utilizing piezoelectric actuators for volume control [36-40]. The material delivered is through a very small orifice of a needle, restricting the size of the particles that can populate a composite ink. In practice, for syringe deposition the particles are of the order tens of microns as a maximum and recently common inks often employ nano particulates. This kind of DW system is able to cope with materials over a wide range of viscosity from 0.5 to 1,000,000 cp. Unlike inkjet process, where the ink is discretised as individual droplets, the delivery of material for flow-based DW is in the form of continuous filaments, as shown in Fig 1.1.1
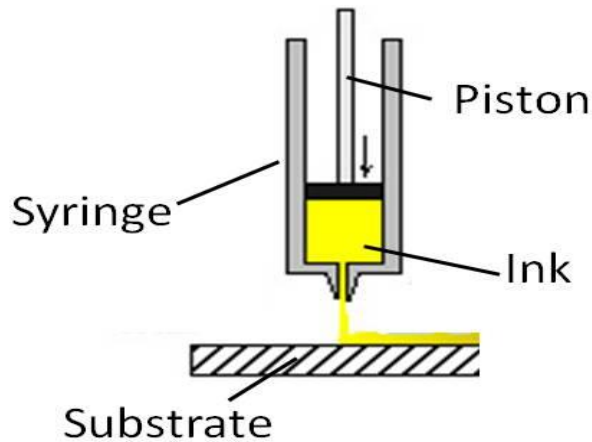
Figure 1.1.1: Illustration of the Syringe deposition method [37].

Common components that are fabricated using this type of technology include conductive lines, resistors, antenna and 3D polymeric structures [41], where line widths down to 25 m have been demonstrated. Conventionally, post curing in an oven is required. This technique is also extensively used in the biochemical field for 3D tissue engineering with cells.

1.1.1.2.2 Inkjet technology

Inkjet technologies for the deposition of sensors have evolved from printing technologies and can create multilayer systems by the deposition of inks containing colloids, nanoparticles, organometallics or organic compounds (including viable cells) [42-47]. Inkjet technologies can be separated into two broad classes based on how the ink is delivered, whether it is delivered in a continuous stream (filamentary approach) or in a series of discrete droplets (the more common technique) [48]. One of the most important considerations is the properties of the ink itself, which must have the required viscosity, shear stress and viscoelasticity for the relevant process ó especially in the case of self-supporting structures. An extra consideration when printing on hard (i.e. non-absorbent) surfaces is that the drying of the ink relies entirely on solvent evaporation. However, the emergence of UV-curable inks has obviated this problem to a certain extent [49-54].

Discrete droplet systems rely upon low-dilution (<5% solids by volume), low-viscosity inks (typically 2cp but can be up to 100cp) which will form consistent droplet sizes [54]. A feature of these low-viscosity inks is their propensity to spread on contact with the substrate, forming tracks with a very low ratio of height to width. Filamentary systems can utilise inks with

much higher concentrations of solute and higher viscoelastic properties, allowing the generation of high-aspect ratio 3-D structures. This is because they do not require the formation of a drop to occur which is dependent on the surface tension and viscosity of the fluid, and so can tolerate a larger range of ink properties compared to drop on demand. Drop on demand has very specific property requirements as the viscoelastic nature of the fluid determines the snap off of the ligament that is formed during drop formation. This ligament needs to break away from the droplet and re-coalesce in to the nozzle so that satellite droplets are not formed [55-57].

Metallic paths can be printed by using a metal precursor which can be subsequently treated to convert it to the pure metal. Silver and copper electrodes have been printed using this technique. Ceramics can also be inkjet printed, either directly with particles in solution (to be subsequently sintered) or by printing a binder on pre-placed ceramic particles. The latter method is more commonly used to make ceramic moulds for casting.
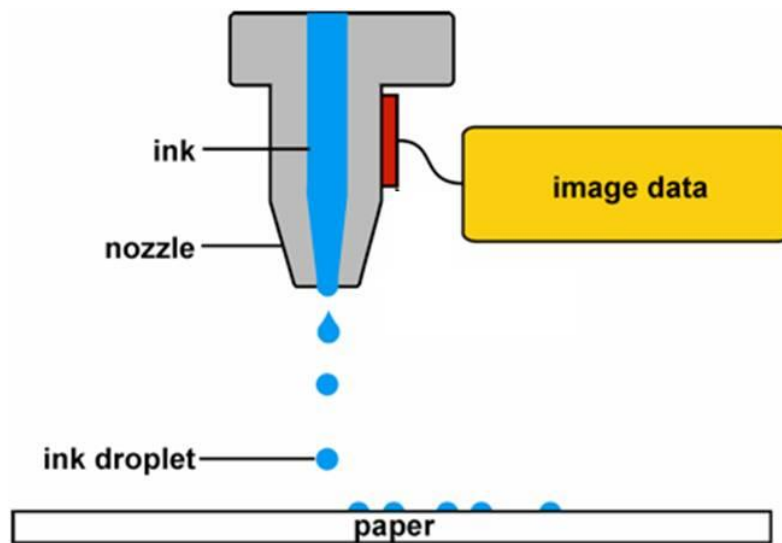
Figure 1.1.2: Illustration of the inkjet nozzle jetting, using drop on demand technique [50].

In general for the fabrication of electrical components, the inkjet heads use a piezoelectric orifice that squeezes or jets the ink out. A discrete droplet is formed in this manner. Another technique is to thermally heat the ink (no piezoelectric orifice) creating a bubble at the end. This bubble then bursts in a controlled manner and is directed towards the substrate. Thermal ink jet printing has been superseded by piezoelectric ink jets due to the inability of thermal inkjet heads to deposit volatile solvents, placing limitations upon the types of materials that can be deposited [34-36, 58, 59].

In general, inkjet printing can create very high aspect ratio lines, with drop sizes on the substrate about 80 m across with a 30 m diameter orifice and tens of nanometres thick. Several overlaps are required to create a solid line. Another benefit of inkjet printing is the use of multiple heads on any single system to increase deposition rates with hundreds of nozzles jetting at any one time. Inkjet printing is generally limited to flat substrates, or features of 2D patterning on 3D cylindrical substrates due to the nature of the inkjet head.

1.1.1.2.3 Screen printing

Screen printing of films with required electrical properties is an outgrowth of the printing techniques used commercially for cloth and paper. The basic process is to use a mesh screen, parts of which are treated to make it impermeable to an ink. This screen is then placed over the part to be printed and ink drawn across it. The ink passes through the permeable parts of the screen and is thus deposited on the substrate. This method has been in use to produce thick conductive films and circuits since the 1960's [60].

Today, the use of conductive inks and colloidal suspensions allows the deposition of electrical components including piezoelectric ceramics [33], metals, semiconductors [61] and the generation of batteries [62]. Though the thickness of screen printed layers can be controlled to 1-2 microns, the width of deposited features is only accurate to a resolution of approx 100 microns and may need to be post-processed by laser machining or photoresist methods.

Screen printing is a very fast way of producing large batches of similar items on flat thin substrates. It is limited by the mesh that is used and any new design requires a new mesh to be fabricated, making it unsuitable for small batch runs. The component once deposited will also require some form of post treatment to functionalise the ink that was deposited. It is also a wasteful process in that the whole mesh needs to be sufficiently flooded for the ink to permeate through it, while only a small proportion is actually used [33, 61, 63].

1.1.1.2.4 Photolithography

Photolithography is a well-established and widely applied technique for generating high resolution features on a substrate. The process usually involves the following steps:

- Preparation: The substrate wafer is initially heated and chemically cleaned to drive off any moisture and remove contamination. A liquid or gaseous õadhesion promoter" is applied to promote adhesion of the photoresist to the wafer.

- Photoresist application: The wafer is covered with photoresist by spin coating. A viscous, liquid solution of photoresist is dispensed onto the wafer, and the wafer is spun rapidly to produce a uniformly thick layer. The spin coating typically runs at 1200 to 4800 rpm for 30 to 60 seconds, and produces a layer between 0.5 and 2.5 micrometres thick. The spin coating process results in a uniform thin layer, usually with uniformity of within 5 to 10 nanometres.

- Exposure and developing: A mask is then aligned over the substrate, before exposing to uniform UV illumination [7, 64, 65]. The exposure to light causes a chemical change that allows some of the photoresist to be removed by a special solution, called "developer". Positive photoresist, the most common type, becomes soluble in the developer when exposed. With negative photoresist, unexposed regions are soluble in the developer Fig 1.1.3 [66]. This procedure can be used to generate patterns on variously coated surfaces with only one type of photo resist and mask.

- Etching: In etching, a liquid ("wet") or plasma ("dry") chemical agent removes the uppermost layer of the substrate in the areas that are not protected by photoresist. In semiconductor fabrication, dry etching techniques are generally used, as they can be made anisotropic.

- Photo resist removal: After a photoresist is no longer needed, it must be removed from the substrate. This usually requires a liquid "resist stripper", which chemically alters the resist so that it no longer adheres to the substrate. Alternatively, photoresist may be removed by a plasma containing oxygen, which oxidizes it. This process is called ashing, and resembles dry etching.

Photolithography has been a crucial factor in the continued advance of Mooreøs Law, enabling minimum features sizes in chip manufacturing to shrink from 0.5 micrometer in 1990 to 45 nanometers and below in 2010. This trend is expected to continue into this decade for even denser chips, with minimum features approaching 10 nanometers.

Overview of Align/Expose/Develop Steps
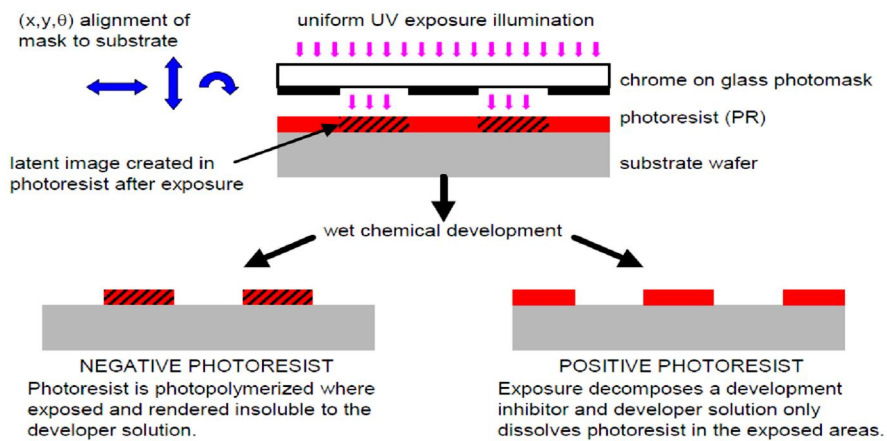
Figure1.1.3: The photolithography technique. [62]

1.1.1.2.5 Thermal spray, Cold gas deposition and Sol-gel

Thermal spray is a process which melts wire, rod or powder feedstock using a flame or plasma arc to produce molten droplets which are then accelerated onto a substrate to form a coating. It has been demonstrated to be capable of producing resolutions on the order of 100 microns [67, 68]. It can be used to deposit metallic, polymeric or ceramic materials. Using this technology researchers have built humidity sensors [67], strain gauges, thermocouples and thermistors on both flat and curved surfaces [12]. This technology can be used on a wide variety of surfaces and has low heat input into the substrate. It can be fully automated and used in conjunction with robotics, increasing the areas in which it can be used, also meaning that it is suitable for small batch quantities and rapid prototyping [12, 69-71].
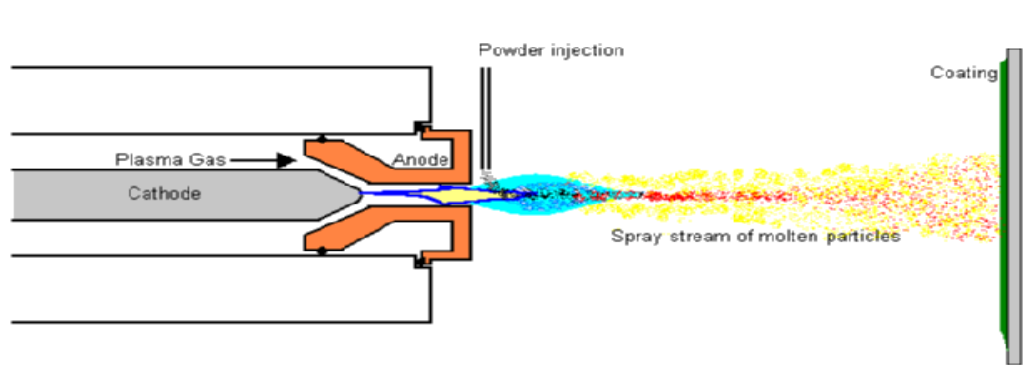
Figure1.1.4: Illustration of the thermal spray process. [64]

Cold gas deposition is an emerging technology whereby particles are accelerated within a supersonic gas stream (typically helium) to impact upon a substrate. Upon impact, their high kinetic energy results in deformation of the particle and bonding with the substrate. This process has been demonstrated for ductile materials including aluminium [72] and other metals [73]. It has the potential to deposit metallic paths on substrates with no heat input and therefore no associated thermal damage to the substrate. Cold gas deposition concentrated upon high deposition rates rather than fine accuracy. The process may produce residual stresses within the deposited material but has oxygen concentrations similar to that of the original powder. Due to the fact that it is not a melting process, reactions between dissimilar materials do not occur and mixed powders can be sprayed to undergo controlled reaction later by heating processes[72-74]. It is not apparent in the literature whether it has been possible to produce the thin films required as a prerequisite of thin film sensor generation.

The sol-gel process used for making ceramic and glass materials involvs a change from a typically colloidal liquid solution "sol" to a solid "gel" phase. Using this method, it is possible to make ultra-fine or spherical shaped powders, thin film coatings, ceramic fibers or microporous inorganic membranes [75-78]. Inorganic or organic metal compounds are firstly made into a colloidal solution which is then spread over a surface to produce thin films or put into a mould to form a gel.

Drying or evaporation then results in a dense ceramic in the required form. Altering the viscosity of a "sol" allows ceramic fibers to be drawn from It [79]. Thin film sensors of interest that have been produced in this manner include chemical and biosensors, strain sensors, actuators [71, 80-82] and moisture sensors.

1.1.1.3 Lasers and their applications

A laser has the ability to direct variable amounts of energy precisely to where it is needed in a controllable way. Many different types have been developed with new types constantly being introduced. The most common types are CO_2 lasers, solid state lasers, fibre lasers, ultrafast lasers, and excimer lasers.

1.1.1.3.1 CO_2 Lasers

Gas lasers are among the most common form in the laser industry. The power levels

range from several kilowatts (carbon dioxide lasers) to milliwatts (heliumóneon lasers). They can be operated in either the continuous mode or pulsed mode, with output frequency ranging from ultraviolet to infrared. As the name implies, gas lasers use a gas as the active medium. Common examples are the He-Ne and CO_2 lasers. Electrical pumping is the most common means of exciting the active medium in gas lasers.

The active medium for the CO_2 laser is a mixture of CO_2, N_2, and He. The CO_2 molecule provides the transitions that generate the laser beam. N_2 helps to increase the population of the upper lasing level, while He helps to depopulate the lower lasing level, thereby enhancing the achievement of population inversion. Since N_2 is a diatomic molecule, it has only one vibrational mode, unlike the CO_2 molecule. Most CO_2 lasers fall into one of the following categories.

Axial Flow Lasers: In a typical axial (longitudinal) flow CO_2 laser, gas mixture is made to flow continuously through the tube along the axis [83].

Transverse flow lasers: In transverse flow lasers, the gas flow, electrical discharge or current flow, and resonator axis are mutually perpendicular to one another. This is because the heat generated within the discharge tube can be more efficiently extracted by flowing the gas at a rate of about 60m/s in a direction normal to the resonator axis. This results in a reduced operating temperature, and under such circumstances, the laser can be operated at higher pressures.

Slab lasers: Slab lasers can have either solid-state or gas-active media [84]. Here, the active medium is excited using two parallel rf-electrodes, which are water cooled. The system is thus said to be diffusion cooled. As a result, the conventional gas circulation systems involving roots blowers or turbines are not required. The use of slab geometry for the active medium enables the beam quality to be significantly improved.

1.1.1.3.2 Excimer Lasers

Excimer lasers are another kind of common gas laser based on the transition of an excited diatomic molecule to a lower energy state where it dissociates into single atoms. The potential energy of a diatomic molecule (dimer) depends on the separation distance between the nuclei centres of the individual atoms [76, 85].

Excimer lasers are useful in applications where ultraviolet output is required. XeCl excimer lasers have been used in laser-assisted chemical vapour deposition for semiconductor manufacture, also photochemical reactions, and photo ablation of polymers, ceramics and glass.

1.1.1.3.3 Solid State lasers

Solid-state lasers normally use an insulating crystal or glass as the host lattice. In it is embedded the active medium, which is either a dopant or an impurity in the host material. The crystal host material does not participate directly in the lasing action, while the dopant does. It is normally a transition metal or rare earth element, and it substitutes for some of the atoms in the host material. The active medium is shaped in the form of a rod, a slab or a disk. Pumping is commonly done using a flash lamp or a diode [86-91].

The active medium temperature may be controlled by circulating air or liquid around it. Otherwise, the heat generated can change the cavity dimensions and consequently, the cavity modes.

Most solid-state lasers generate pulsed beams, even though some generate continuous

wave outputs. Common types of solid-state lasers include the ruby, Nd:YAG and Nd:Glass lasers.

The most recent and significant development in laser technology is the advent of the fibre laser, where the fibre is used as the cavity producing high quality high power beams with the ease of a fibre optic for integration.

Advantages of fibre lasers include the following [92]:

  1. Compact design, since the fibers can be packaged in a coiled configuration. In fact the term õbriefcase laserö has been used to refer to these types of lasers.

  2. High beam quality (diffraction limited) that results from the use of single-mode fiber cores.

  3. Relatively high output efficiency of about 50 % compared to about 10ô30 % for CO_2 and 2 % for lamp pumped Nd:YAG lasers.

1.1.1.3.4 Ultrafast Lasers

The laser systems discussed thus far are capable of generating either continuous wave or pulsed beams with pulse duration of up to hundreds of nanosecond duration by either Q-switching or mode-locking. Shorter laser pulses of duration down to picoseconds and femtoseconds are obtained with ultrafast lasers [93, 94]. These enable much higher peak intensity to be obtained. The output wavelength can be varied with built-in optical crystals. Regardless of the low maximum power (~50W) [93], the high peak intensity and repetition rate make these lasers ideal for micromachining of surface structures.

1.1.1.3.5 Applications of laser technology

Over the past five decades, applications of lasers have been found in countless fields, from medical treatment, to car manufacture; from commercial display to defence related technologies. A laser can be used for welding, cutting, drilling, marking, engraving, and cleaning. In this study, the scope to laser material interaction is limited to creating surface structures.

Applications rely on the coherent and monochromatic nature of a laser. Lasers can be used to create small features on a suitable substrate by using additive, ablative or reactive chemical methods. For fine (<100 micron) features, the shorter wavelength lasers are most commonly used. These include Excimer (193 and 248nm wavelength), frequency doubled or frequency tripled Nd:YAG and high beam quality short-pulse lasers (nanosecond pulsed or lower). With additive processes, lasers can be used to generate 2D and 3D structures at resolutions of tens of microns, whereas laser machining or ablative processes can remove pre-placed materials in defined patterns to a feature resolution of less than half a micron. With some processes, laser machining is used as a final step to remove unwanted material which has been deposited in order to refine the deposited feature to the required dimensions [22, 24, 25, 95-104].

1.1.1.4 Laser based DW

Laser technologies make many new direct write processes possible and economical. A laser could be used to remove unwanted material on a coating through ablation or could be used to create a coating; or to induce chemical reactions within the pre-laid surface ink structure. These applications generally involve state of the art laser systems and deposition facilities. And trained expertise is required to operate such machines. However for many applications there may not be any valid alternatives.

1.1.1.4.1 Laser ablation

A short pulse laser of the order of femtoseconds or picoseconds can be used in a process that is termed ablation or spallation depending on the exact mechanism involved. A constant stream of pulses of a specific wavelength and frequency are incidented upon the material to be removed/deposited, the high peak energy strips off the electrons of the material under irradiation, the remaining positively charged lattice than expels and explodes [68, 71, 105, 106]. This process allows efficient small area precision machining on almost any surface with virtually no heat affected zones, hence also referred to as õcold machiningö [94, 107-109]. Laser micromachining has emerged as one of the most popular way to create a particular

pattern on a coated thin film. The number of applications of this technique is expected to increase considerably in the coming years due to the availability of higher average power lasers and decreasing cost. The throughput of such process can also be potentially improved with new techniques such as beam splitting with the spatial light modulator [94, 107].

1.1.1.4.2 Pulsed laser deposition (PLD and MAPLE)

PLD is a process that uses an off axis pulsed laser to vaporise areas of a sacrificial rotating target such that the resultant plume of evaporated material is deposited upon a facing preplaced substrate. PLD has usually been used to deposit ceramics [110] and semiconductors [111]. It is not suitable for depositing organic or polymeric materials due to the high temperatures and violent mechanism of deposition. Typically it employs UV lasers (usually excimer) and takes place within a hard vacuum, as shown in Fig 1.1.5. PLD is used almost exclusively for the generation of thin films with area coverage, and as a result any component desired would need to be fabricated by post laser-machining or etching of some sort in order to be of use as a functional component. In addition the need for a vacuum chamber would raise problems for the generation of components and would not be suitable for 3D conformal deposition.
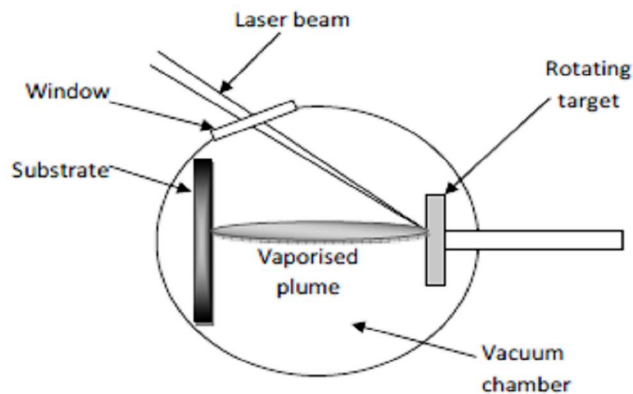
Figure1.1.5: Illustration of the pulsed laser deposition technology [19]

PLD is a popular technique where thin films are required. T. Miller et al [106] describe the fabrication of micro-scale ITO (Indium Tin Oxide) thin film strain sensors using a combination of PLD and focussed ion beam (FIB) machining [19, 106, 110-112].

MAPLE stands for Matrix Assisted Pulsed Laser Evaporation (MAPLE), and is a hybrid technique of PLD for the soft deposition of polymers and organic material, but is not suitable for the deposition of biological materials as they must be frozen within a Matrix [113-115].

In this technique an ultraviolet (excimer) laser pulse is directed at a sacrificial target which consists of a dilute matrix of a specifically chosen solvent and the organic material (solute) to be deposited. The solvent is chosen so that it has a near zero sticking coefficient on the substrate and preferentially absorbs the laser radiation over the organic molecules to be deposited. The matrix is frozen along with the target being rotated in order to reduce the effects of localised heating by successive laser pulses striking the same area and hence reducing the effect of decomposition of the organic molecules.

When the laser beam irradiates the target, the solvent is evaporated, imparting kinetic energy to the released polymer molecules. This effect appears as a plume being ejected from the frozen target. If a substrate is placed in the path of this plume it will be coated with a thin layer of polymer molecules. The gaseous solvent is evacuated from the chamber by means of a pump [19, 113-120].

In order to create any functional geometric components, post processing of the thin film would be required as with PLD. This could be done using a laser or some other subtractive technique. The benefit of MAPLE over PLD is its ability to deposit organic and piezoelectric material without any adverse side effects.

1.1.1.4.3 Laser induced forward transfer (LIFT)

LIFT is a relatively cheap and simple DW manufacturing technique that relies on a disparity between the optical, thermo-physical and mechanical properties of the materials involved. It has been shown to work over a range of laser wavelengths, pulsed and continuous wave (CW). The deposition of metals, oxide compounds and diamond particles have been demonstrated on a variety of substrates [25] in a vacuum, inert and air atmospheres, along with the capability of fabricating precise 3D structures.

The process was first demonstrated by Bohandy et al [121] in the 1980s where it was shown that deposition of Cu and Ag lines of ~50 m in width could be achieved. It is a process which uses a focussed laser to vaporise a thin film which has been placed on a laser transparent medium which acts as a supporting plate; usually quartz but specific to the wavelength used. The laser passes through the transparent medium and impinges upon the film at the thin film/supporting plate interface, where it is absorbed and causes a small portion of the film to vaporise. The vaporised material is expelled away from the supporting plate due to the high pressures that occur during vaporisation, and recondenses upon the substrate, shown in Fig 1.1.6.

Though the amount of material deposited and the achievable resolution is related to the film thickness, laser intensity, wavelength and optical extinction coefficient of the target, the substrate must be held in close proximity to the target so that the vaporised material does not diverge during propagation. Typically the substrate will be between 25 m to 100 m from the target material [122] and this distance is directly proportional to the width of the track deposited as well as the laser fluence employed [123].
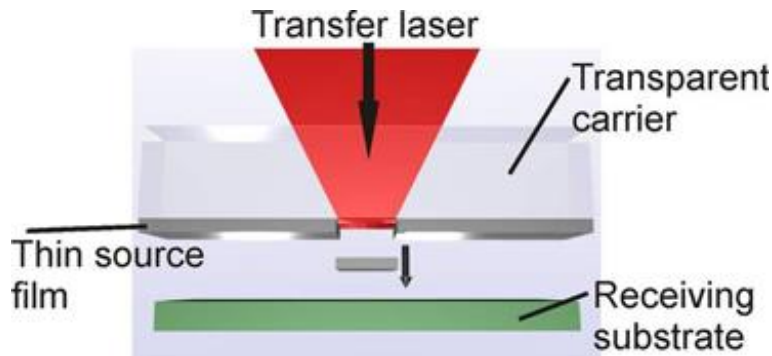
Figure1.1.6: Schematic of a typical LIFT setup. [118]

Because LIFT causes the vaporisation of the transfer material, it is not generally considered to be appropriate for the transfer of polymers, though they may be used as a sacrificial binder in certain applications. It has also been demonstrated that successful deposition of bio molecules such as DNA [124], proteins, prokaryotic and eukaryotic cells[125] has been achieved.

1.1.1.4.4 Selective laser sintering (SLS)

Selective Laser Sintering (SLS) is an extension of the laser cladding process in that it allows 3D parts to be built by sintering successive layers on top of one another in predetermined vector paths. The process utilises a laser beam to create a melt pool on a substrate into which powder is incorporated and subsequently melted. A roller or scraper is used to deposit a thin layer of powder over a piston, and then a laser is used to scan over defined areas, sintering or fusing the powder together, as illustrated in Fig 1.1.7. The piston is then lowered and a new layer of powder deposited to allow the generation of successive layers [126-128].

By repeating the process on top of this generated layer a 3-dimensional part can be made in a layered manufacturing form. Since the layers are fusion bonded to each other, a fully dense metallic part can thus be made. At present, most laser deposited parts need some post-process machining to finish them to required tolerances [129]. The build direction has a significant

effect on part quality, in terms of dimensional error and surface roughness; but no influence on mechanical properties. Table 1.1 [130] gives examples of the commercially available õstate of the artö SLS systems and their capabilities.

Table 1.1: comparison of the capabilities of commercial SLS systems [123]

Machine	EOSINT M250 XTENDED	M3 Linear LASERCUSING
Technology	DMLS	SLM
Laser type	CO_2	Nd:YAG
Power laser [W]	200	107
Wavelength [µm]	10.6	1.080
Material	DS H20	CL 20 (1.4404/AISI 316L)
Building platform [mm]	250×250×185	250×250×250
Preheating platform [°C]	80	n/a
Hatch spacing [mm]	0.2	0.2
O_2 [%]	0.4	0.6–1.2
Environment gas	Nitrogen	Nitrogen

An advantage of this process is that overhanging structures can be built, as the unsintered powder acts as support. Any powder capable of being melted can be used in this process and multimode powders can be used to allow high densities to be achieved.
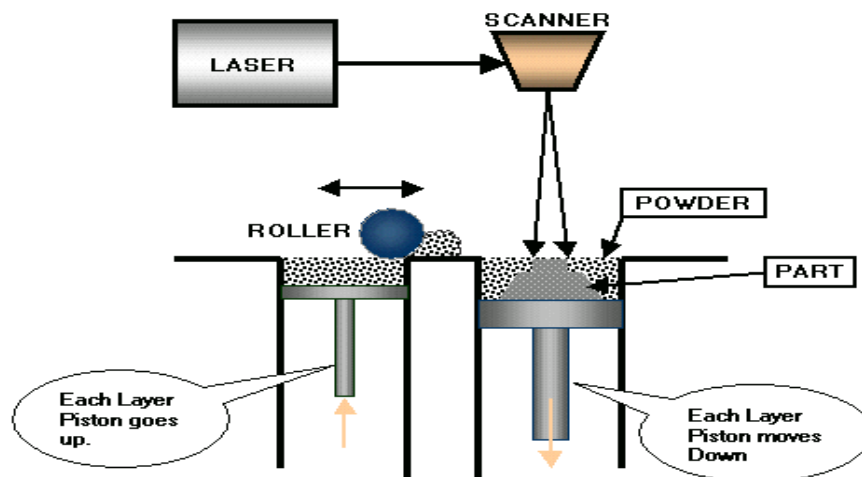
Figure1.1.7: Schematic of the Selective Laser Sintering process. [124]

Electron beam deposition is fundamentally the same process but uses an electron beam rather than a laser to create the initial melt pool. One major difference between electron beam and laser deposition is that for electron beam the process must be carried out in a vacuum chamber. Absence of magnetic fields is also essential.

1.1.2 Laser assisted direct write (LADW)

The following part of literature review focuses on the Laser Assisted Direct Write process and its application, which is the topic of this thesis. Key aspects of the study, including advances in conductive inks, laser intensity distribution shaping and mathematical modelling of the process, are also addressed.

1.1.2.1 Review of the LADW process

The LADW process referred to herein is an additive deposition process which uses laser energy to thermally cure a pre-deposited conductive ink track pattern on a substrate. As illustrated in Fig 1.1.8, after deposition, the sample is shifted onto a X-Y stage, a laser of a particular power and beam modes applied over the surface of the track and thus cures the sample.
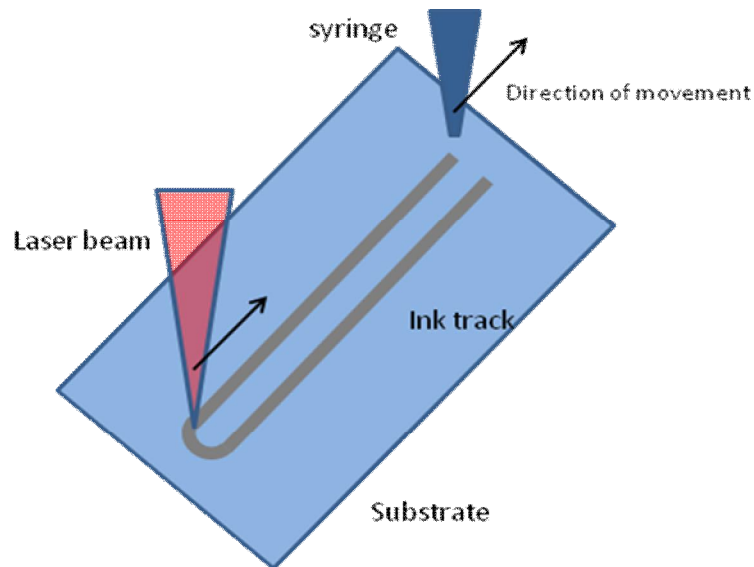
Figure1.1.8: Schematic of the Laser Assisted Direct Write process.

In LADW, as with any manufacturing process, the quality of the materials used is paramount when producing high cost, high quality components. A conductive ink is typically a fluid loaded with metallic (eg, silver) micro particles that have been fully suspended in resin. Solvent is added to reduce viscosity for deposition. Once deposited, the solvent is evaporated by heating to leave a thin film of micro particles in resin. The composite is then further heated to a higher temperature at which the resin starts to cross-link, and hence reduce in volume. The silver particles are then closely packed together and held by the cross-linked polymer, yielding electrical conductivity ranging from approximately 1% to 10% of bulk

silver [131]. Traditionally, ovens are used to cure the deposited ink. Advantages of this method include ease of operation and that a relatively large surface area can be cured at no additional time compared to small areas. However, oven curing is not necessarily desirable or possible in the case of heat sensitive substrates or many pre-existing geometries.

Fearon et al. studied the laser curing process extensively using empirical methods. They found, with single path curing under a stable laser source, for a fixed geometry of a particular kind of ink, the range of traverse speed resulting a satisfactory cure was fundamentally related to the thermal properties of the substrate [132].

Other work done in the field of photon-induced polymerisation has tended to focus on the microscopic physical chemistry side of mechanism, that is, for curing with a particular wavelength for a certain type of polymer bonding. For example, Mao et al. used in-situ Raman spectroscopy for the direct measurement of the $C = C$ molar concentration in the visible light curing vinyl ester resin [133]. Eduardo Jose et al. extensively studied the influence of different curing wavelength and chemical catalysts on the degree of conversion of resin using an argon ion laser, LED or quartz-tungsten-halogen light, with or without a chemical catalyst [134]. Some novel mechanisms have also been discovered. Cao et al. achieved creation of sub-50 nm features by using the direct laser writing technique based on single-photon photoinhibited polymerization. The super-resolution feature is realized by overlapping two laser beams of different wavelengths to enable the wavelength-controlled activation of photoinitiating and photoinhibiting processes in the polymerization[135].

However none of the research available provides any systematic understanding of the macroscopic relation between irradiation level and curing quality. In this sense the work presented in this thesis is completely novel. In this research a continuous wave CO_2 laser has been employed. The process is treated as a thermal one and depends on the thermal association of the absorption of photons by the material. In this manner a continuous wave laser is the primary candidate with an IR output.

1.1.2.2 Applications for LADW technology

The Laser Assisted Direct Write (LADW) method can be used to generate electrical circuitry on a substrate by depositing metallic ink and curing the ink thermally by a laser. Laser Curing has emerged over recent years as a novel yet efficient alternative to oven curing. This method

can be used in-situ, over complicated 3D contours of large parts (eg. aircraft wings) and selectively over heat sensitive substrates with little or no thermal damage.

Compared to existing DW technologies discussed previously in this chapter, the relatively low productivity of LADW confines its applications to the low volume, high value fields of engineering. LADW is basically a syringe based deposition method. Inkjet printing is the most popular conventional method for micro-fabrication on a substrate. As a potential substitution, LADW has advantages in that it is able to use higher viscosity liquids containing various sizes of micro particles [48]. LADW also has more flexibility than photolithography in terms of varying deposition geometry, though the resolution achieved may not be as high. LADW has already been extensively used in the medical field.　Kim et al. evaluated the shear bond strength (SBS) of orthodontic brackets bonded to teeth using a diode-pumped solid state (DPSS) laser of 473 nm with various light intensity and light-curing settings[136]; Shin et al. and Mirsasaani et al, respectively, evaluated the effectiveness of a diode-pumped solid state (DPSS) laser as a light source for light-curing dental resin composite [137, 138]; Shahbazi et al. demonstrated the feasibility of a novel, thin film, laser-activated adhesive in sealing penetrative corneal wounds with a view to replacing sutures in ophthalmic operations [139].

In terms of industrial utility, Akira et al. have fabricated a new type of plastic micro lens by laser polymerization. They found, the amount of resin polymerized by exposure to laser light (light curing) depends on the laser power and the exposure time. The shape of the lens can be controlled by changing the conditions of laser irradiation [140].

Other potential industrial uses of this technology cover applications in solar cells [5], Radio Frequency Identification-tags (RFID-tags) [6], flexible-electronics [7, 28, 30], Organic Light Emitting Diodes (OLED) displays, antenna, biological uses and many more [2, 35, 141, 142]. However, there are barriers to be overcome before Laser Assisted Direct Write can be fully implemented in the commercial arena [143]:

3) Manufacture of conductive inks which are optimised for laser curing.
4) Reliably achieving efficient laser curing with satisfactory conductivity, and acceptable adhesion to the substrates.

1.1.2.3 Inks and materials used for LADW

Conductive ink has been commonly and extensively used for printable electronics over the past two decades, due to the advantage of their availability, flexibility and economy. Inks

come in many forms and are selected chiefly depending on the application. But the most common types consist of three main components: conductive particle [144] (silver particle [145], silver flake, copper [146], aluminium, carbon particles of different grain sizes or a mixture of the listed; recent study reports of blending carbon nano-tube into conductive inks based in a formic acid/acetone co-solvent system[147]), Kim et al. also studied the effect on conductivity induced by varying particle sizes[148] ; a polymer resin which acts as a binding agent; and a solvent, which acts as carrier and controls the viscosity of ink for printing). The deposition process is extremely versatile. Currently the most common techniques are inkjet printing and variations of screen printing for the high throughput required in the electronics industry [149]. Also the printing of the substrate largely determines the type of ink and printing method used [150]. There are also a diversified sources for the post printing curing: electrical, microwave, plasma, laser and flash lamp annealing have all been used to a certain extent [151]. Inks of different components and different curing/sintering mechanism could differ greatly in performance in terms of conductivity, durability and sometimes even result in different failure mechanisms [152].

1.1.2.4 Beam shaping technologies and their applications

Gaussian beam intensity profiles have been most commonly used for laser processing, since they occur naturally as the operating mode for many lasers. However, a Gaussian intensity distribution is not capable of providing the uniform surface heat treatment desired by many laser processes. This is due to the large disparity between the intensity at the centre of the Gaussian beam and that at its outside edge. The effect of laser mode on the surface temperature distribution was investigated by Kar and Langlais [153] and earlier by Sharp [154]. They suggested that a shaped beam profile can improve many laser processing applications. Previous studies have shown ingenuity in both the intensity profiles created [155-158] and in the methods used for creating them [159-162].

For most applications a circularly symmetric intensity profile is preferred, since it will give a consistent result in all processing directions. The most commonly used top-hat [163] shaped intensity profile has a circular geometry with uniform intensity. The circular shape, however, dictates that, when the heat source or laser beam is moving, points further from its axis of movement experience reduced beam interaction time which leads to under-heating compared with points at the centre. One circularly symmetric beam profile which is capable of

achieving a relatively uniform maximum temperature rise on a surface is the annular ring. Annular rings are noted for having some success achieving more uniform heating effects both in stationary [164] and moving beam applications [165]. There are several methods of carrying out the transformation, all of which are based either on the principles of reflection, refraction, diffraction or a combination of these. However most of the existing methods achieve beam shaping at the cost of losing 50%-60% of power [166-168], also the intensity profiles produced cannot be easily varied for different processes.

The SunShaper designed by Wellburn [18] is a dynamic beam shaper possessing the advantage of being capable of tuning the output intensity profile and/or beam geometry to suit different processes, with virtually no loss of input power. It converts a CO_2 laser beam of the Gaussian mode into a plateau filled annular ring shape, the relative level of plateau fill can be easily varied by calibrated manual adjustment of the device (Fig 1.1.9). The flexible beam profiles produced by the SunShaper enable study of process optimisation for a wide range of laser surface heat treatments.
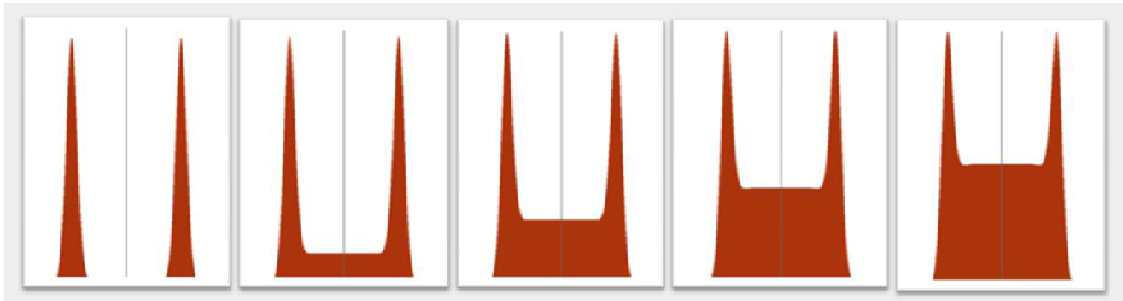
Figure1.1.9: Different beam profiles that can be achieved with the SunShaper[18].

1.1.2.5 Curing mechanisms of polymer inks

Remarkable advances have been made regarding the manufacture of inks[46] and in deposition techniques, while much less study has been done on the development of a mechanism for non-oven methods of curing.

Simone et al. [9] have studied the processing conditions to achieve functional coating on metallic substrates from thermal setting powders with a laser source. In this work, epoxy-polyester hybrid resin was supplied in the form of coarse powder, then coated on stainless steel 304 sheets before being cured with a CO_2 laser under a range of fluence and scan speed. She characterised the quality of this curing process with a defined adhesion index. An empirical model of the curing mechanism was then constructed based the results collected for

this adhesion index. The material used by Simone is largely different to that in this work, however the curing apparatus and procedure are similar. This work also extended the representation of results from an empirical approach to a self- contained numerical model.

Friis-Pedersen et al [169] studied the thermal curing process of epoxy resin, which is a representative ingredient of typical DW ink. An epoxy resin containing diglycidyl ether, dicyandiamide, and an accelerator (diurone) was investigated under different curing cycles. The mathematical prediction of the degree of curing in a thermoset as a function of time and temperature was investigated and compared to measured data. Near-infrared analysis was used to measure the conversion of epoxy and primary amine and the production of hydroxyl. Modulated differential scanning calorimetry was used to measure the changes in the heat capacity during curing. The measurements revealed differences in the primary amine conversion and hydroxyl production, and close relation to the measurements of heat capacity were found. The characteristics found were attributed to differences in the curing mechanisms. The mathematical model did not incorporate these differences, and this may have led to discrepancies between the predicted and actual values of the degree of curing. The DSC analysis used in Friis-Pedersen's study is also implemented in this work to obtain the actual heat capacity curve. The mathematical model used in his study is a generic analytical formulation which does not account the actual experimental environments. This drawback can be sufficiently compensated with a flexible and comprehensive FEM model that describes the exact process, as presented in this work.

Lewis et al [21, 170] modelled the curing kinetics for polyamide. Khan et al [10] studied the sintering of silver nanoparticles with a laser. There are also other research which have been carried out to study the effect of different light sources on the curing efficiency of resin [171-174] .

However, there are still gaps in the quantitative understanding of the dynamic laser curing process. There is need for a mechanism that accounts for the overall integrated effect of material properties and laser processing parameters over the curing quality in a real LADW situation. The work presented in this thesis aims to address these issues by providing such a mechanism, which is then accurately formulated into a repeatable and flexibly adjustable FEM numerical model. The modelled outputs are also supported by empirical results.

1.1.2.6 Mathematical modelling of laser material processing

Finite Element Method has been extensively utilised as an analytical tool for a wide range of laser material process [175]. There are numerous FEM softwares commercially available in the market; the most commonly used ones include Matlab, Abaqus, FEMtools and recently COMSOL Multiphysics. The choice of the software is dependant on the particular application and various commercial factors.

The modelling strategy of laser material processing can be generally divided into two categories based on the meshing methods, which is the consequence of the process: For processes that do not involve melting or deformation, a fixed mesh is used (eg surface hardening and heat treatment.) for those processes that involve melting or deformation, a changing mesh has to be implemented, along with varying boundary conditions.

In the former case, 4 node linear tetrahedrons are usually used as elements to generate a 3D mesh, with finer size around the laser processed region, growing into coarser elements away from the process region [176-183]. The latter situation is usually more complicated. In the cases of modelling for laser cladding, welding and forming, due to phase change or deformation of the material, a changing mesh is required for precise simulations.

For laser cladding and welding, meshing is adjusted between iterations in the time domain to address the change in the geometry of the meltpool, usually represented with an isotherm [175, 184-187]. In the cases of laser forming, the mesh elements are usually refreshed and regenerated after each sequence of laser movement, to accommodate the deformation induced [188-195].

In LADW a thin film of highly viscous ink is laid on top of a rigid substrate which is then illuminated by a defocused laser source with low intensity. This means there is negligible flow or deformation involved in the process and using a fixed mesh will provide sufficient accuracy for the simulation.

Fearon et al [132] found, for single path curing of fixed geometry of ink track, the range of traverse speeds resulting in satisfactory curing was related to the thermal properties of the substrate. Sato [36] investigated the effect of curing temperature changes on electrical conductivity and scratch resistance with both oven curing and laser curing. A curing mechanism was derived from the results obtained for three different composite polymer inks on a range of substrates.

There are several interdependent processing parameters on which the curing quality and efficiency strongly depend. Incorrect parameters can result in a track that is cured in some

areas and uncured in others, or in damaged substrates. Therefore not only is the empirical approach was time intensive, but also the outcome is often unpredictable if more than one of the parameters are varied.

This work addresses the strong need for a quantitative model which can systematically output the processing conditions for a given combination of ink, substrate and laser source. Transforming the LADW technique from a purely empirical approach, to a simple, repeatable, mathematically sound, efficient and predictable process is a key content of this work.

The method comprises a novel and generic Finite Element Method (FEM) model that for the first time predicts the evolution of the thermal profile of the ink track during laser curing and thus generates a parametric map which indicates the most suitable combination of parameters for process optimisation. Experimental data is compared with simulation results to verify the accuracy of the model.

The work enables efficient numerical simulation of the curing process for different substrate/ink combinations, taking into account the properties of the ink, substrate, and laser beam profile and generating a processing window which will be useful as a guide to engineers for the optimisation of the process [196, 197]. Due to commercial sensitivity, the exact composition of the ink used is not disclosed in this study. However, close approximation is made to generate an indicative parametric map which is then compared with experimental results.

1.1.3 Summary

The work conducted within this thesis and presented here details the development of a

laser curing low thermal process used in conjunction with inks manufacture by Gwent Electronics Group (GEM), creating a low cost manufacturing process for conformal directly written components. The emphasis of which has been on the curing process with analysis of the ink tracksø temperature evolution to gain a better understanding of what occurs during the thermal cure process.

Previously empirical methods have been used to generate processing windows for this technique. In this work, a predictive Finite Element Method (FEM) model for LADW in the COMSOL 4.0 environment has been developed. The model simulates the temperature evolution of the sample during the process. The results can be used to predict whether satisfactory curing has been achieved and thus indicate the suitability of the combination of curing parameters used. Laser intensity profiles can be defined in the model as analytical

functions, or imported as interpolation functions, and one can therefore predict the optimised beam mode by running the model.

In this study, CNC systems have been used to deposit and cure ink samples with consistent processing. Ink track samples are cured with a Gaussian profile and filled annular ring profiles produced with the SunShaper, over a range of curing speeds. The experimental results are presented and compared to model simulations, and thus indicate the significance of beam shaping in a LADW process by showing the improvements achieved.

1.2 Overview of the Finite Element Method and its application in this study

1.2.1 Introduction of the Finite Element Method (FEM)

The purpose of this chapter is to introduce the fundamental concepts of finite element method (FEM) as a general technique for finding numerical solutions of partial differential equations in science and engineering, how it can be applied to problems and the basic steps involved. Basic formulations and some proofs of key concepts are included, while abstract formulations are beyond the scope of this work. However, literature on this topic is readily available should the reader be interested. This chapter is structured to demonstrate how a general mathematical modelling approach is applied to solve the particular problem of study. Therefore it focuses on the mathematical methodology rather than rigorous proofs. Error estimations will also be included.

1.2.2 Background of numerical methods

The mathematical models of science and engineering mainly take the form of differential or integral equations. Using computer-implemented mathematical models, one can efficiently analyse and simulate complicated systems. This reduces the need for expensive and time-consuming experimental testing and makes it possible to compare many different alternatives for optimization[198-200].

To implement mathematical models on a computer one needs a numerical method; ie, an algorithm to find solutions. Only in the very simplest cases is it possible to find exact analytical solutions of the equations in a model, in general one has to rely on numerical techniques for finding approximate solutions. Among all the numerical methods the most popularly used are the finite difference method, finite volume method and the finite element

method. Some numerical methods may suit certain types of problems better than others, due to the nature of the physics involved, geometry, requirement of accuracy, efficiency of computation or other factors [29, 201-204].

The **finite difference methods** are numerical methods for approximating the solutions to differential equations using finite difference equations to approximate derivatives. This method is limited in terms of its applicability in complex engineering problems[205].

The **Finite volume method** is a method for representing and evaluating partial differential equations in the form of algebraic equations. Similar to the finite difference method or finite element method, values are calculated at discrete places on a meshed geometry. "Finite volume" refers to the small volume surrounding each node point on a mesh. In the finite volume method, volume integrals in a partial differential equation that contain a divergence term are converted to surface integrals, using the divergence theorem. These terms are then evaluated as fluxes at the surfaces of each finite volume. Because the flux entering a given volume is identical to that leaving the adjacent volume, these methods are conservative. Another advantage of the finite volume method is that it is easily formulated to allow for unstructured meshes. The method is used in many computational fluid dynamics packages[206].

The *finite element method* (FEM) is a general technique for numerical solution of differential and integral equations. The method was first introduced in the late 50øs and early 60øs for numerical solutions in structural mechanics. It soon became clear that in fact this method is a general technique for any numerical solution with roots in the variational methods[207]. Combined with Computer Aided Design (CAD), today FEM is used extensively in almost every area of physical science and engineering[203, 208].

1.2.3 Outline of FEM methodology

The basic idea in any numerical method for a differential equation is to discretize the given continuous problem with infinitely many degrees of freedom to a finite number of unknowns, and hence capable of being solved with a computer.

The basic steps of FEM involve the following[209];

    i.   Variational formulation of the given problem

ii. Discretisation with FEM method

iii. Solving the discrete problem

iv. Implementation of the method through programming

Topics (i-iii) are discussed in chapter 7, with (iv) explained in chapter 2.

1.2.4 FEM modelling for laser surface heat treatment

FEM has been extensively utilised in research of laser processing for a wide range of materials. Some key texts are summarised below:

For the surface hardening process of steels, a simulation of the thermo-metallurgical and mechanical coupling is elaborated by Yaakoubi, using ABAQUS software linked to phase transformation and elasticóplastic modules[210]. The application of this method makes it possible to highlight the metallurgical and mechanical behaviour laws and procedures used to calculate austenite grain size, hardness, microstructure effect on physical properties, transformation latent heat, deformation progress, and stress genesis during a surface hardening process.

The thermal effects of Łbre laser surface treatment on a Si_3N_4 engineering ceramic were studied using a computational Łnite element analysis (FEA) by Shukla and Lawrence[211]. By utilising data obtained from a TG-DSC analysis the FEA model predictions of the temperature distribution were used to map phase transformations and signiŁcant events occurring during the Łbre laser surface treatment of the Si_3N_4.

Wellburn showed that in the case of surface heat treatment of sheet metal, assuming that , C_p and k are constant during the process, then the optimised uniformity achieved at any depth, corresponds to a particular Peclet number for any given beam profile. Certain beam profiles are able to achieve much better uniformity compared to other[18].

2. Theoretical background and model construction

This chapter discusses the theoretical background of the laser curing process. A parameterised mechanism is derived and implemented in the FEM model. Topics in this chapter include a schematic of the set-up, properties of materials, beam mode approximations, formulisation of the curing mechanism, curing criteria and model construction.

2.1 Curing Process Overview

The laser assisted curing method is an application that involves the integration of knowledge in physical chemistry, mathematical modelling, process automation and laser optics. Laser induced heat conduction has been well studied both theoretically and experimentally for applications of metal machining and surface treatments [14, 212-216]. However there is still a lack of formulised investigation of composite inks. In this study, samples of typical industrial application scale are prepared in a laboratory environment. The sample geometry and thermal properties are parameterised in the FEM package. An overall nonlinear curing mechanism is also built in the FEM model through a set of coupled PDEs and boundary conditions, which include the beam modes, curing criteria and many other non-linear properties. The simulation outputs act as results of theoretical studies, which are compared with a range of experimental data in later study, to verify the validity of the understanding of laser curing mechanism derived.
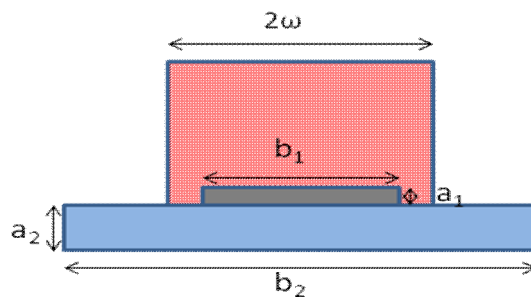
2.2 Schematics of configuration

Fig 2.1 Cross-sectional view of an ink track sample

The cross-section of the set-up is illustrated in Fig 2.1. An ink track of thickness a_1 and width b_1 is laid on top of a substrate of thickness a_2 and width b_2, and the laser beam with a

diameter of 2   couples heat into the top surface of the sample. The laser beam then traverses along the track with a constant translational speed, and thus cures a sample, as shown in Fig 2.2. Assuming the sample is infinitely long in the direction of laser spot movement, then curing result achieved will be identical along the longitudinal axis.
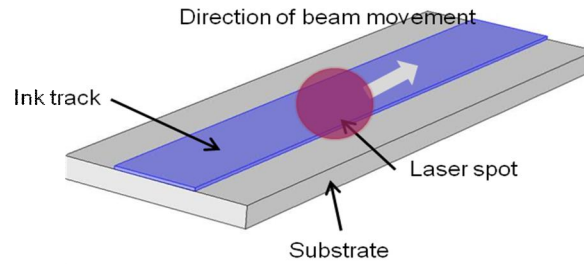

Fig 2.2 Schematic of curing set-up.

In the experiments carried out in this work, the size of laser spot is treated as a variable and thus can be flexibly adjusted; for example, a focused or defocused Gaussian beam can be used. Differently shaped beams can also been used, which is in practice achieved with various beam shaping techniques described in the previous chapter.

2.3 Materials

2.3.1 Inks

 The inks used in this theoretical part of the study are generic inks, which approximate the content and mixing ratio of the actual conductive inks used in experiments, manufactured by GEM. For example, in the case of D58 ink, the modelled ink volumetrically contains ~13% silver micro particles, ~51% Ethanol as solvent, and ~36% Epoxy Resin as bonding agent (the mixing ratio is from that of D58 ink). The combination of constituents is chosen by the manufacturer for best performance. The choices of resin and solvent are often uncommon substances protected by patents. However, close approximation is made to give generic and indicative model simulation results [217]. Table 2.1 shows a few common Gem Inks and properties.

Table 2.1: Types and properties of common GEM inks

Name	Description
D1	Platinised Carbon Ink; an economic alternative for low temperature applications
D58	Silver ink designed to be used for screen printing working electrodes.
D6	A screen printable Platinum ink designed for printing working electrodes in electrochemical sensor applications.

2.3.2 Substrates

There are a few common substrates used for LADW. The popular types include alumina (Al_2O_3), polyethylene terephthalate (PET), carbon fibre composite (CFC), polyaramid and paper, as listed in Table 2.2. This work focuses on the two most commonly used materials, namely alumina and PET. Alumina is used as a well known dielectric material, which is chemically inert and thermally resistant; it also has excellent durability in harsh environments due to its hardness. Alumina is light weight and reasonably cheap. PET is chosen for its light weight, physical flexibility, elasticity against stress, and economical advantage. PET has relatively low thermal conductivity; while Al_2O_3 is considerably more thermally conductive. Therefore the LADW curing process on PET is very different from that on Alumina.

Table 2.2: A table of substrate properties

Substrate	Thermal Conductivity (W/mK)	Advantage	Disadvantage	Density (kg/m^3)	Specific Heat Capacity (J/kgK)
Alumina	18	hard, thermally resistant, rigid	brittle	961	880
CFC	0.059	light, strong	brittle	1850	950
PET	0.23	flexible cheap, light	easily thermally damaged	1380	1000
Polyaramid	0.04	flexible cheap, light	easily thermally damaged, variable surface roughness	1440	1400
Burn Paper	0.01	cheap light, flexible	poor strength, poor resistance to humidity	192	1336

2.4 Laser intensity distributions

2.4.1 Gaussian

A Gaussian beam is a [beam] of [electromagnetic radiation] whose transverse [electric field] and [intensity] distributions are well approximated by [Gaussian functions]. Many [lasers] emit beams that approximate a Gaussian profile, in which case the laser is said to be operating on the fundamental [transverse mode], or "TEM_{00} mode" of the laser [optical resonator].

A Gaussian beam mode is described by the following equation

$$I = I_0 \exp\left(-\frac{2r^2}{\omega^2} \right)$$

(2.1)

where I_0 is the peak intensity at the centre of the beam,   is the beam waist; r is the distance away from the centre of the beam, illustrated in Fig 2.3.
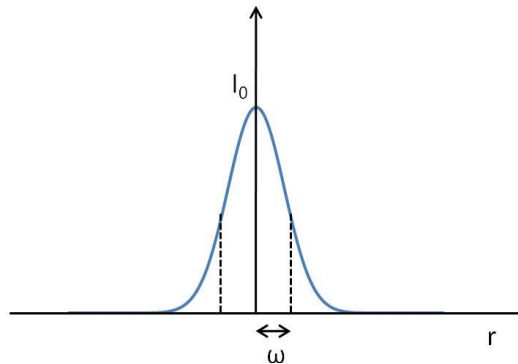

Fig 2.3 The Gaussian intensity distribution.

The Gaussian beam mode is good for operations such as cutting, drilling and welding. In these processes the beam quality of the laser often determines the quality of the process. However this mode is not ideal for surface heat treatment, due to the uneven energy intensity between the centre and the edge of the laser spot.

2.4.2 Top-hat

A top-hat beam profile can be described by the following

$$I_{TH} = I_1 \quad \text{if } r \ddot{O} \quad _1$$

(2.2)

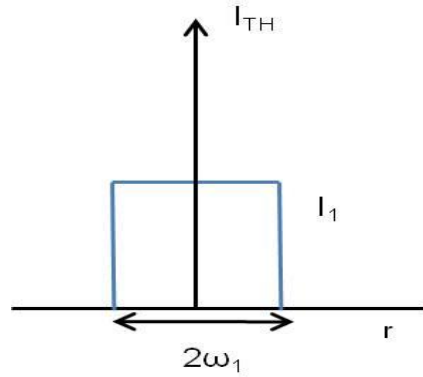$$= 0 \quad \text{if } r > \quad _1$$

Fig 2.4 The top-hat intensity distribution.

The circular top-hat intensity distribution is one of the most popular shaped profiles. It homogenises laser intensity and evenly distributes energy across the focus spot. Like the Gaussian beam, the circular shape enables top-hat beams to be used in any direction. It is mostly applied in selectively micro-machining thin films in the electronics, displays and solar cells industry. Also this beam profile is highly desired in surface heat treatment of metal parts compared to Gaussian beams, in the sense that it can reduce the overlapping needed, hence speeding up the process while reducing undesired tempering effect [18].

2.4.3 Annular filled rings
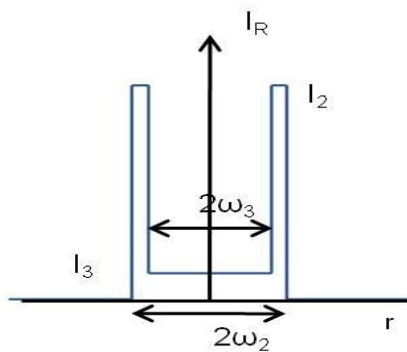
$$I_R = I_2 \quad \text{if} \quad _3 < r \ddot{O} \; _2 \quad\quad\quad\quad (2.3)$$

$$= I_3 \quad \text{if } r < \; _3$$

$$= 0 \quad \text{if } r > \; _2$$

Fig 2.5 Schematic of curing set-up.

Wellburn [18] studied the advantage of the annular ring profile extensively. He suggested that the filled ring has advantages compared to both Gaussian and the top-hat intensity distributions. In his work simulations were used to successfully support this argument. However, the simulation done in his work was based on a slab of metal, which is linear and homogeneous. A direct translation of argument to this study would be invalid since this work investigates the application of a shaped beam in curing ink tracks, that is, surface treating a thin, non-linear material.

2.4.4 Power integration over the beam focal spot

The total power delivered by a laser beam can be calculated by integrating the intensity over the area irradiated:

$$P = \iint I_i dA \qquad (2.4)$$

where P is the power of laser, and dA is the area increment of the processed surface.

2.5 Curing mechanism

In this section, a novel theory for the curing mechanism has been proposed and formulated in detail. For the first time, a comprehensive account of the thermal dynamic process for LADW is demonstrated, allowing a parametric study over a range of processes with similar mechanisms and set-ups.

Fig 2.6 illustrates a single pass curing process. As discussed previously, the ink is a composite of silver particles, resin and solvent, and hence, a nonlinear overall curing mechanism takes place. The temperature of the ink rises in a series of steps as the heat source gradually couples energy into the ink. In stage 1, heat from laser brings the irradiated region to an elevated temperature of vaporisation T_v, which is the temperature where the latent heat of evaporation of solvent becomes dominant, represented by stage 2. After the solvent evaporates, the volume has contracted, resulting in the silver particles becoming more closely packed.

The overall reduced heat capacity results a larger curve gradient in stage 3. Further heating will elevate the temperature of the material untill T_{cur} is achieved. T_{cur} is the temperature

where cross-linking takes place, in stage 4. Once this stage is finished, the ink can be considered cured and extra energy will only go into heating the ink track, stage 5. If an õover-curingö temperature T_{ov} is exceeded, one risks damaging the bonding between the silver track and the substrate, and therefore this needs to be avoided. For the generic ink of the study illustrated in Fig 2.6, T_v is set to 80 $^{\circ}$C (353 K), T_{cur} is 160 $^{\circ}$C (433K) and T_{ov} is 330 $^{\circ}$C (603 K). This mechanism approaches the problem from a purely thermal point of view and assumes the material to be homogeneous at during the curing process.

2.5.1 Coupled laser energy

Based on this analysis, we have

$$\Delta Q = \sum \Delta Q_i = \Delta Q_1 + \Delta Q_2 + \Delta Q_3 + \Delta Q_4 + \Delta Q_5 \qquad (2.5)$$

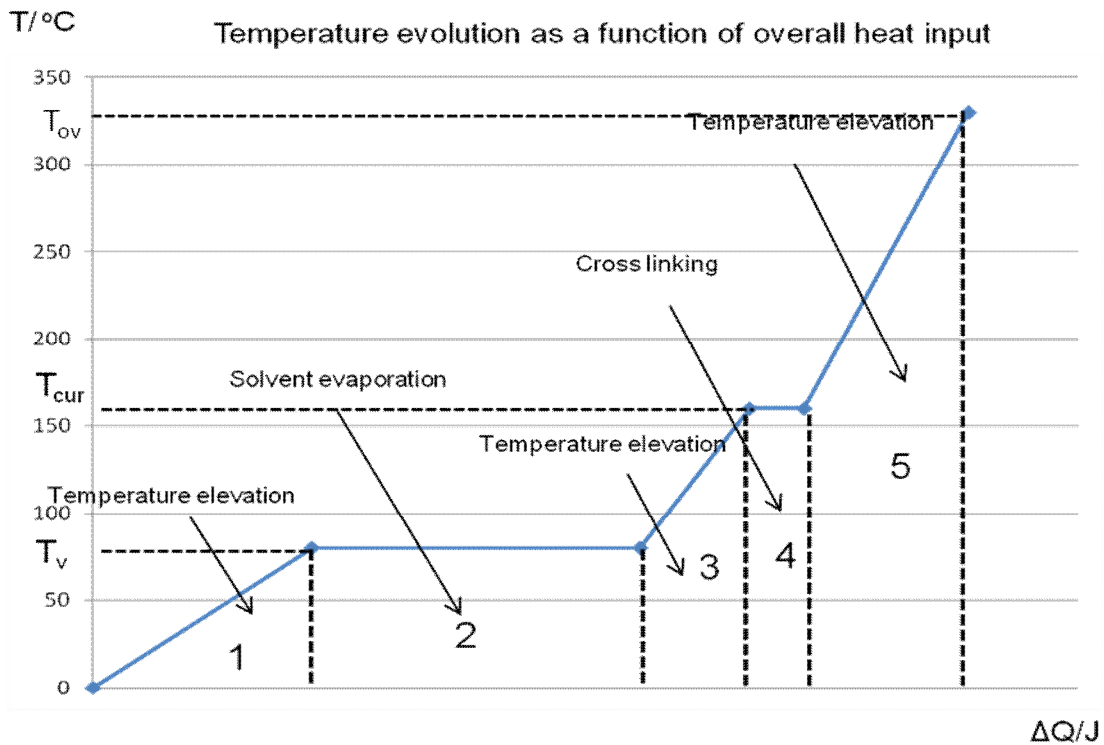where Q is the total energy required to bring unit volume of ink from room temperature to

Fig 2.6 Curing mechanism for a composite ink.

T_{ov}; Q_1, Q_2, Q_3, Q_4 Q_5 are respectively the energy required for the individual stages described in Fig 2.6.

If we denote the temperature change for each stage with T_i, denote the Latent heat of solvent with L_s, the energy for cross-linking with L_{cr}, and use C_p for the specific heat capacity with, for density, and % for volumetric percentage, then we have

$$\Delta T_1 V[(Ag\%)\rho_{Ag}C_{p(Ag)} + (r\%)\rho_r C_{p(r)} + (s\%)\rho_s C_{p(s)}] = \Delta Q_1 \tag{2.6}$$

$$V(s\%)\rho_s L_s = \Delta Q_2 \tag{2.7}$$

$$\Delta T_3 V[(Ag\%)\rho_{Ag}C_{p(Ag)} + (r\%)\rho_r C_{p(r)}] = \Delta Q_3 \tag{2.8}$$

$$V(r\%)\rho_r L_{cr} = \Delta Q_4 \tag{2.9}$$

$$\Delta T_5 V[(Ag\%)\rho_{Ag}C_{p(Ag)} + (r\%)\rho_r C_{p(r)}] = \Delta Q_5 \tag{2.10}$$

where V is unit volume.

The suffixes Ag, r and s respectively represent silver micro particles, resin and solvent.

We assume the density and specific heat capacity of epoxy resin do not change over the curing process. The specific heat capacity and Latent heat of Ethanol is 2.3 KJ/kg and 846 KJ/kg. The cross-linking energy of the resin is approximately 890 J/kg, as estimated from Sato's result [131]

2.5.2 Effective Specific Heat Capacity

As a consequence of the nonlinearity of the ink system, one needs to define an Effective Specific Heat Capacity $C_{p\text{-eff}}$ for the ink, which is a function of temperature. Use $_{ink-i}$ for the corresponding density of the ink for each stage of curing, we have:

$$\Delta T V \rho_{ink-i} C_{p-eff} = \Delta Q_i \tag{2.11}$$

and $$C_{p-eff} = (\frac{\Delta Q_i}{\Delta T_i V})\rho_{ink-i}^{-1} \tag{2.12}$$

Assume

$$\rho_{ink-1} = \rho_{ink-2} = (Ag\%)\rho_{Ag} + (r\%)\rho_r + (s\%)\rho_s \qquad (2.13)$$

$$\rho_{ink-3} = \rho_{ink-4} = \rho_{ink-5} = (Ag\%)\rho_{Ag} + (r\%)\rho_r \qquad (2.14)$$

Then, C_{p-eff} can be calculated and interpolated as a function of temperature, as shown in Fig 2.7. It is important to be aware of that, the Latent heat of evaporation of solvent and cross-linking energy of resin have both been smoothed over a small temperature increment of 5K. This is to avoid mathematical singularity, and the adjustment has negligible effect on the overall model accuracy.
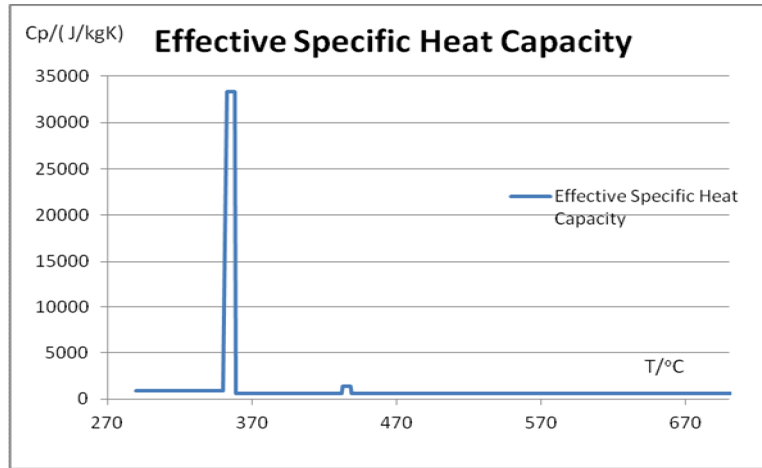
Fig 2.7 Modelled specific heat capacity of D58 ink against ink temperature.

2.5.3 Absorption coefficient

The absorption coefficient of the ink also is a nonlinear function of temperature. A CO_2 laser source outputs light of 10.6 micron wavelpength, for which silver can be regarded as totally reflective. Sato[131] has measured the absorption coefficient of the resin, and suggests an extinction coefficient $k_d=1.54 \times 10^{-2}$. In the specific case of this study, the optical path, l_r, in the resin is

$$l_r = r\% \cdot a_1 = 36\% \times 60 = 22\,\mu m \qquad (2.15)$$

And the absorption coefficient A_r is

$$A_r = (1 - \frac{I}{I_0}) = 1 - \exp(-\frac{4\pi}{\lambda} k_d l_r) = 32.08\% \tag{2.16}$$

Regarding to the absorption of ethanol, Hullbrook and Shaw [141] have found the absorption cross-section per molecule to be $=16.8\times10^{-20}$ cm^2. If N is the molecule number density, l_s is the optical paths in the solvent, then

$$l_s = s\% \cdot a_1 = 51\% \times 60 = 31\,\mu m \tag{2.17}$$

$$N = \frac{\rho_s}{M_a} N_A \tag{2.18}$$

where $_s$ is ethanol density, M_a is the molar mass of ethanol, and N_A is the Avogadro constant.

According to Beer-Lambert Law, the absorption coefficient for solvent in this case will be

$$A_s = \min[1, \sigma \cdot N \cdot l_s] = 1 \tag{2.19}$$

This means that the solvent will absorb most of the laser light.

Therefore the total absorption of the ink track before solvent vaporisation is

$$A = (1 - Ag\%)[A_s + (1 - A_s)A_r] = 1 - Ag\% = 87\% \tag{2.20}$$

and $A = (1 - Ag\%) A_r = 27.8\%$ $\hspace{2cm}$ (2.21)

after solvent vaporisation.

The absorption A as a function of time is shown in Fig 2.8

2.5.4 Thermal conductivity

Another very important nonlinear property of the ink is thermal conductivity, which changes as the track becomes cured. The typical value before curing is close to that of the solvent or resin, and higher after curing, when the silver particles pack together. The thermal conductivity of ink track after curing can be calculated from its linear relationship with electrical conductivity according to the Wiedemann-Franz law. For metals, the ratio of thermal to electrical conductivity is:

$$\frac{\sigma_{T-ink}}{\sigma_{e-ink}} = \frac{\sigma_{T-Ag}}{\sigma_{e-Ag}} = \frac{2}{3}(k/e)^2 \times T \qquad (2.22)$$

therefore

$$\sigma_{T-ink} = \frac{\sigma_{T-Ag}}{\sigma_{e-Ag}}\sigma_{e-ink} = \sigma_{T-Ag}\frac{\sigma_{e-ink}}{\sigma_{e-Ag}} \qquad (2.23)$$

For single pass curing, experience suggests the ratio of electrical conductivity between cured ink and bulk silver averages to ~0.022. $_{T-Ag}$ is 429, so $_{T-ink}$ ~9.5 W/mK is the estimated value for thermal conductivity of the ink track after curing. Fig 2.9 is the interpolated function of thermal conductivity:
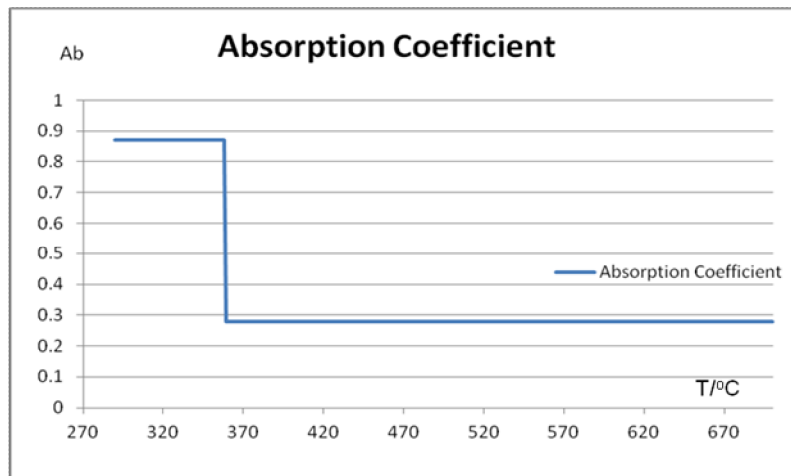

Fig 2.8 modelled absorption coefficient of D58 ink for 10.6 micron wavelength radiation, as a function of temperature.
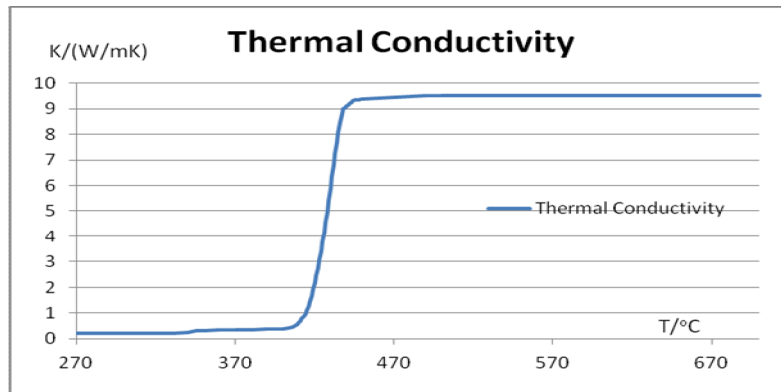

Fig 2.9 Modelled thermal conductivity of ink as a function of temperature

It is important to be aware the curve for K is smoothed around 433K, to ensure the existence of the second derivative for convergence.

The effective heat capacity, optical absorption coefficient and thermal conductivity curves are modelled functions. In reality these parameters may take different values as demonstrated with STA analysis later in section 4.4.

2.5.5 Governing conductive heat equation

Thermal energy is conducted within the ink track, within the substrate and through the interface according to the heat equation:

$$\rho C_p \frac{\partial T}{\partial t} + \nabla(-k\nabla T) = 0 \qquad (2.24)$$

where   is the density of material, C_p is the heat capacity, k is thermal conductivity and T is the local temperature.

2.5.6 Boundary conditions

Fig 2.10 illustrates the geometrical model set-up in the modelling environment. A laser beam of a certain intensity distribution couples energy into the top surface of the ink track, thus raising the local temperature. Heat is then conducted through the ink and substrate. The track becomes cured as the beam traverses along the track.

Surfaces of the ink track and substrate are subjected to Neumann boundary conditions as a result of convective cooling, laser inflow and radiation. Convective cooling with ambient air gives:

$$-k\nabla T \bullet \underset{\rightarrow}{n} = h(T - T_0) \qquad (2.25)$$

The top surface is coupled with inward heat flux from the Laser:

$$-k\nabla T \bullet \underset{\rightarrow}{n} = I + h(T - T_0) \qquad (2.26)$$

I is the input Laser intensity and h is the convective cooling coefficient.

After curing the ink track will be left at an elevated temperature at which the surface of the track would lose heat through radiation, in addition to convective cooling. The radiating intensity J is

$$J = \sigma \cdot \varepsilon \cdot T^4 \qquad (2.27)$$

where   is the Stefan-Boltzmann constant and   is the emissivity.

Therefore equation (25) describes the top surface of the ink track

$$-k\nabla T \bullet \underrightarrow{n} = I + h(T - T_0) + \sigma \cdot \varepsilon \cdot T^4 \qquad (2.28)$$

The bottom surface is insulated.

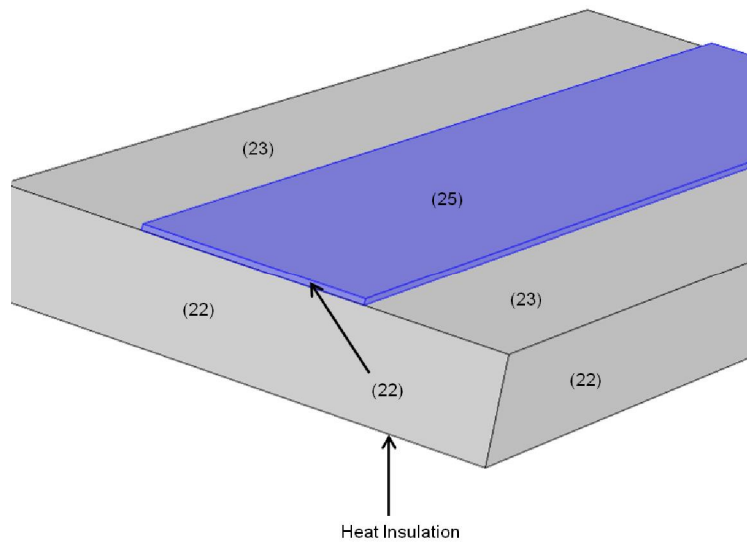The applications of these boundary conditions are illustrated in Fig 8:

Fig 2.10 Illustration of the boundary conditions in a typical simulation

2.5.7 Curing criteria

The cross section of an ink track with width 2R is shown in Fig 2 .11. The dashed line marks the interface between the ink and the substrate.
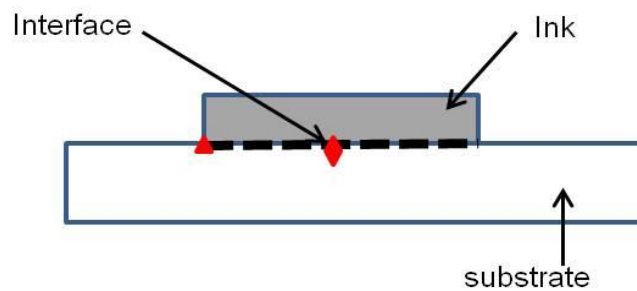

Fig 2.11. Cross sectional view of an ink track sample.

The highest temperature reached along this line can be extracted from simulation results and compared to the curing criteria, illustrated in Fig 2.12. If the temperature is between T_c and T_{ov} everywhere on the interface, then the ink is considered cured; if the temperature at any point is below T_c or above T_{ov}, the track is considered undercured or overcured respectively. The highest temperatures achieved at the centre (marked with a diamond shape) and the edges (marked with the triangle) are compared, and the difference between the two will be used to represent the temperature disparity for the particular intensity profile used.

The curing criterion is defined based on the temperature distribution along this interface: After running the model, the temperature evolution is stored in the memory for any point in the geometry. The highest temperature reached along the interface during this process can then be interrogated and extracted from simulation results. If the temperature is between T_c and T_{ov} everywhere on the interface, then the ink is considered cured; if the temperature at any point is below T_c or above T_{ov}, the track is considered undercured or overcured respectively.
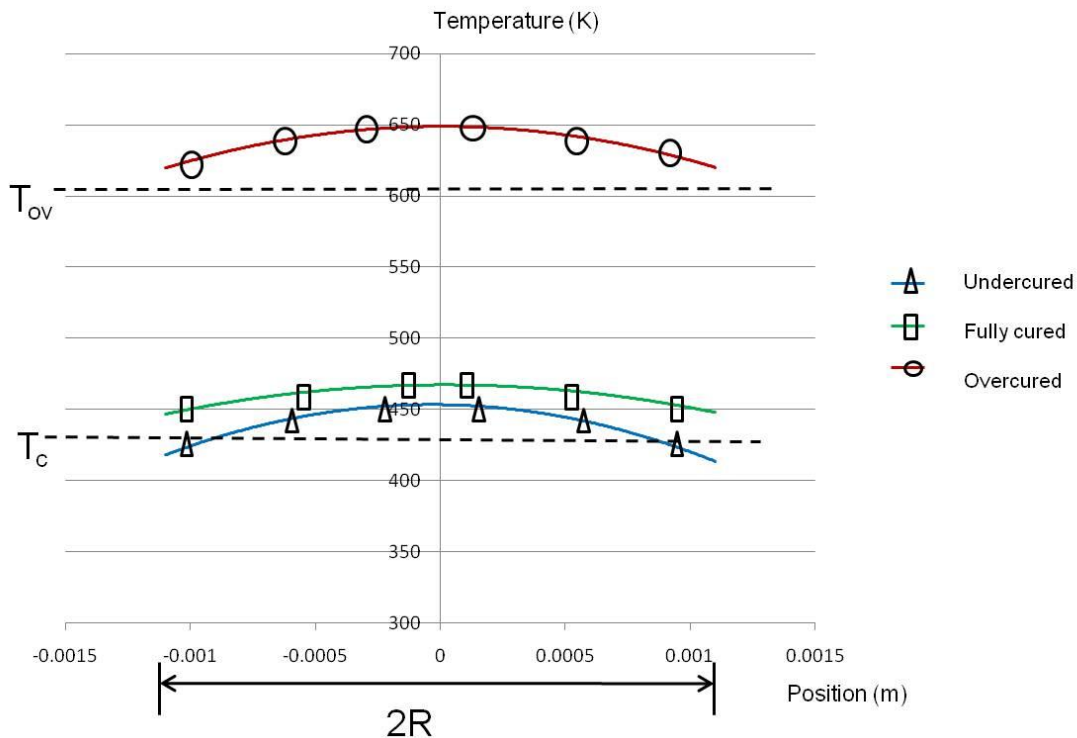

Fig 2.12. Curing criteria: examples of temperature distributions on the interface that represent undercuring, overcuring and cured situations.

2.5.8 Assumptions:

Here we summarise the key assumptions made:

- It is assumed that the ink geometry is uniform and the laser power is continuous and stable[214]. Also, as already mentioned, the resin and solvent are assumed to be Epoxy Resin and Ethanol respectively.

- The ink is homogeneous, ie, the silver and polymer is homogeneously dispersed within the solvent.

- Solvent is only evaporated once T_v is reached. In reality, solvent vaporises even at room temperature, however the rate is very slow compared to that at T_v.

- Cross linking only occurs at T_{cur}. In practice cross linking takes place over a small range of temperatures centred at T_{cur}.

- We assume thermal and electrical conductivity of the ink track is independent of the sizes and shapes of silver particles, once curing is completed.

- In LADW one usually uses low laser intensity and a relatively large defocused spot. The traverse speed is also usually quite low. These mean there is sufficient time for heat to be conducted away efficiently, instead of any local accumulation. Therefore the conventional role of time in metal heat treatment does not apply here.

2.6 Model Building

2.6.1 Overview

This section introduces the strategy , the hardware and software used to build and solve the FEM model.

2.6.1.1 General model strategy

The modelling strategy is illustrated in Fig 2.13: For any particular ink of study, model simulations are carried out to scan through each combination of processing parameters within a suitable range of investigation. Positional temperature distribution is then compared with the curing criteria. Results are marked as cured, undercured and overcured.

2.6.1.2 Comsol Multiphysics model environment

The modelling environment is COMSOL Multyphisics 4.0. (Fig 2.14)

COMSOL Multiphysics is a powerful interactive environment for modelling and solving many kinds of scientific and engineering problems involving partial differential equations (PDEs). With this software, one can easily extend conventional models for one type of physics into multiphysics models that solve coupled physics phenomena. The software runs the finite element analysis together with adaptive meshing and error control using a variety of numerical solvers. COMSOL Multiphysics offers modelling and analysis power for many application areas, the package provides a resourceful built-in modules bank for commonly used physics and a large material library (Fig 2.15). In this particular study, the Heat Transfer and Solid Mechanics modules are used.
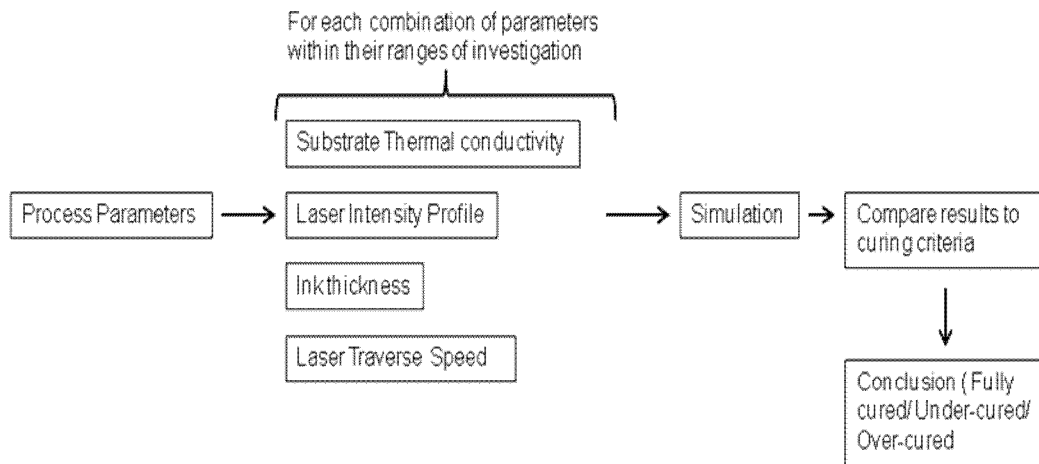

Fig 2.13: General modelling strategy
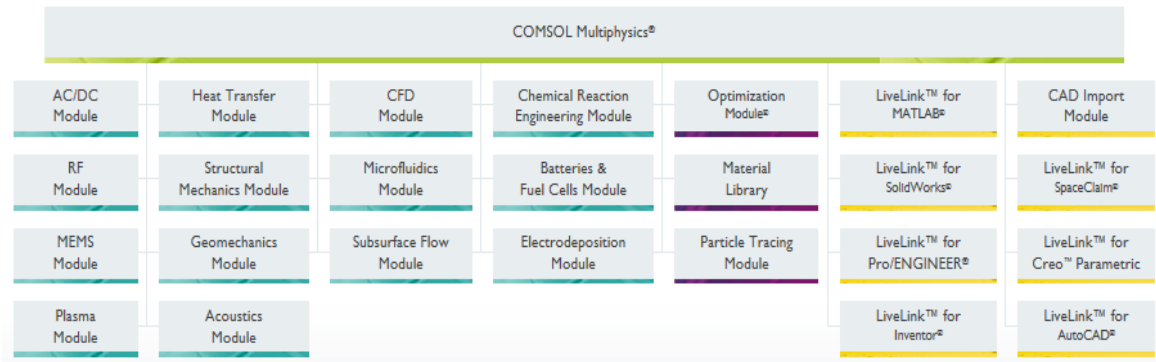

Fig 2.14: COMSOL Multiphysics 4.0

Fig 2.15: Built in modules in COMSOL Multiphysics 4.0

2.6.1.3 Hardware requirement

All of the following factors will affect the amount of computation involved in a FEM simulation:

- Number of mesh elements

- 3D models (as opposed to 1D, 2D, or 2D symmetric)

- Amount of coupled physics to be solved (the number of coupled PDEs)

- Smoothness of the functions in PDEs

- Size and number of time steps

The total number of nodes determines the size of the matrix to be solved, and therefore an increase in the number of elements or dimensions will geometrically increase the amount of calculation. If the physics to be solved is a complicated PDE system involving many parameters and variables, it will also take longer to solve for each node than a simple, straight forward linear problem. The smoothness of the functions determines how easy it is to converge and find a solution for the matrix. Also the time steps will decide the numbers of iterations to be run to complete the simulation.

A LADW model is a nonlinear, 3D, time dependant problem, and therefore needs high computing speed to simulate efficiently. High memory storage is also required, given the size of the computation.

Two computer systems of the following specifications were purchased and used:

(1) Processor, Intel Corei7 870

(2) Processing speed, 2.93GHz

(3) RAM, 8Gb

(4) System, Windows 7

The systems used are high-cost PCs installed with state of the art processor õIntel Corei7 870ö. They were the best option available at the time in terms of cost and functionality.

2.6.2 Model construction

This section goes through the steps taken to build a FEM LADW model in COMSOL 4.0.

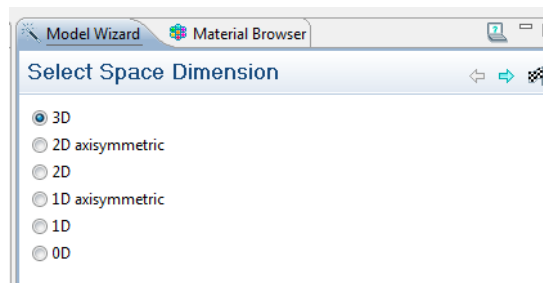2.6.2.1 Initiating model type and selection of physics involved

Fig 2.16 Select model

One first chooses the dimension of the model there is going to be built. The less degrees of freedom involved, the faster simulations would run. Therefore one should always choose the lowest dimension required.

The physics tab includes all the built-in physical differential equations, based on the area of applications. One or more physics can be added to the model. Each application contains many subcategories, as illustrated in Fig 2.17: Structural Mechanics include many fields such as Solid Mechanics, Thermal stress, Beam, Shell, etc.

The type of study is selected, a process under equilibrium will apply to Stationary study, and a dynamic problem will require the Time Dependent option to be selected. In this case we choose Time Dependant study to simulate the change in temperature profile as a laser beam traverses across and cures the sample.
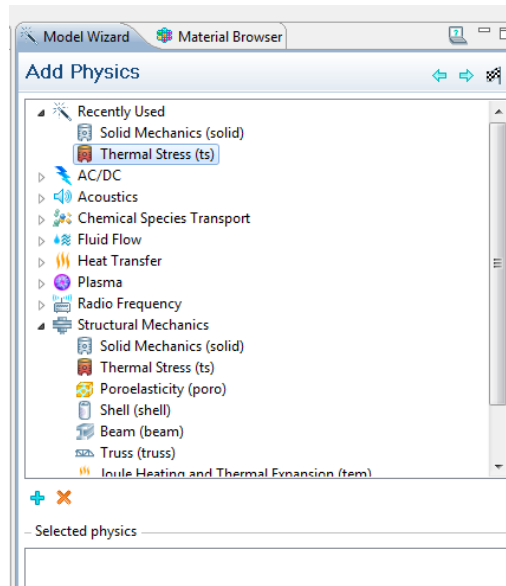
Fig 2.17 Physics modules that can be added to the
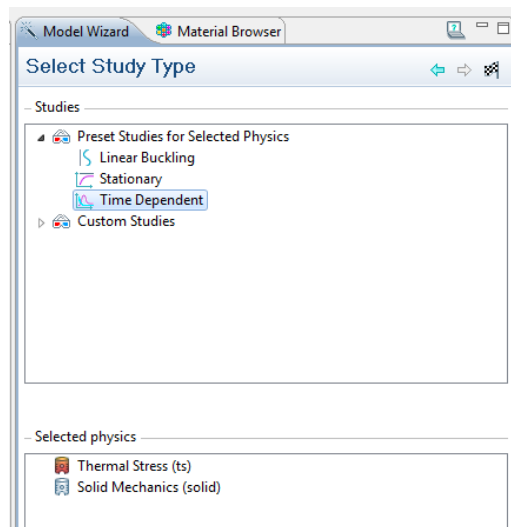
Fig 2.18 Time dependency of the study

2.6.2.2 Geometrical build up

The model builder (Fig 2.19) consists of the following major components, arranged top-down in the order of logical building sequence: Definitions, Model, Study and Result. Specifically in the Model section, one edits the information of definitions, geometry, materials, physics and mesh, for the particular study.

In the Parameters tab, all the constant parameters are defined, including geometry dimensions, laser profiles and other physical properties of the system. The field of each parameter can be

a constant number or an equation involving other defined parameters, provided a valid unit is specified.
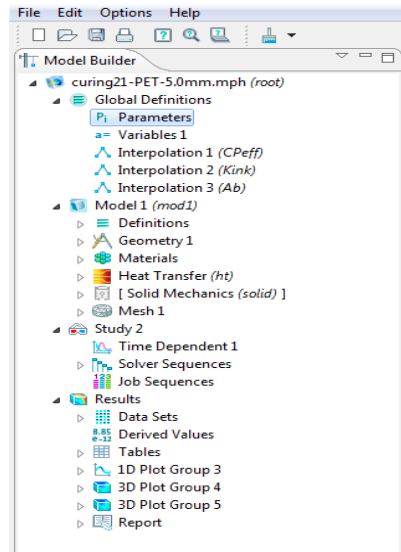
Fig 2.19 The model builder
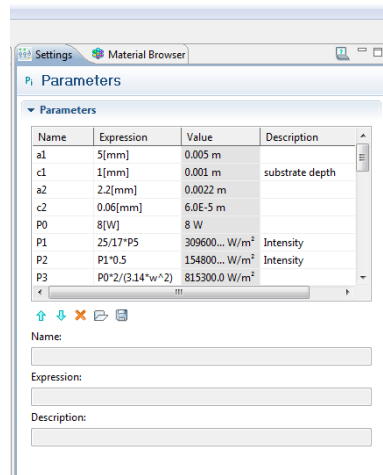
Fig 2.20 The parameter window

For the simple geometry involved in this case, both substrate and ink track are defined as strips (Block), with dimensions specified in the CAD package interface, shown above in Fig 2.21.

COMSOL provides a basic 3D drawing tool-kit with which one can quickly build simple geometries. More complicated shapes can be firstly constructed in professional CAD packages (such as UG, ProE and Solid Works), then imported into COMSOL as an IGES or SAT file. Fig 2.22 shows the parameterised geometry of the sample.
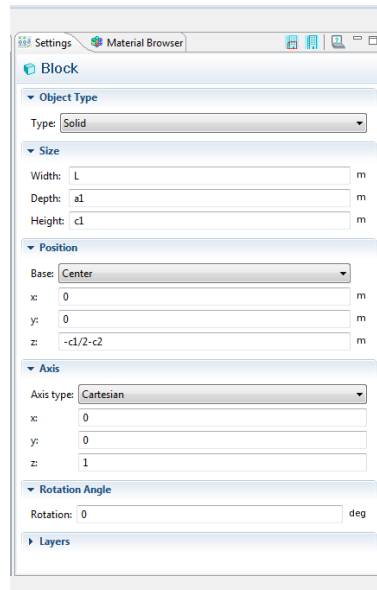
Fig 2.21 Defining model geometry
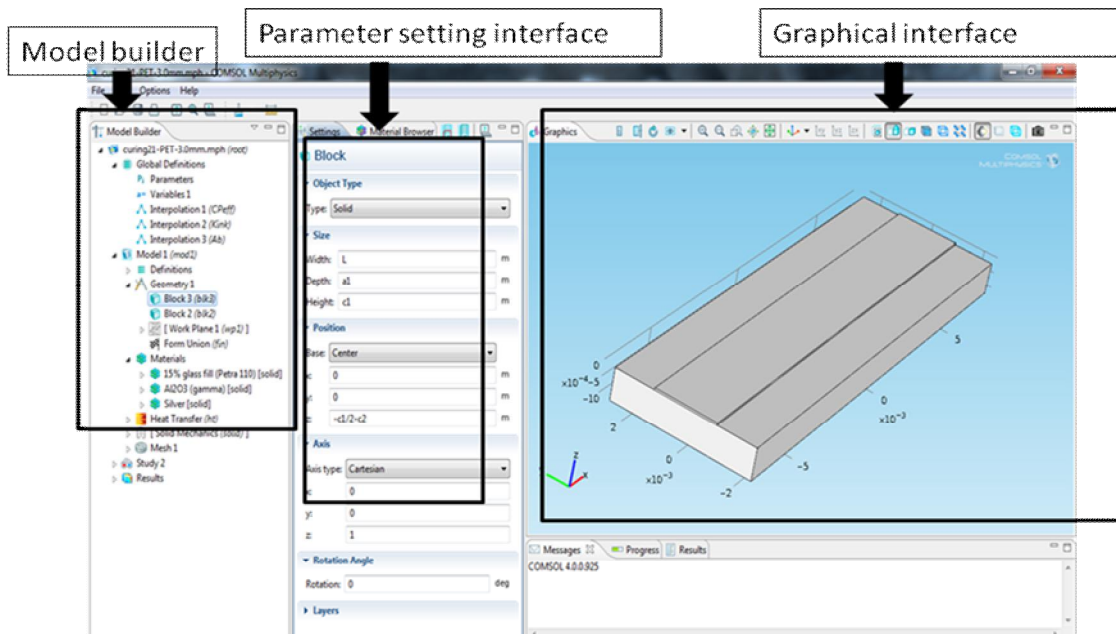
Fig 2.22: Geometry construction in COMSOL Multiphysics 4.0

2.6.2.3 Application of material physics and boundary conditions

Material physics are selected for the ink and substrate, which includes the heat influx from the laser source, thermal conductivity within the domain, convective cooling and radiation on the boundary surfaces, and a group of user defined variables and functions.
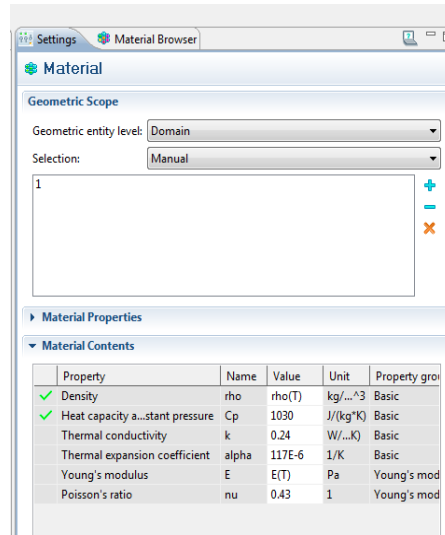
Fig 2.23 Material properties and coefficients

The materials used in this study can be selected and assigned to the corresponding geometry with the Materials/Coefficients Library. The Materials/Coefficients Library is an extensible database with properties for a broad collection coefficients and physical, mechanical, electromagnetic, and thermal properties of materials. The library includes metal, ceramics, semi-conductor, plastic, elements and composite materials of solid, liquid, gas and plasma phases. In the Materials/Coefficients Library dialog box (shown in Fig 2.23) you can add and edit library entries. Further, you can define multiple materials libraries, each stored in a separate data file.
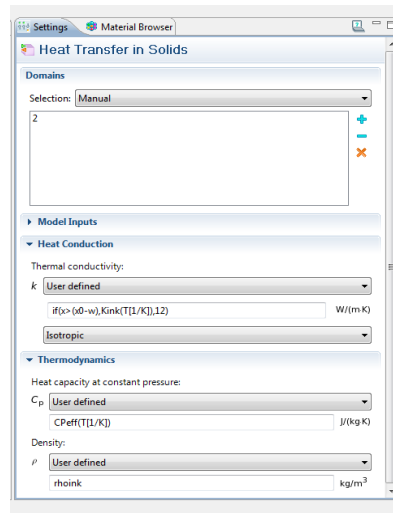
Fig 2.24 Editing the physics (differential equations).

After selection of materials, the physics of the system will be defined through a set of differential equations and boundary conditions. This is achieved by editing in the built-in modules previously selected. As shown in Fig 2.24, each parameter involved in the differential equation can be set to default or User Defined.

Predefined parameters and variables are substituted into each physics module for every geometry domain respectively, which includes the appropriate initial values and boundary conditions (Fig 2.25).
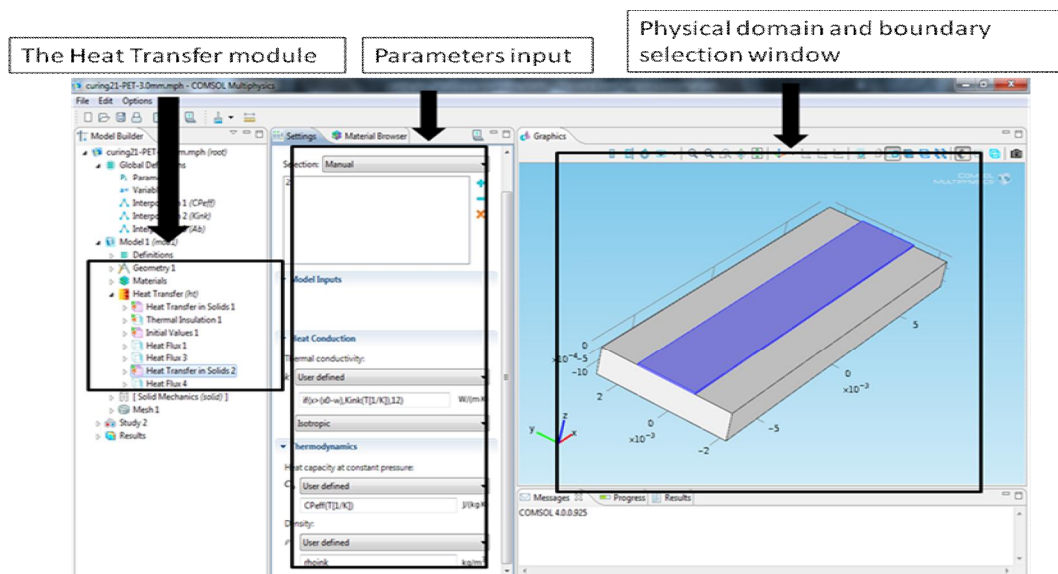
Fig 2.25: Application of Physics and boundary conditions in COMSOL 4.0

2.6.2.4 Meshing
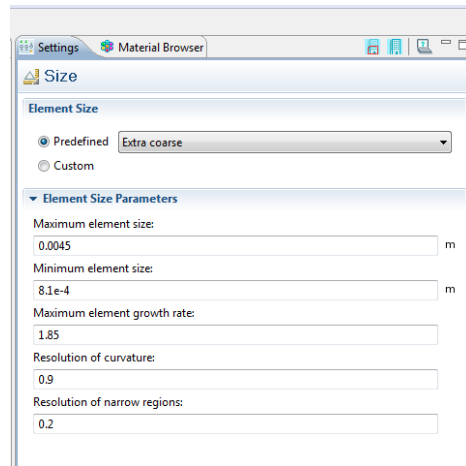
Fig 2.26 Meshing parameters

In the Meshing tab, the user can choose either predefined mesh, or custom mesh. In either case the element size, resolution and element growth rate can be found in the editing field. The Predefined mesh ranges from Extremely Fine, Extra Fine, Finer, Fine, Normal, Coarse, Coarser, Extra Coarse to Extremely Coarse, giving increasing element sizes. A coarser mesh would result in less calculation time and more mathematical error, as previously discussed in Chapter 1.2.2.4.
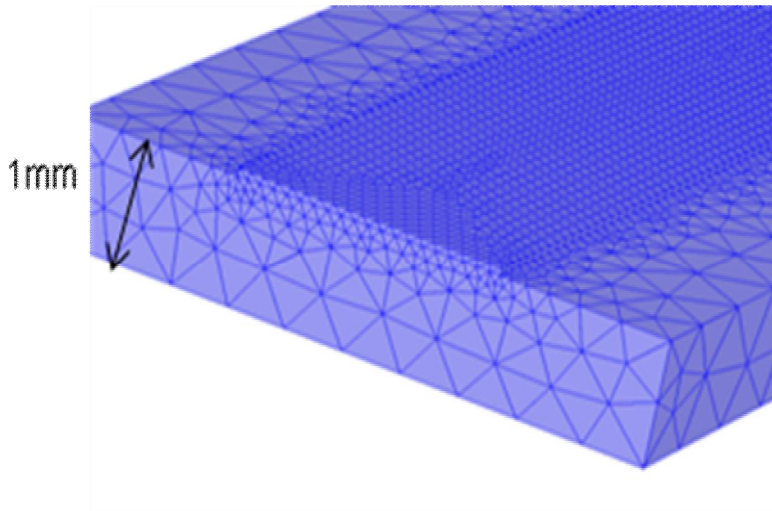
Fig 2.27: Meshing in COMSOL 4.0 propagation

In order to flexibly and efficiently achieve good accuracy over the entire geometry, free tetrahedral has been chosen as the mesh style for this 3D time dependant problem. The entire

system can then be solved after constructing the global sparse matrix obtained by combining the local matrices. The dimension of the global sparse matrix is equal to the total number of nodes in the system. As shown in Fig 2.27, the thin film of ink is meshed with very small elements and the mesh size increases rapidly as it goes through the PET substrate, reducing the total number of nodes and thus minimise the amount of calculation. COMSOL provides both automatic and user defined adjustment for mesh refinement and growth rate and thus allows accurate yet time efficient numerical solutions.

2.6.3 Interpretation of result

Results can be organised into data sets and exported as graphs, different types of plots, numerical values and videos.

The results induced solution for all of the physics involved, stored as data sets. One or more quantities be selected and displayed as colour fields, vectors, contour lines etc. The numerical results can also be exported as data files, images and videos. Comsol also provides enhanced analytical features focused on cross-sections, lines and points. Fig 2.28 shows the temperature distribution of the sample after curing, as a colour field.
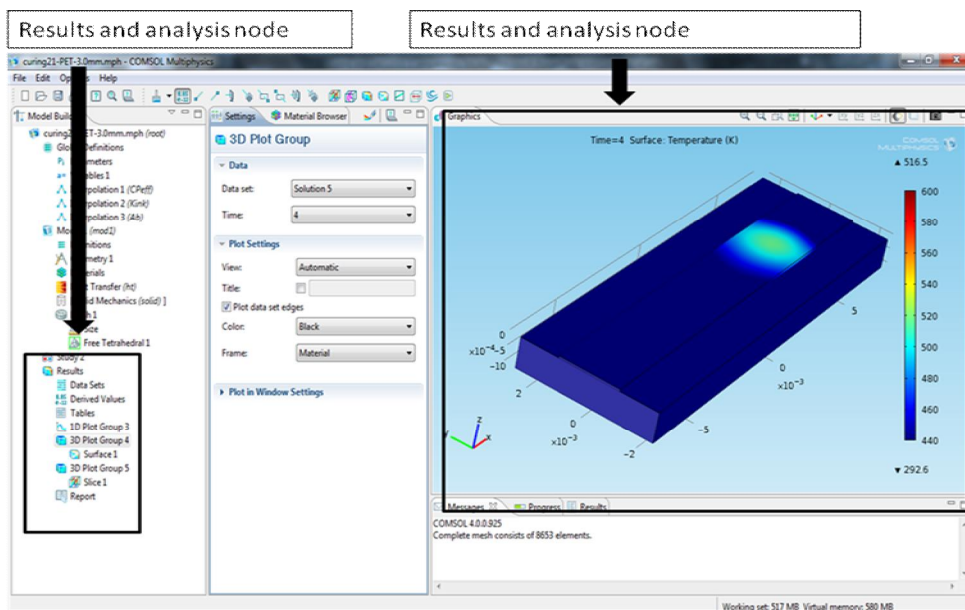
Fig 2.28: Interpretation of result
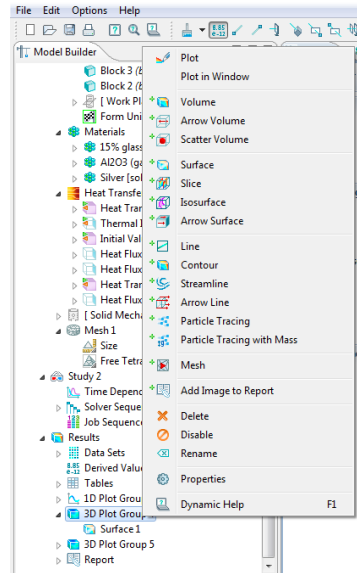
Fig 2.29 Options of result illustration

Comsol provides powerful graphical interface for results illustrations. As shown in the Fig2.29, many kinds of 3D plots can be easily achieved, including Volume, Arrow, Surfaces, Slice, Contour, etc. The plots can be superposed onto each other, and easily hidden or removed if not desired.
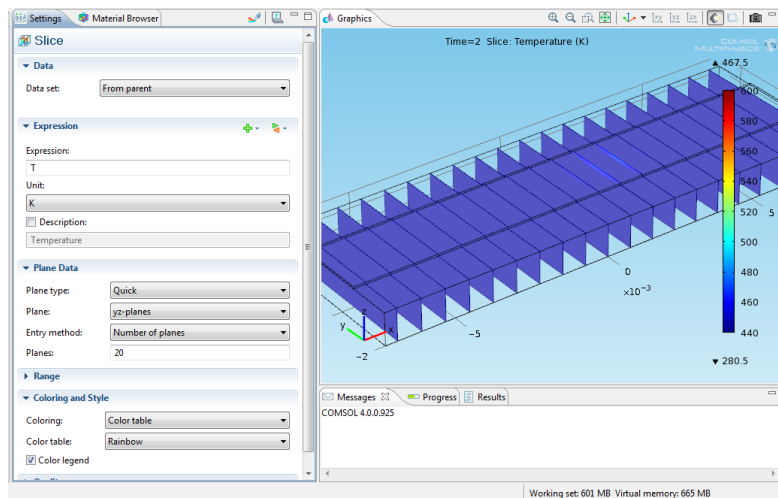
Fig 2.30 Slicing of sample to illustrate results.

Fig 2.31 shows an example of a sliced plot. In this plot one can also see the temperature scale beneath the surface. The slicing parameters can be easily edited as in Fig 2.30.
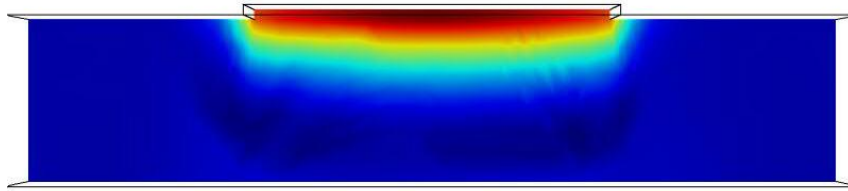
Fig 2.31 Sliced cross sectional views of results.
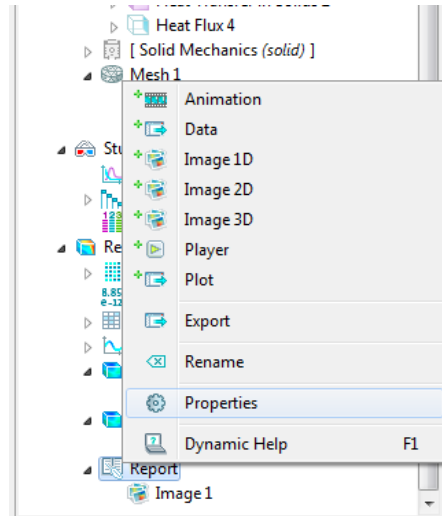
Fig 2.32 Available options for exportation of results.

To integrate the results with other computational or graphical tools for further analysis, one can also export the results from Comsol in the format of 1D, 2D or 3D images, data files and videos, shown in Fig 2.32.

3.Experimental procedure

3.1 Introduction

The experimental part of the work is divided into three main sections:

The FEM model was firstly constructed based on a set of processing parameters of an ink (referred to as õ the generic inkö hereafter) that approximates the properties of D58 ink. A parametric map was then produced by running simulations of this generic ink. in order to verify the accuracy of the FEM model, LADW results with actual D58 ink are compared with the model output.

After the success of the first part, the effect of different intensity profiles was investigated. Different beam profiles was inputed into the model, then simulated and compared with experimental results, demonstrating the improvement that can be achieved in terms of curing quality.

Finally, GEM [217] provided another type of ink, namely the D1 carbon ink, which was used to verify the validity of the model for different types of ink of very different composition and resistivity. A curing window of the D1 ink on alumina substrate was obtained with simulation, which was then again compared to experimental results, indicating that the principle of the model was once again proved.

This chapter details the equipment, materials and experimental procedures used through the body of work presented in this thesis. The laser systems, deposition systems and other devices essential for the completion of the work are introduced in this chapter. The physical and thermal properties of the materials used are also outlined; Finally the procedure of the invetigations and the analysis are detailed.

3.2 Equipment

3.2.1. Synrad laser marking system

The Synrad CO_2 laser marking system (Fig 3.1) consists of a Synrad Series 48-2 Laser and a DH Series Marking Head. The Series 48-2 Laser is an air-cooled sealed unit. It outputs a continuous wave of 10.6 micron wavelength, with tuneable power of up to 25 W. Linearly polarised laser beam of TEM_{00} mode is delivered into the scanning head. As illustrated in Fig 3.1, samples are placed on a stage, with manually controlled vertical position. The user then

generates a sequence of jobs in the geometrical interface of the marking system, Synrad WinMark Pro, as shown in Fig 3.2. This interface consists of a menu bar, a tool bar, a drawing canvas and an operating window. This software allows easy generation of a wide range of simple geometrical shapes such as lines, squares, triangles, circles, etc. Text images can also be readily generated or imported into WinMark. In operation, the user firstly defines the geometrical shapes and a job sequence. The CNC controlled scanning head will then deliver the laser onto the samples to mark out the 2D patterns designed in the WinMark interface.
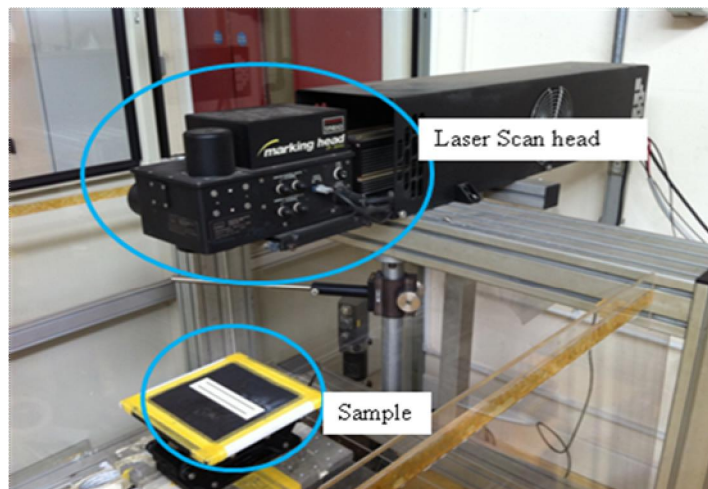
Fig 3.1: Synrad CO_2 Laser marking system
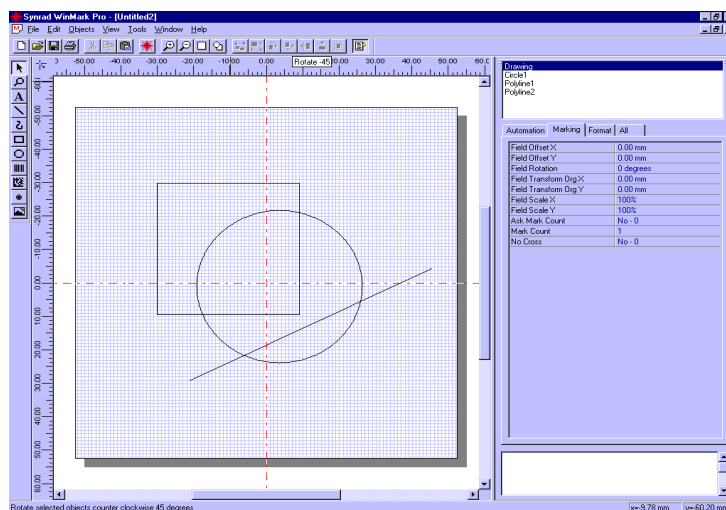
Fig 3.2: Screen shot of the Synrad WinMark Pro, the graphical interface of the Synrad laser marking system

3.2.2. Fluid dispensing equipment
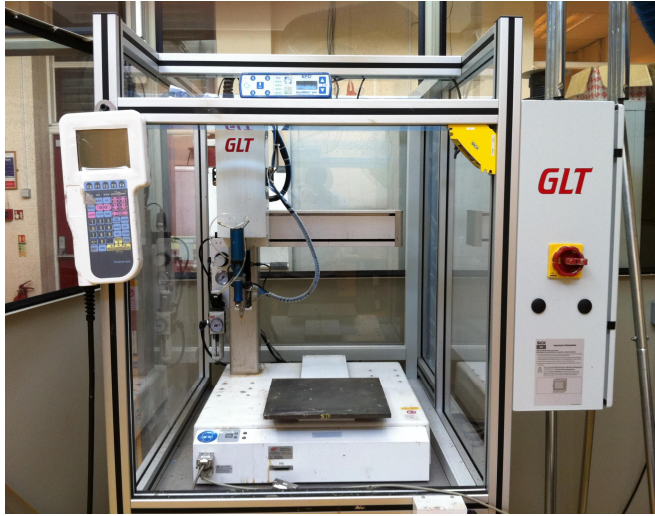
Fig 3.3. The GLT.JR2400N desktop 4 axis CNC deposition system

The Janome Desktop JR2400N, made by GLT, is a high performance, semi-automatic CNC system, shown in Fig 3.3. It has 3 linear axes of movement, and positioning accuracy of 0.01 mm. It has many applications including Screw fastening, Pick and Place, PCB Routing etc [218]. However in this work it is only used for dispensing. The system has many advantages [218] in terms of its

- Compact Size: The JR2400N Series Desktop CNC systems are designed to minimize footprint and maximize efficiencies in assembly line operations.

- Application specific software: The PC Software allows the end user to program an infinite number of programs and download them to the CNC system as needed. JR C-Points also includes a compiler to convert .dxf files into .jcs format, which is the CNC system's resident file.

- Improved memory capacity: The JR2400N Series has a memory capacity of 255 programs and 30,000 points.

- Simultaneous control of all axis: The JR2400N Series desktop CNC systems are capable of simultaneous control of up to four axes. The system performs 3D linear and arc interpolations to include compound arcs.

As shown in Fig 3.4, ink was firstly loaded in the syringe unit. Gauged gas pressure was applied to the top of the syringe to drive the flow of ink down. The bottom of the syringe is

connected to an EFD fluid dispensing tip. Samples were placed on the X-Y table. The movement of the CNC system is principally controlled by a PC. Positional information probed by the tip can also be fed back to the computer.
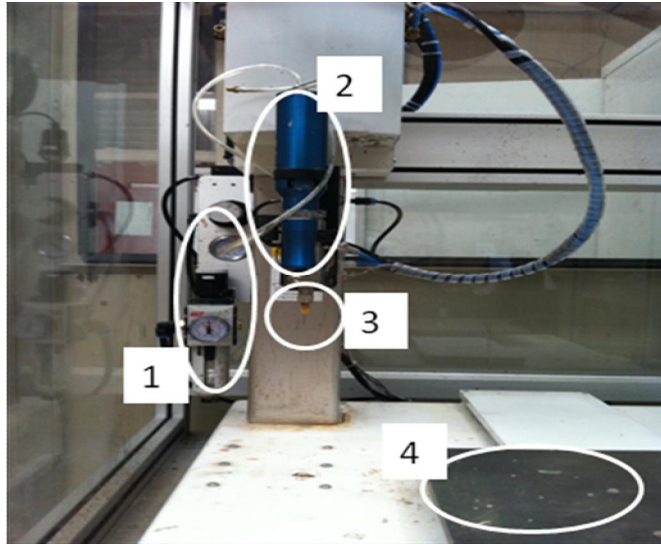
Fig 3.4. 1) Gas Pressure control. 2) Syringe unit. 3) Dispensing nozzle tip. 4) CNC controlled X-Y stage

Ink was then delivered through the tip onto the sample to make an ink track. Fig 3.5 shows the gas delivery pipe and the syringe used as the ink carrier.

Fig 3.5. The syringe unit and gas pipe
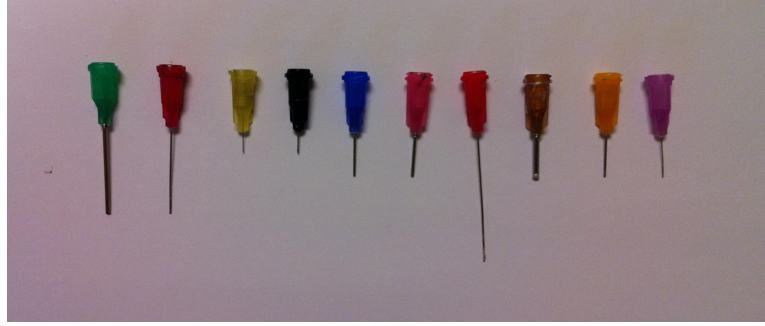
Fig3.6. The range of dispensing nozzle tips available

There are a variety of different sized nozzle tips, which would result in different flow rate and deposition geometry. Fig 3.6 shows the range of nozzles available. Each nozzle has its own gauge number which specifies their inner diameter, this is represented by the colour of each tip physically, as listed in Table 3.1. Type and size of the tip can be varied to suit any particular application.

Table 3.1. Dispensing nozzle tip Gauge numbers and Colour codes

Gauge	ID (mm)	Colour code
14	1.55	Olive
15	1.37	Amber
18	0.84	Green
20	0.61	Pink
21	0.51	Purple
22	0.41	Blue
23	0.33	Orange
25	0.25	Red
27	0.20	Clear
30	0.15	Lavender
32	0.10	yellow

To build a ink track pattern, CAD drawings were firstly imported into the Visual PathBuilder V3.4 software, which converted the geometrical line pattern into a sequence of vector movements, illustrated in Fig 3.7. The vectors were then mapped into a coordinated path in

the JR C-Points software for dispensing (shown in Fig 3.8). The JR C-Points directly controls the movement of the CNC system, and dispensing of the ink.
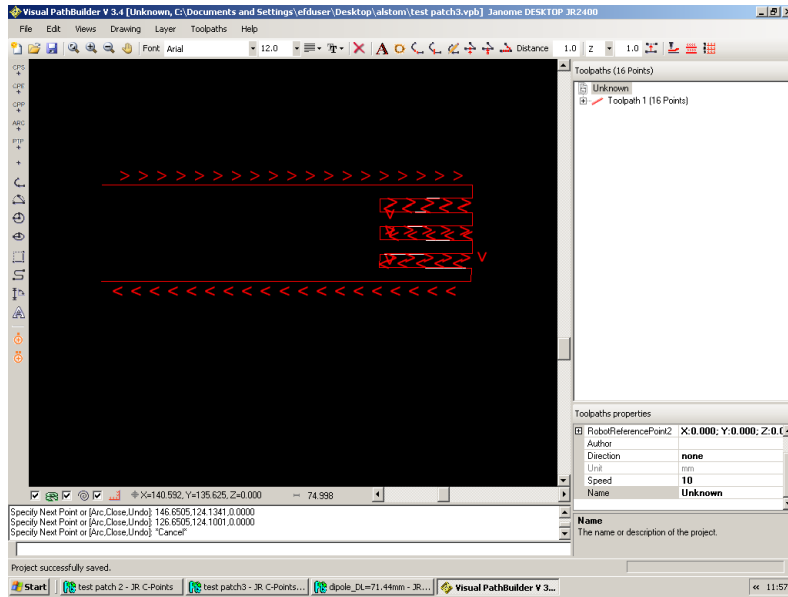
Fig 3.7. Screen shot of the Visual PathBuilder V3.4 software
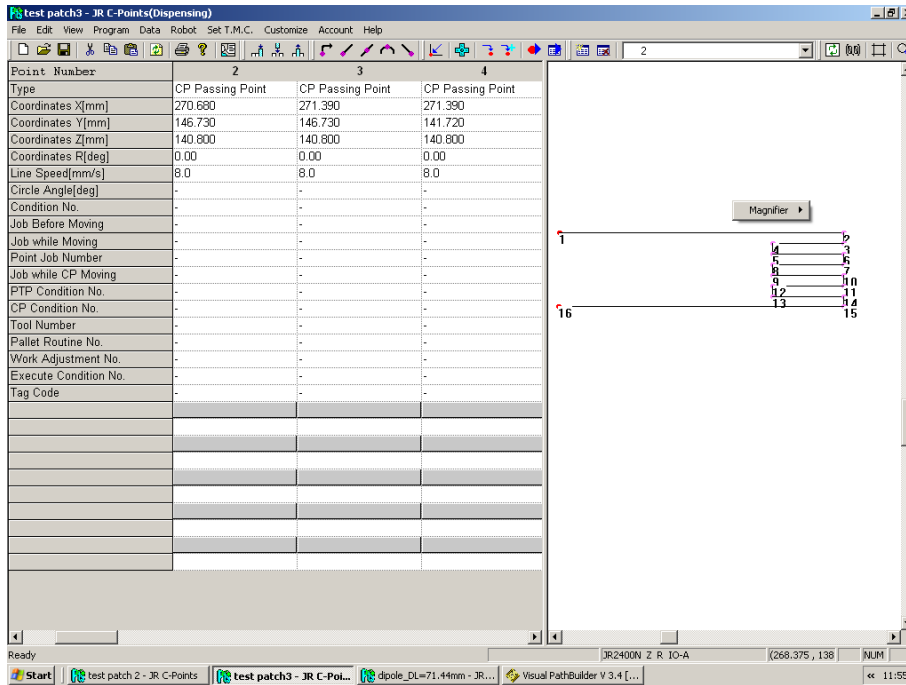
Fig 3.8. Screen shot of the JR C-Points software for dispensing

3.2.3 The SunShaper

Fig 3.9.The SunShaper beam shaping device.

SunShaper is a refractive laser beam shaping device capable of transforming a collimated Gaussian laser input beam into a filled annular ring of varying proportions (Fig 3.9).This device was invented by Dr Dan Wellburn in the Laser Group of University of Liverpool [18]. It utilises refractive surfaces in conjunction with a novel beam modulation mechanism to produce a range of intensity profiles based around a focussed annular ring. The annular ring may be accompanied in varying amounts with a plateau intensity fill in its centre. The level of this fill is determined by the lens separations within the beam shaping device, which is easily manually controlled by turning the calibrated junction.

The particular unit used in this case is designed to convert an input CO_2 Gaussian beam of diameter 9 mm into a shaped profile of diameter 2.55 mm. The annular ring profile has a peak to peak distance of 2.3 mm and an annular ring spread (the peak to where the intensity falls to $1/e^2$ of the main peak) of 0.125 mm. The device is capable of producing a central plateau intensity fill of between 0 and 50%. The SunShaper is currently under application of a patent[219], therefore no further technical details can be revealed beyond the operation principle of this device. The author has been given special permission by Wellburn [18] to publish the basic principle of this device.

The SunShaper is designed to transform an input beam with a Gaussian intensity profile into a focussed annular ring with a central intensity feature which is variable in its relative

magnitude to the maximum amplitude of the annular ring. The underlying principle of the device mainly relies on manually controlled separation of an Axicon lens pair (Fig 3.10). Via a simple variation in the spacing of the optics, the SunShaper may produce a range of intensity profiles at the work piece from an annular ring with no central intensity fill to one with a relative fill of 50% or more. The range of profiles achievable is shown in Fig 3.11 below:
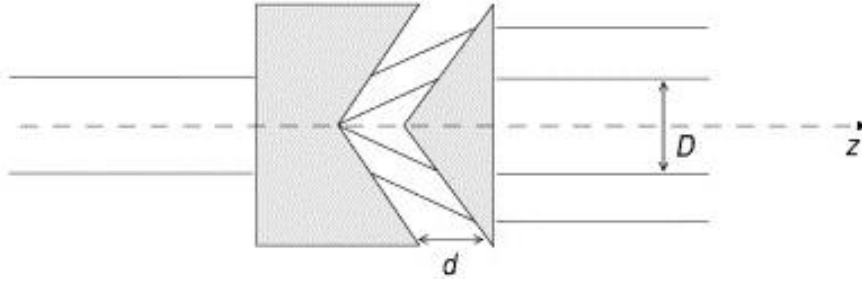
Fig 3.10. The operation principle of the Sunshaper is to produce different beam profiles by varying the spacing between a pair of aligned Axicon lenses [20].
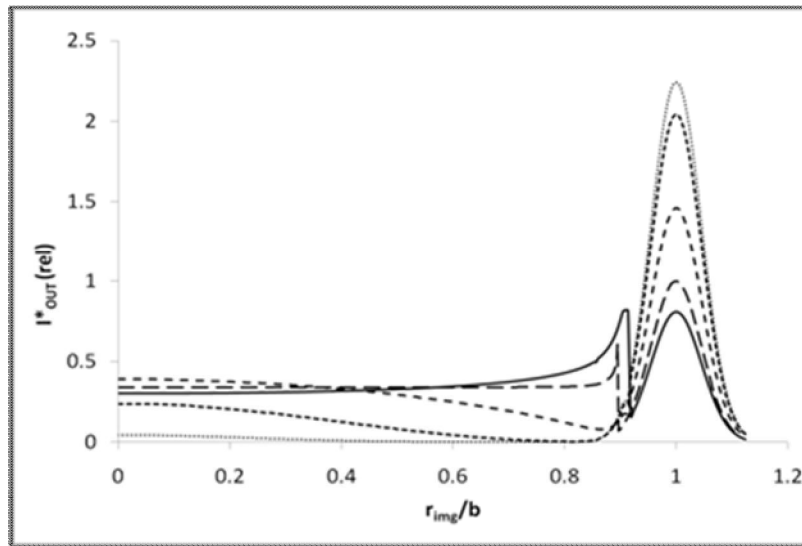
Fig 3.11.Different beam modes produced by the SunShaper [18].

3.2.4. The Solsurf laser processing system

The Solsurf laser processing machine (Fig 3.15) is a system which allows the dynamic application of a laser beam on the surface of a 3D part. The machine consists of six motion axes (3 linear axes and 3 rotary stages), a 300 W CO_2 laser and a process motion controller. This system is designed and built in-house in the Laser Group, University of Liverpool. The axes are grouped together in a configuration to perform 3 dimensional part manipulations and positioning. The range of the linear axes are X-150 mm, Y-150mm, Z-200 mm. Each has accuracy of 12 microns [220]. As illustrated in Fig 3.12, The Solsurf system has its datum point located at the intersection of the three rotary axes. This feature enables full 3D part manipulation in a compact space. The Solsurf is a modified system based on the concept developed by Cybaman Ltd [220].
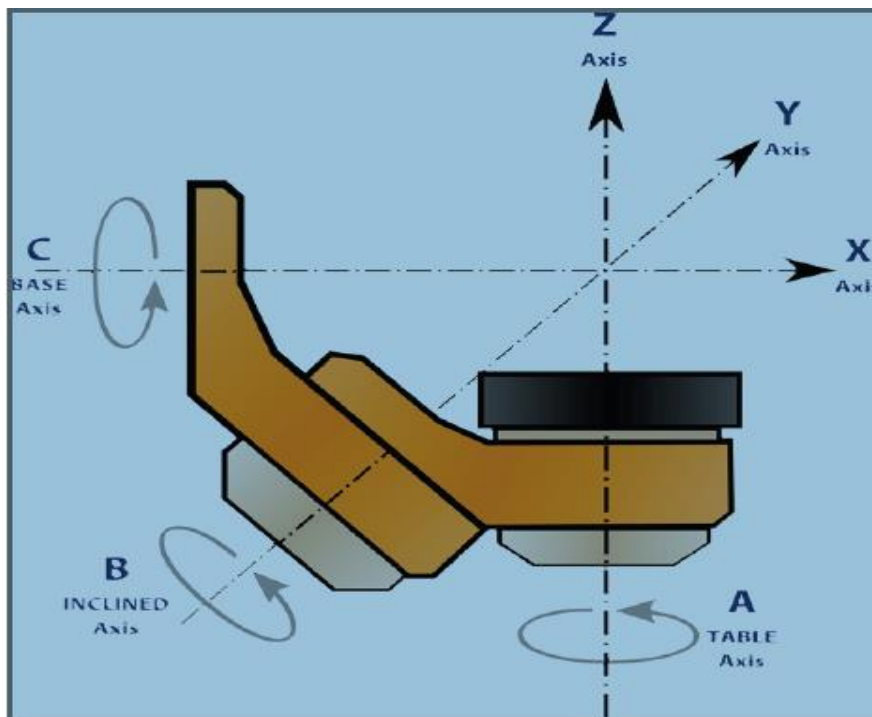
Fig 3.12. The datum point of the Solsurf is at the intersection of the rotary axes.

The Rofin SC x 30 Sealed CO_2 Slab Laser can produce 5-300 W of average power. The pulse length can be varied from 5 to 200　s. Therefore with a repetition rate higher than 15 KHz,

the laser becomes pseudo-CW. The laser units are of a compact, rugged design as a result of their propriety diffusion cooled RF excited slab construction [221]. This produces a high quality round, symmetrical beam. The hard sealed construction of the laser tube ensures long gas lifetime, with virtually no maintenance requirement. The elimination of an independent gas supply has the added benefit of removing the contamination source for the cavity optics and output window.

A specifically designed control unit integrates the Rofin laser, the processing gas valve and the 6-axis machine together. It utilises the standard Aero-tech A3200 controller[222], which is an excellent platform for user-developed add-on functionalities. The user interface is the NView HMI (2.19) software.

In the manual user interface, a user can operate the motion axes, processing gas switch and the laser; alternatively. One can write a G-code programme script and run it in the execution interface, shown in Fig 3.13-14.
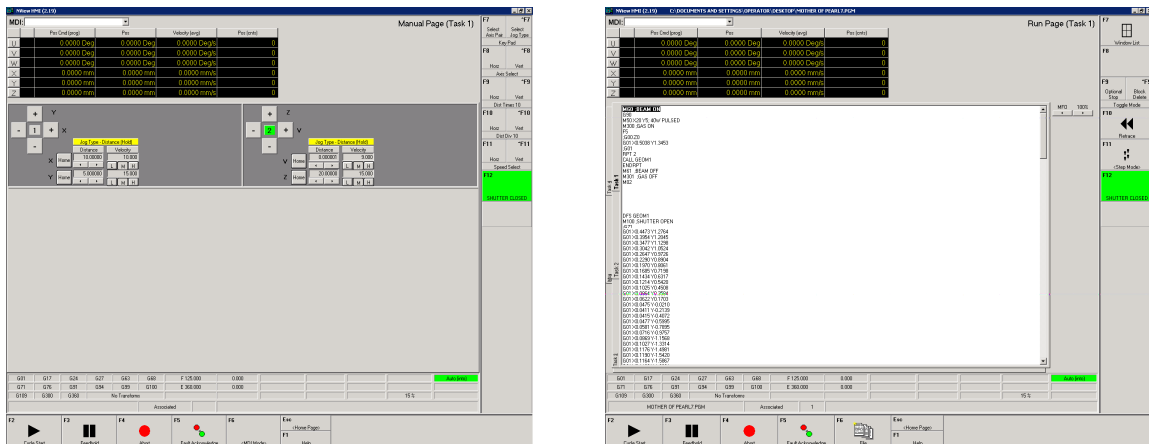
Fig 3.13-14. The NView HMI (2.19) manual and G-Code programmable interface

In Fig 3.15, the 9mm diameter CO_2 laser beam firstly goes through the attenuator, which reduces the beam size to 8mm, then mirror delivered into the SunShaper. The shaped beam profile from the SunShaper was used to process samples placed on the pellet of the Solsurf system.

The ink track was placed under the focus of the shaped beam, the sample was then cured by moving the stage along the direction of the track at a specific speed.

3.2.5. The beam intensity attenuator

Brewster plates to eliminate lateral beam deviation, and to allow internal dumping of unwanted laser power. The unit has a clear aperture of 33mm diameter, can stand up to 2000 W of CW power. Transmission of 6%-100% can be easily achieved by simply rotating the Brewster plate pair. When used with over 100W of input power, 3 litres per minute of water flow through the water-cooling jacket was required to restrict temperature rise of 5 ^{o}C.
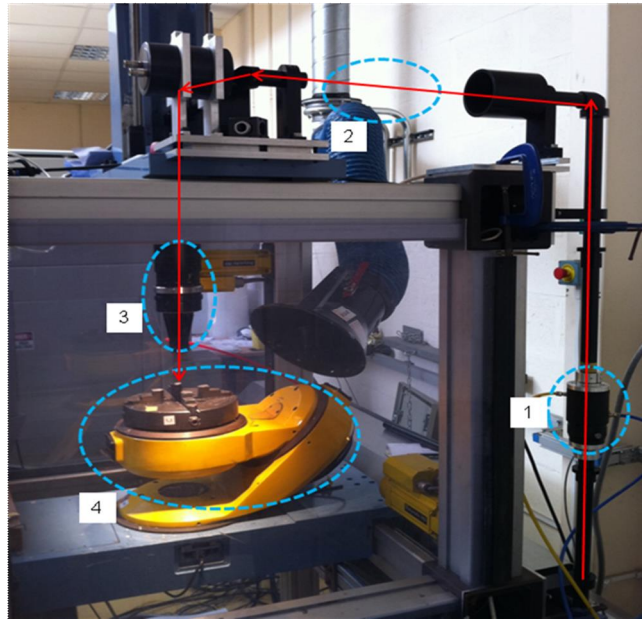
Fig 3.15. The Solsurf system: 1) Attenuator unit. 2) Laser beam paths. 3) Sun Shaper. 4) CNC Stage.
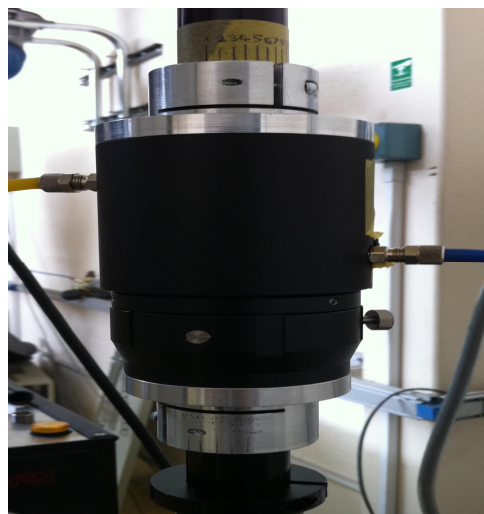
Fig 3.16. HPA20 CO_2 Laser beam attenuator manufactured by ULO Optics

The attenuator used was Model HPA20 manufactured by ULO Optics[223] for attenuating linearly polarized high power laser beams, shown in Fig 3.16. The unit contains two ZnSe As illustrated in Fig 3.17, the attenuator was operated on calibrated rotation of the Brewster plate pair. The input linearly polarised beam then partially passed through, leaving some energy dumped in the attenuator.
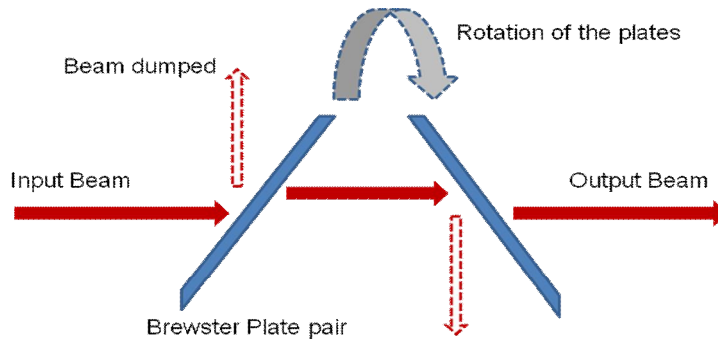
Fig 3.17. Schematics of the operation of the attenuator

3.2.6. The LaserDec beam analyser

The LaserDec CL200 system was used for examining the intensity profiles obtained with the SunShaper. This is a compact and portable system, designed for monitoring high-power CO_2-lasers beam profile. It utilises a unique imaging technique based on a screen converting 10.6 micron light into NIR radiation. A high quality CCD camera that is sensitive to NIR wavelength is used to acquire and measure the converted light in real-time. The CL200 model is suitable for a laser beam with diameter ($1/e^2$) in the range of 1mm - 10mm, and power up to 200W. The CCD camera of the unit has a resolution of 752 x 580 pixels [224]. The shaped beam can be directly focused onto the CCD camera of the LaserDec, as illustrated in Fig 3.18, to obtain the exact intensity distribution required.
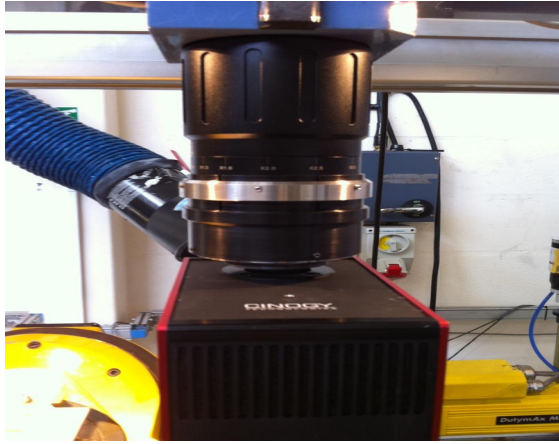
Fig 3.18. Using the LaserDec to analyse the output of the SunShaper.

The LaserDec system was operated through the specifically designed analysis software, RayCi. Users can access standard settings with the self-explanatory functions on the interface. The comprehensive visualization modes and analytical capabilities allow high accuracy laser beam analysis. A wide range of beam width techniques (e.g. Knife Edge, Moving Slit, Plateau and Gauss-Fit) can be applied to determine standard beam parameters. Also, continuous monitoring of beam parameters, beam position and power density distribution are enabled. RayCi can output data and images flexibly. A clearly arranged and printable protocol view displays the chosen measurement parameters as well as the most important laser beam analysis results, as shown in Fig 3.19.
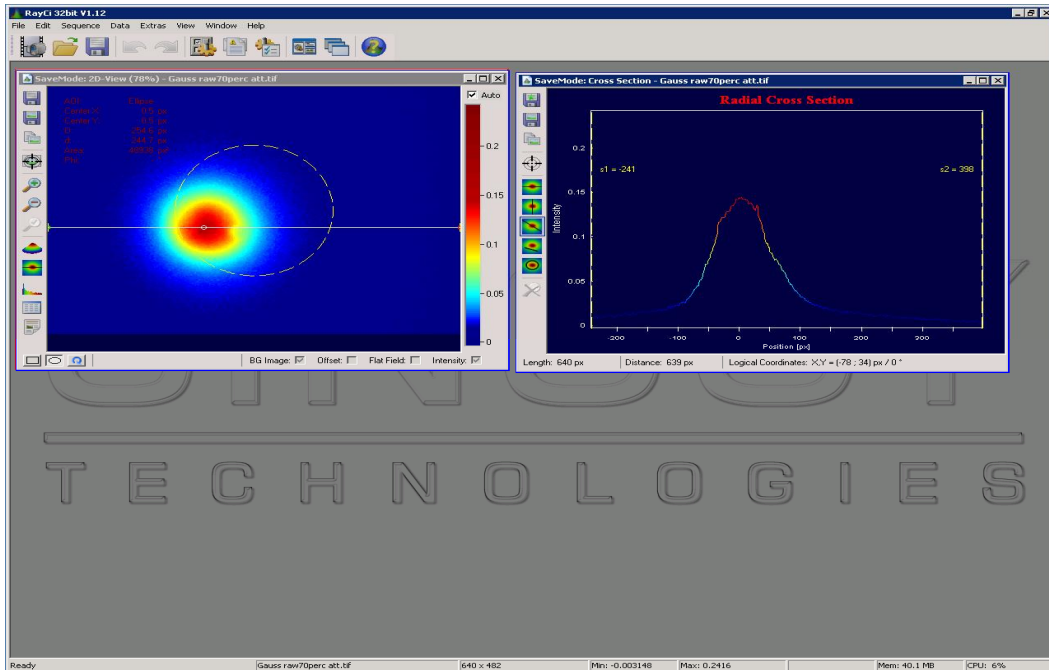
Fig 3.19. Screenshot of the RaySci software, which is used for analysis of the beam profiles captured by the LaserDec system.

3.2.7. The Elcometer pencil hardness tester

Another measure for the quality of curing is the hardness (or scratch resistance) of the cured ink track. The Wolff-Wilborn method was used for testing this. The full description of this method can be found in BS 3900-E19, ISO 15184 and ASTM D 3363-92a.

The purpose of the Elcometer 501 Pencil Hardness Tester is to provide a rapid, inexpensive method for determination of the comparative scratch resistance and hardness of a coating.
As shown in Fig 3.20, a cured sample is placed on a firm horizontal surface and the pencil is held firmly against the track, point away from the operator, at a 45° angle. The pencil is then pushed away from the operator. The hardness of the pencils is increased until plastic deformation or cohesive fracture occurs. The equipment used in this test was the Elcometer 501 Pencil Hardness Tester, which uses standard wooden black lead pencils, and is supplied with a full set of fourteen, covering 6H (very hard) to 6B (very soft)[225].
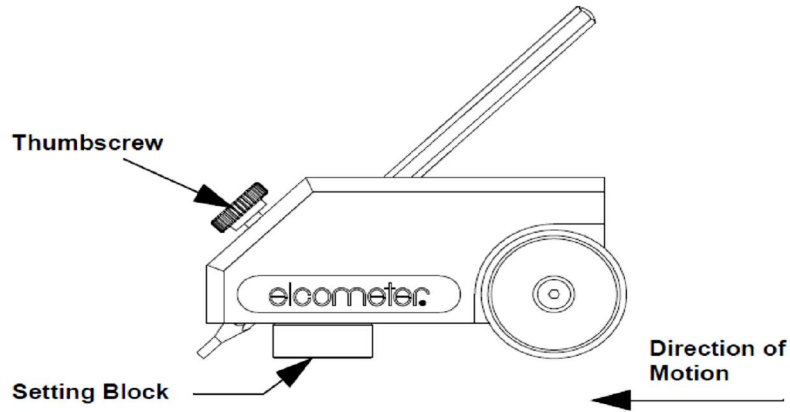
Fig 3.20.The Wolff-Wilborn method.

3.2.8. The Digimess RLC meter

The resistance of cured samples was measured with the compact Digimess RLC Meter. This device can measure resistance, inductance and capacitance of the cured ink track to 1% accuracy. To measure the resistance of a cured ink track, the probes are held in firm contact with the track, and the result is shown by readings on the display (Fig 3.21).
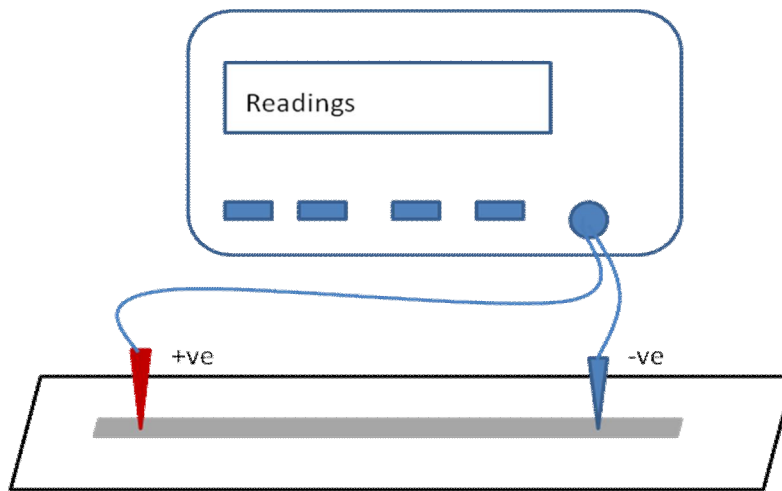
Fig 3.21. Schematics of using the RLC meter to measure sample resistance

3.3 Materials

3.3.1 Inks

The inks used in the experimental part of the study are D58 and D1 ink manufactured by Gwent Electronic Materials Ltd (GEM). Ink was kept in a sealed carton and stored at room temperature (20 ^{o}C). D58 and D1 are part of a range of heat curable inks that are based on a unique curing process that results in the low temperature formation of thermosetting polymer [15]. D58 has a silvery paste-like appearance, while D1 is completely raven black; They both have a viscosity of 6.5-8.5 Pas. These inks provide excellent adhesion to various substrates, with good chemical and environmental resistance [217].

3.3.1.1 Properties of ink components

The components of the conductive inks supplied by GEM include the following:

Silver Flake:

High density, low surface area conductive silver flakes manufactured by Ferro Electronics Material Systems [226], has been used as the conductive media in the D58 ink.

Conductex SC:

Conductex SC is a black, odorless, insoluble powder manufactured by Colombian Chemicals It is a high purity conductive furnace carbon with exceptionally low levels of ash and residue and intermediate conductivity [227].

Timrex:

Timrex is a family of commercial high purity graphite powder. Graphite is characterized by having a crystalline structure made of carbon atoms organized in planes of regular hexagons. These planes are parallel to each other and have a very well defined relative orientation. [228].

Epikote:

Epikote resin is an epoxy resin produced from bisphenol and epichlorohydrin. The resin is available in the form of a viscous, transparent solution. Applications include coatings for the protection of metals and concrete. Also can be used as a modifier in stoving enamels based on acrylic resins or alkyd/melamine resin systems [229].

Trixene:

Trixene is a viscous solution prepolymer, based upon Toluene di-isocyanate. It can be used in single component moisture curing priming and sealing applications for a wide range of substrates. The products are available in a range of solvents and solvent concentrations. Typical applications include concrete primers and anti-corrosion coatings for various substrates including steel and aluminium.

Glycerol:

Glycerol (or glycerine) is a simple polyol compound. It is a colorless, odorless, viscous liquid that is widely used in pharmaceutical formulations. Glycerol has three hydroxyl groups that are responsible for its solubility in water and its hygroscopic nature. Glycerol is sweet-tasting and of low toxicity. Applications include: food industry, pharmaceutical, surface science, botanical extracts and chemical intermediaries.

Methyl Carbitol:

Methyl carbitol glycol ether is a very hydrophilic, slow-evaporating glycol ether. Its primary use is as a de-icing additive for aviation fuel. Methyl carbitol glycol ether can also be used in coalescing blends with other solvents where high polymer solvency and is needed.

Due to its powerful solvency, low surface tension and low evaporation rate, Methyl Carbitol has been used as active solvent for silk screen printing inks, stamp pad ink and ball point pen inks [230].

Butyl Carbitol:

Butyl carbitol glycol ether can be considered a slow evaporating glycol ether. It can be used in combination with butyl cellosolve glycol ether to lower the evaporation rate and increase the hydrophobicity of the solvent package. Powerful solvency and coalescing ability make butyl carbitol an excellent coupling solvent for resins and dyes in water-based printing inks [230].

Table 3.2: Ink components and their physical properties. (NA means "Not Applicable", and "STA" means properties later determined with STA analysis)

Component Name	Function	Density (kg/m3)	Specific Heat Capacity (J/kg*K)	Latent Heat of Vaporisation (J/kg)	
Epikote	resin	1.19E+03	STA	NA	
Trixene	resin	1.03E+03	STA	NA	
Methyl Carbitol	solvent	1017	2300	369000	
carbon	conductance	1800	STA	NA	
Timrex/graphite	conductance	2267	710	NA	
Glycerol	solvent	1261	STA	974000	
Butyle carbitol	solvent	948	2260	276000	
Ag flake	conductance	10500	250	NA	

The physical and thermal properties of these components are listed in Table 3.2. Some of the properties are non-applicable; and some are not available through open resources and therefore can only be determined with STA analysis later in the study.

Table 3.3: Indicative ratios used in the silver and carbon thermosetting formulations.

	Product Code	similar to D1
RM183	Glycerol	1
RM133	Conductex SC	15.00
RM132	Timrex KS15	15.00
	R2050309D9	35.00
RM306	Trixene BI7963	20.00
RM195	Methyl Carbitol	15.00
		100.00

	Product Code	R2050309D9
RM 297	Epikote 1007	50.00
RM 195	Methyl Carbitol	50.00
		100.00

GEM also provided the indicative mixing ratio for mixing carbon inks similar to D1. This provides a guideline of the composition of D1 ink. Note that the component R2050309D9 is usually mixed with other components as a pre-existing product, which consists of Epikote and methyl carbitol to 50% weight percentage each.

3.3.1.2 Principles of DSC, TGA and STA

Differential Scanning Calorimetry

Differential Scanning Calorimetry (DSC) is a technique used to study thermal transitions of a polymer. It measures the temperature and heat flows associated with transitions in materials as a function of time and temperature in a controlled atmosphere. These measurements provide quantitative and qualitative information about physical and chemical changes that involve endothermic or exothermic processes, or changes in heat capacity.
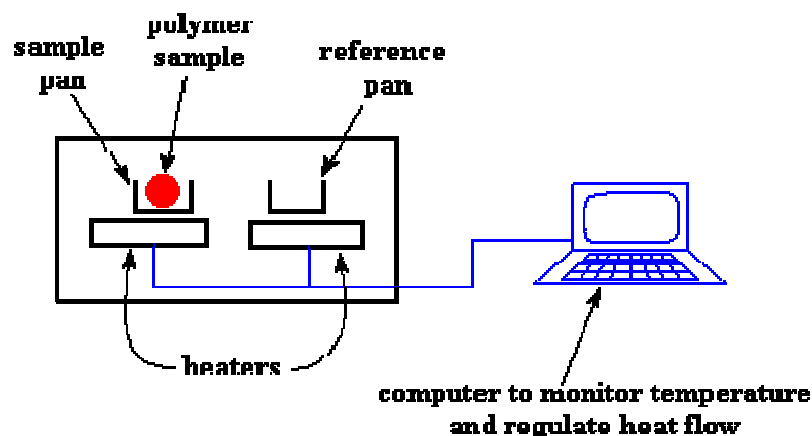
Fig 3.22 Schematics of DSC set-up.

DSC heats a polymer sample with a linear temperature ramp and measures the heat into or out of a sample relative to a reference. Fig 3.22 shows the basic set-up. There are usually two pans, each positioned on top of a heater that is controlled by a computer. The polymer sample is placed in the sample pan. The other one is usually left empty as the reference pan. The heaters are heated at a steady rate throughout the experiment [231-234]. There are a few sources of errors, including calibration, contamination, sample preparation, residual solvents and moisture.

Thermogravimetric Analysis (TGA)

TGA measures the change in weight of a sample as it is heated, cooled or held at a constant temperature.

Simultaneous Thermal Analysis (STA)

STA is a simultaneous technique that determines the weight change of a sample (TG) and measures the change in temperature between a sample and the reference as a function of temperature and/or time (DSC).

3.3.1.3 Perkin Elmer STA 6000 System

The Perkin Elmer STA 6000 system used in this study to combines the high flexibility of the differential analysis feature (DSC) with the proven capabilities of the thermogravimetric (TGA) measurement technology to provide highly reliable characterization information.

As shown in Fig 3.23(a), the system was placed on top of an inflated isolation table to reduce vibration induced errors. Features of the system is listed in Table 3.4

In a STA run, firstly the internal water cooling was turned on. Then Nitrogen gas purge rate was set at ~20ml/min. The purge gas was used to carry the vapour out of the system through the vent [Fig 3.23(c)]. An empty crucible [Fig 3.23(d)] was then placed and weighed on the balance [Fig 3.23(b)]. The reading was then zeroed, enabling the measurement of sample weight later on.

The programmes of the experiment are defined in the method editor of the Pyris software. Fig 3.24 shows an example: The system was heated up from 30 $^{\circ}$C to 250 $^{\circ}$C at the rate of 5 $^{\circ}$C/min. Once it reached 250 $^{\circ}$C, the system was held at that temperature for 10 min, and was then cooled down to 30 $^{\circ}$C at the rate of 10 $^{\circ}$C/min.

Table 3.4: Features and capabilities of the Perkin Elmer STA 6000 System

Sensor	Pure platinum pan holder and reference ring. Corrosion-resistant, making the instrument suitable for a wide variety of samples and applications
Furnace design	Vertical optimized for performance, user exchangeable SaturnA sensor. Ensures even purge gas flow.
Balance design	Top loading, single beam. Easy loading and unloading in manual and automated mode.
Balance resolution	0.1 ug
Temperature range	15 °C to 1000 °C. Start experiments below room temperature to capture complete moisture and solvent evaporation
Heating rate	Ambient to 1000 °C 0.1 to 100 °C/min
Cooling rates	From 1000 °C to 30 °C under 10 minutes Forced air and chiller to achieve fastest cool down for higher productivity.
Temperature accuracy	< ±0.5 °C
Sample pans	Alumina 180 l
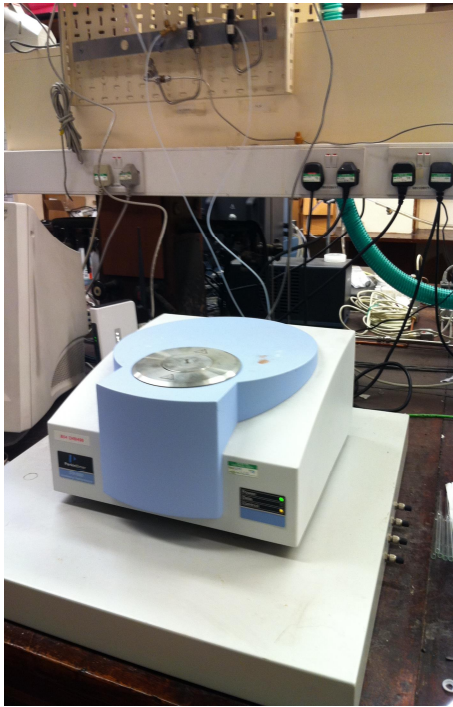
(a)

(b)

(c)

(d)

Fig 3.23 (a) The Perkin Elmer STA 6000 system. (b) Micro-balance and furnace. (c) Vent on top of the furnace. (d) Alumina crucible sample carrier.
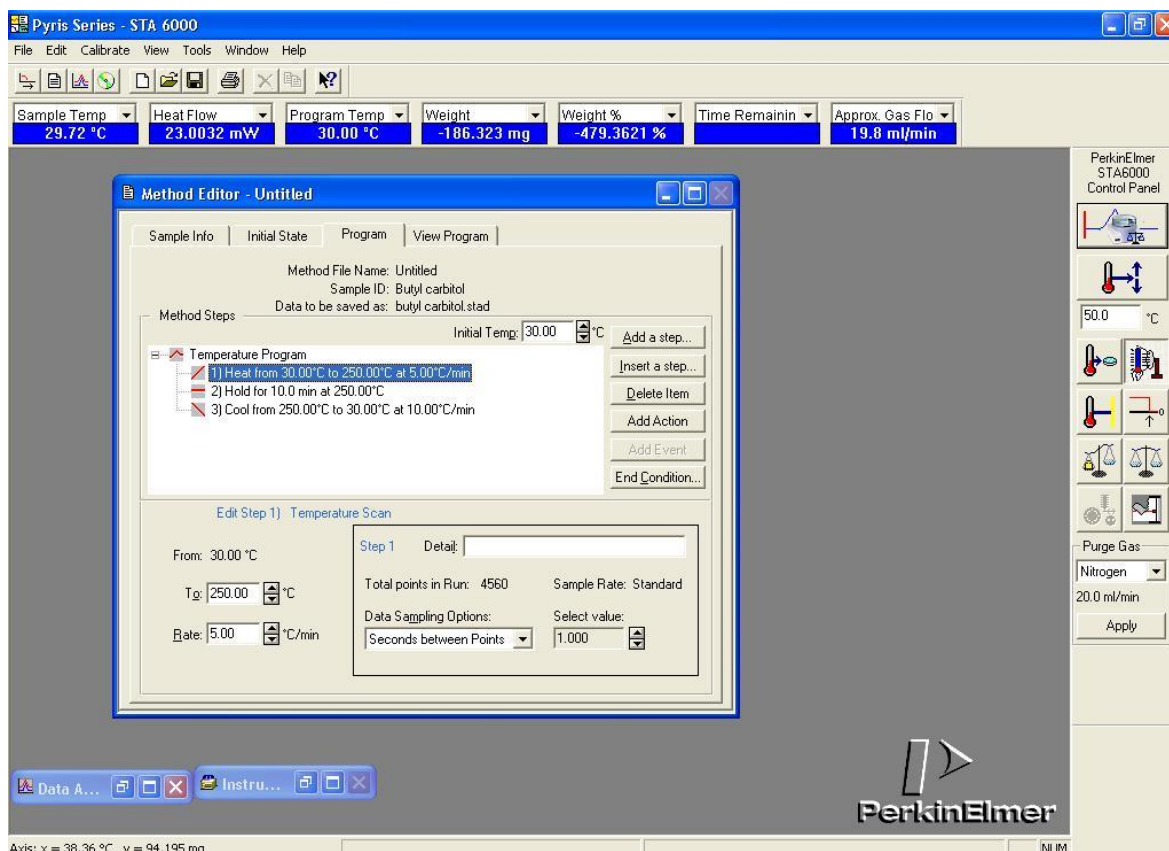
Fig 3.24 The programming interface of the Pyris software interface in which the temperature elevation is programmed.

Fig 3.25 The STA 6000 STA system   Fig 3.26 The sample holding pan
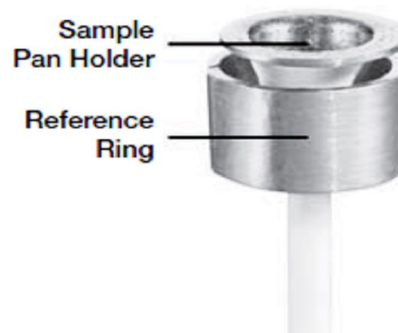
The STA 6000 system provides the following advantages:

1. The small furnace enables accurate temperature control, minimises the time to achieve a pure gas environment and allows for the fastest cool down/ turnaround times.

2. The vertical loading balance allows for easy operation and sample loading.

3. The rugged alumina furnace is corrosion-resistant allowing for a wide variety of reactive gasses to be used.

4. The chiller and integral forced air features enhance furnace cool-down speed and allow more samples to be processed.

5. The balance housingøs stainless steel wall act as a large heat sink, thermally isolating the balance from the furnance.

6. Balance purge gas maintains a constant environment for the balance and protects it from the reactive sample.

7. The integrated controller provides accurate environmental control and specific gas flow rate.

The corrosion-resistant, pure platinum pan holder and reference ring make the instrument suitable for a wide variety of samples and applications. In addition, the mass flow controller enables you to program a fast purge-out of residual oxygen or a quick oxidizing furnace clean at the end of the run, as required for good laboratory practice.

3.3.2 Substrates

The three common types of substrates used were alumina (Al_2O_3), polyethylene terephthalate (Bi-axially orientated PET) and paper.

Alumina was used as a well known dielectric material which is chemically inert and thermally resistant. It also has excellent durability in harsh environments. However, it is rather brittle and tends to break easily under stress.

PET was chosen for its light weight, physical flexibility and elasticity against stress. It can be easily cut or tailored, and economic advantage. The disadvantage of PET is its thermal

sensitivity, which normally result in plastic deformation if extra heat is coupled in during the curing process.

Paper is the cheapest among the three. On the other hand it has virtually no mechanical strength and no resistance to any environment conditions (such as water).

Paper and PET have relatively low thermal conductivity. While Al_2O_3 is considerably more thermally conductive. Therefore the LADW process carried out on Paper and PET is very different from that on alumina.

3.4 Experimental Procedure

Laser curing trials generally start with deposition of a certain ink track pattern onto a substrate, with either the doctor blade method or using a CNC dispensing system. The ink track samples were then shifted onto the laser system for curing, before hardness and resistivity measurements were carried out.

3.4.1 The deposition methods

3.4.1.1 Doctor Blade method

The doctor blade method is a common technique and is similar to that of manual screen printing. A stencil was created which acted as a negative of the image/dimensions desired. The stencil was then flooded with ink and a scraper drawn across the surface of the stencil flooding the negative (gaps) with ink. Once it had been properly flooded and scraped with excess ink removed, the stencil was peeled off the substrate leaving a positive image of ink, Figure 3.27. It is only suitable for simple geometries and in this case it was used to create single lines.

Fig 3.27. Illustration of the Dr Blade method

Fig 3.28 shows an example of a stencil, and the ink track made with this method.
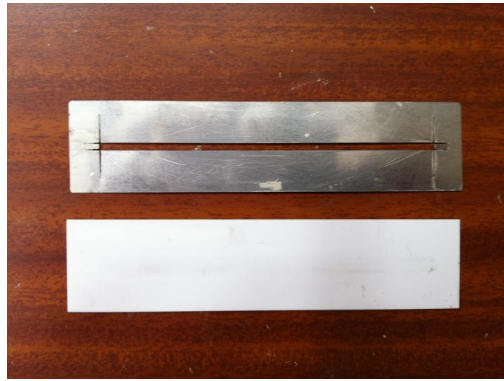
Fig 3.28 a). Stencil used in the doctor blade method
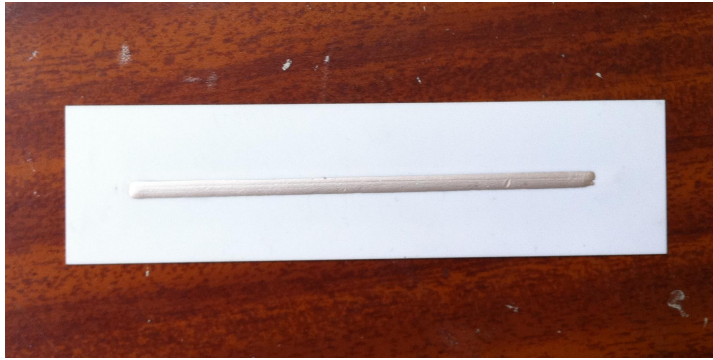
Fig 3.28 b). Ink track sample made with the doctor blade method

This is a quick and traditional method of making sample patterns of regular geometry. The disadvantage of this technique emerges once large quantities or complicated ink track geometry are required. In the later case, a programmable CNC dispensing robot serves the purpose better and is introduced in the next section.

3.4.1.2 CNC deposition with the dispensing robot
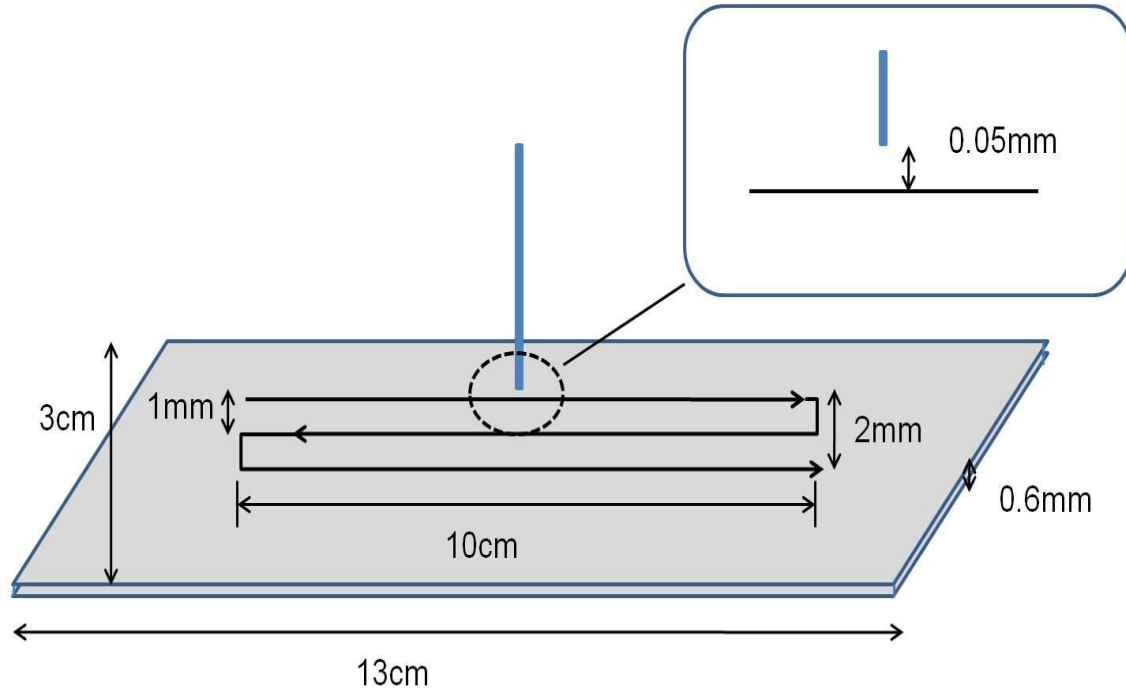
Fig 3.29. Deposition process: the dispensing tip makes a track by following a path defined in the CNC programme.

Fig 3.29 shows a schematic of the deposition process. Firstly the track geometry was imported from AutoCAD into the Visual Path Builder 3.4 software. Visual Path Builder was then used to convert the CAD file into movements of the robot. In this case, a 10 cm long track was deposited on a 0.6 mm thick alumina substrate. The nozzle tip stand-off distance was 0.05 mm; the traverse speed was 10 mm/s. The ink flow was then driven by a tuneable gas pressure, which was kept constant at 20 psi in this study for consistency in deposition.

The nozzle tip used in this study was the gauge 20 tip which has an inner diameter of 61 mm and tip length of 25 mm, as shown in Fig 3.30. This particular size produced the most suitable flow rate at 20 psi, and hence was chosen for this process.

(a)   (b)
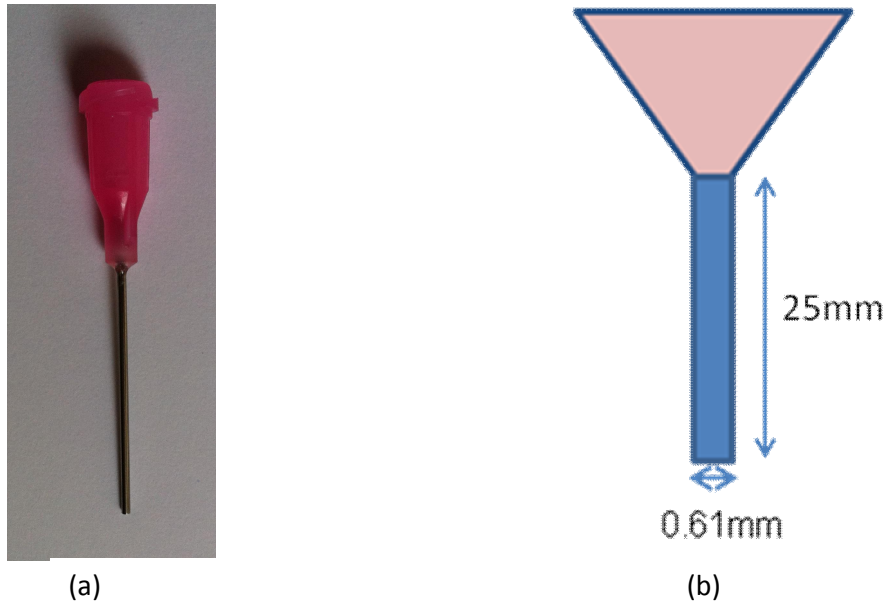
Fig 3.30.(a) EFD fluid dispensing tip (b) Tip dimensions

This process produced ink tracks of consistent geometry. As illustrted in Fig 3.31, the tracks had width of 2.8 mm and thickness of 100 microns. Newly deposited ink track samples were left for 24 hours before laser curing trials.
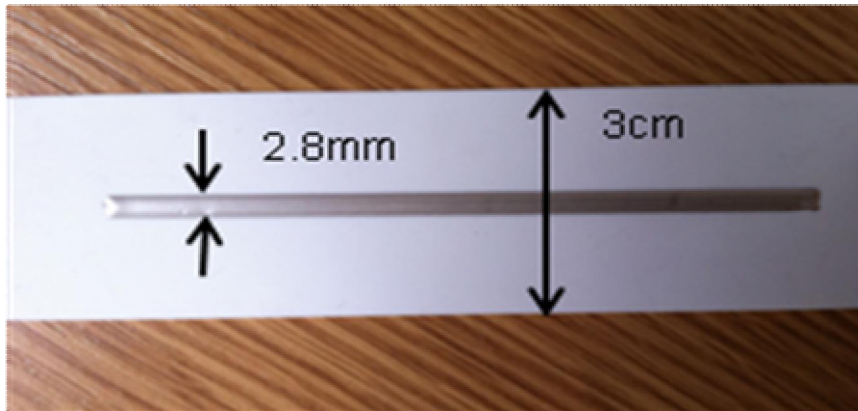
Fig 3.31. Example of an ink track deposited with the dispensing system.

3.4.2 The laser curing method

3.4.2.1 Defocused curing with the Synrad laser system
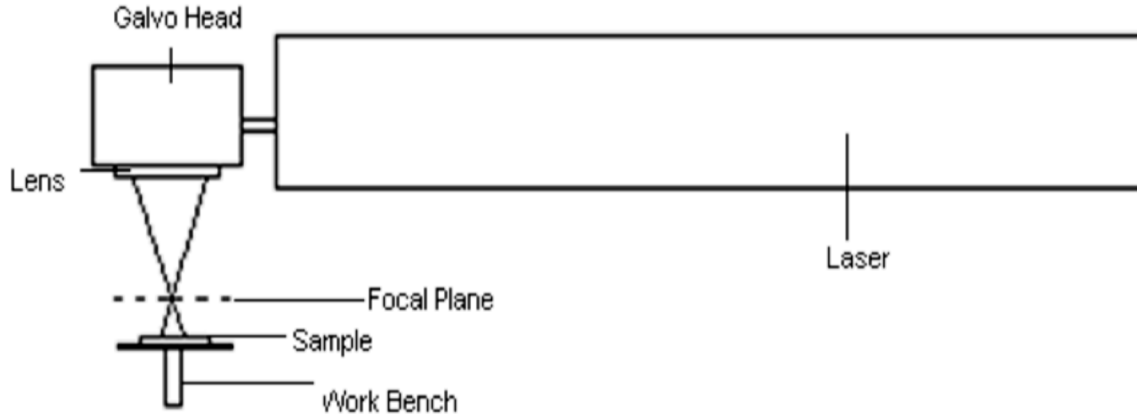
Fig 3.32. Schematic of the defocused operation of the Synrad laser, with respect to the work bench and sample.

The Synrad laser system outputs continuous beam of 10.6 m wavelength with a Gaussian mode. It has a focal length of 242 mm and a spot size of 150 m. However the focus was not used for these experiments. A focussed spot would have a too high energy density and would burn the polymer and with such a small spot size that multiple scans would have to be conducted to create a cured patch. By using a defocused spot size it was possible to match the width of the tracks deposited and modulate the power setting accordingly to achieve the right energy density. The appropriate energy density was found through experiments. Since the track sizes used were 2.8 mm in width and a thickness of 90 m, it was desirable that the spot size would match this. It was found that if the sample was placed 350 mm from the lens, the spot size would be approximately 2.8 mm. Using this width, the beam would irradiate the whole width of the track in one pass. Because a different position was being used, in this case further away from the lens (Figure 3.32) this meant that the input speeds would no longer correspond to the actual speed as seen by the sample. The speed would now be faster as the sample was further away from the focus. This meant that the actual speed as measured by the sample was 1.45 times the input velocity.

To minimise experimental error, the output power and beam mode were monitored regularly; a bespoke sample holder was also made to keep the substrates flat and in position through out a curing process; All sample substrates are cleaned with acetone before deposition.

3.4.2.2 Curing with shaped intensity profile using the SunShaper

LADW with shaped beam profiles were implemented on the Solsurf system with the SunShaper integrated. As shown in Fig 3.33, the minimum power of the Rofin SC30 Laser was further reduced by a beam attenuator to a power level that was suitable for curing. The Gaussian beam then goes into the SunShaper and transformed into a filled annular ring profile at its focus on the sample surface. The CNC stage then traversed along the axis and thus cured the track. The focused beam approximately positions right on top of the sample tracks width during the process.
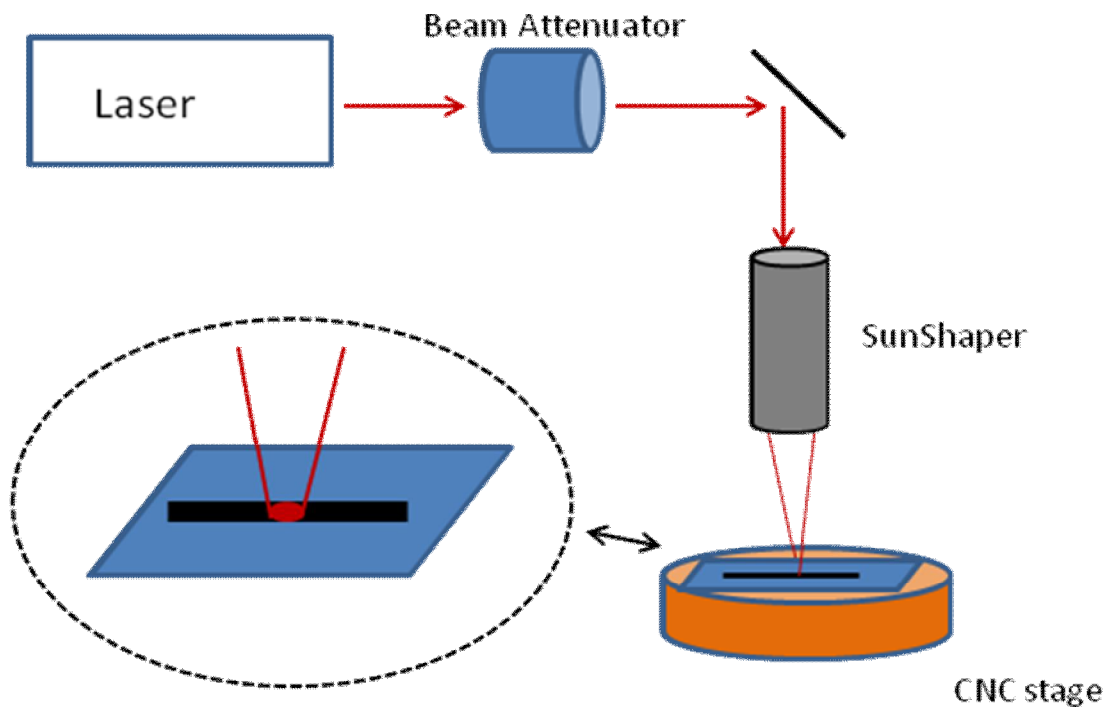
Fig 3.33. Schematic of LADW using focused shaped beam produced with the SunShaper.

The laser power and mode from the SunShaper were checked regularly with the LaserDec beam profiler each time before curing. A bespoke sample holder is also made for this set-up to eliminate misalignment and thus minimise error.

4. Results, Analysis and Discussion

This chapter compares simulation and experimental results and thus discusses verify the validity of the proposed model.

Firstly, the thermal evolution of ink tracks during a LADW process is studied by simulation. Then a parametric curing window is produced for a range of traverse speeds, laser intensity and substrate materials. This window is shown to be valid by comparison with experimental results.

Curing with different intensity profiles is then investigated. Experimental and model results agree in suggesting that an annular filled ring profile provides considerable improvement compared with a Gaussian beam.

In the final part of the study, model input parameters are modified to match the properties of D1 ink, after running STA analysis for the ink and each component. Experimental data is considered supports the model and proves its validity for different inks with different composition and thermal properties.

The methodology and results in this study are compared with similar work done by others previously, where appropriate.

4.1 Simulation of generic ink tracks on PET substrates with Gaussian beam

The model for a generic ink described in Chapter 2 was simulated and produces a set of results, which can be extracted, analysed and presented in various fashions within the Comsol 4.0 environment. Thus, one can obtain quantitative information of the thermal evolution during LADW which would be extremely difficult to obtain using experimental techniques.

4.1.1 Simulation results

Fig 4.1 (a-f) illustrates simulation results for samples on PET substrates at laser traverse speeds of 0.5mm/s,1mm/s,2mm/s,3mm/s,4mm/s and 5 mm/s respectively, with 8W laser power and a Gaussian mode of spot diameter of 2.6mm.

(a)

(b)

(c)

(d)

V= 4mm/s

V= 5mm/s

(e)

(f)
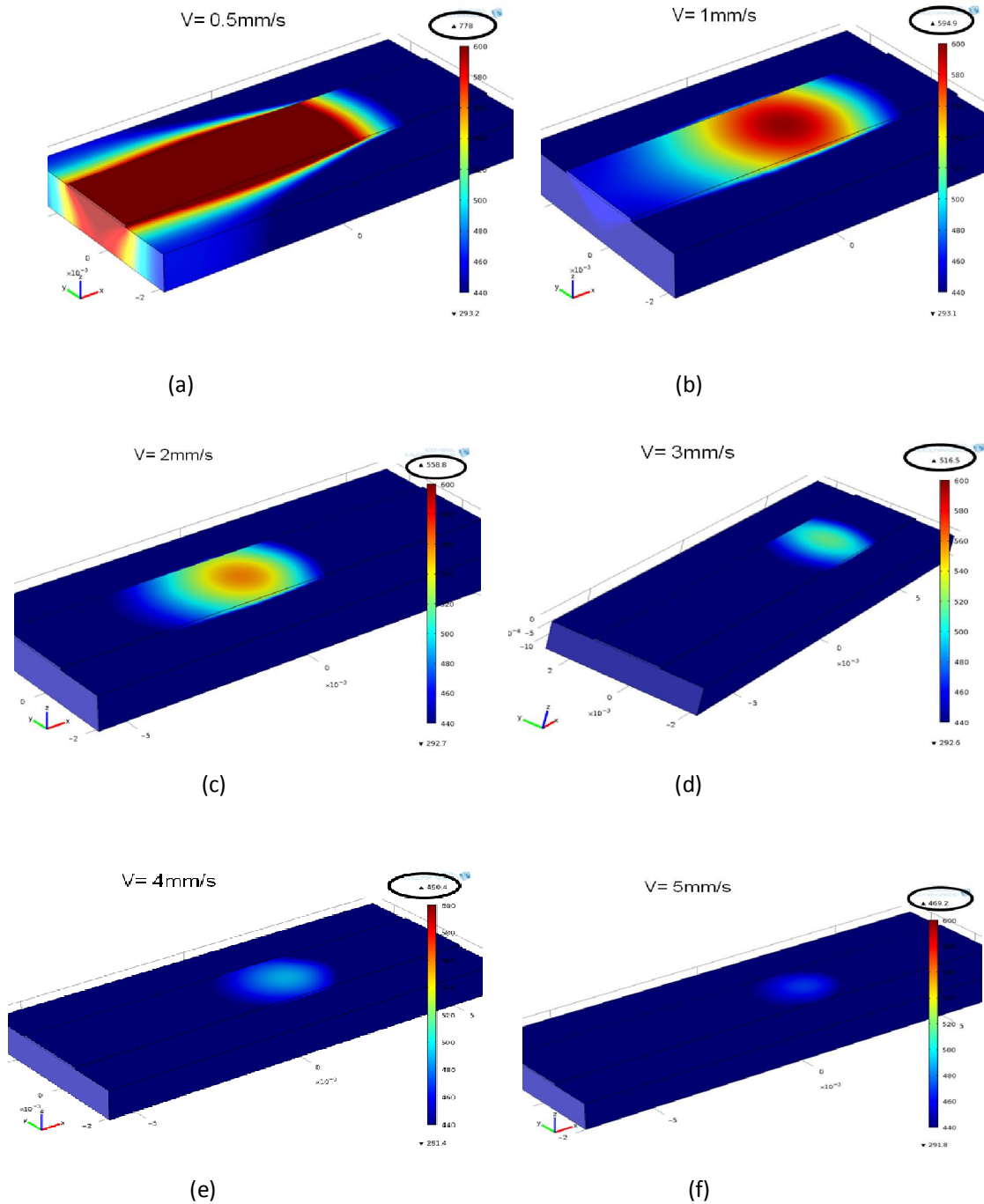
Fig 4.1 (a-f): Temperature distribution for traverse speed of 0.5mm/s, 1mm/s, 2mm/s, 3mm/s, 4mm/s and 5mm/s, with a Gaussian beam of 2.6mm diameter spot at 8W.

As one would expect, the peak temperature at the centre of the beam becomes smaller as the laser traverse speed increases. At the lowest traverse speed of 0.5mm/s (a), the entire ink track is heated far beyond the curing temperature, indicating the laser beam is moving too slowly for this power. For 1mm/s, the ink track is cured, as the track is well within the curing

temperature window. The highest temperature occurs at the centre of the track, with a value of 595 K, as marked on the temperature scale in (b). With further increase in the speed to 2mm/s (c) and 3mm/s(d), the ink can still be cured but the maximum temperature drops as less energy is coupled in per unit volume; For 5mm/s (f), most part of the track remains below the curing temperature after the laser passed and therefore clearly the ink track is not cured. In the case of 4mm/s (e), no immediate decision can be made and investigation of the cross-section is required, as shown in the Fig 4.2:
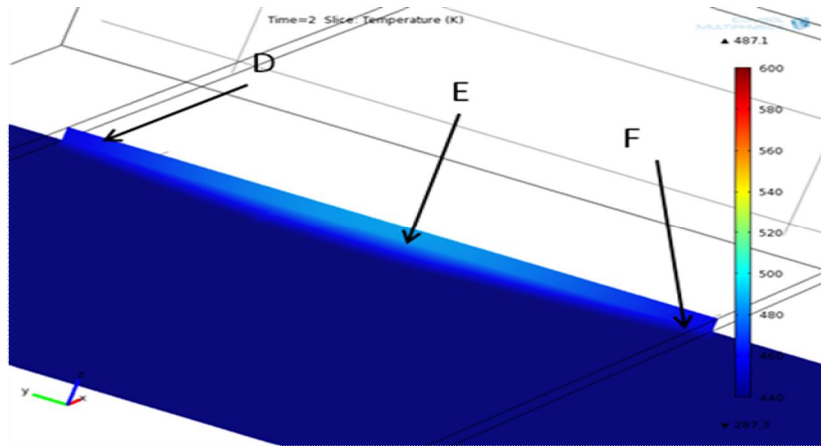
Fig 4.2: Sliced illustration of temperature at the bottom of the ink track for 4mm/s traverse speed, as of Fig 4.1(e).

Table 4.1: Coordinates and temperature of points D, E and F from Fig 4.2

	X/mm	Y/mm	Z/mm	Temp/K
D	1.5	1.3	-6.00×10^{-2}	460.75
E	1.5	0	-6.00×10^{-2}	486.19
F	1.5	-1.3	-6.00×10^{-2}	460.93

In Fig 4.2, D, E and F are three points at the bottom of the ink track, sliced at the hottest location along the X-axis. The co-ordinates and corresponding temperature are shown in

Table 1. The temperature at D and F is just above the curing temperature for this ink (refer to Chapter 2) and the result suggests that the ink is marginally cured at the edges. The tracks are 2.8mm wide and 60 micron thick, therefore D, E and F lie on the interface between ink and substrate, with E and F on the edge of the track.

Therefore the model concludes that, for this particular set of parameters, traversing at 4mm/s results in full curing of the ink at the fastest rates, but rates of 1mm/s-3mm/s are acceptable.

In the previous experimental work of Fearon and Sato [132], a similar situation had been studied: D58 ink was deposited on Printed Circuit Board (PCB) substrate with almost identical thermal conductivity (0.23W/mK) compared to PET (0.24W/mK). With all other processing parameters being identical, their experimental result suggested that full curing is achieved for a traverse speed between 1 and 3 mm/s, which is in full agreement with the simulation result obtained in this study.

4.1.2 Linear temporal analysis

In order to study the temperature evolution of samples during the entire curing process, linear temporal analysis was carried out. Data along two specific lines were extracted which represent temperature at the centre and the edge regions of the track, as shown in Fig 4.3. The case for v=3mm/s, and the length of the lines are 12 mm was studied. The positions of l_1 and l_2 are l_1 (Y=0, Z=0.06) and l_2=(Y=-1.3,Z=0.06) respectively.
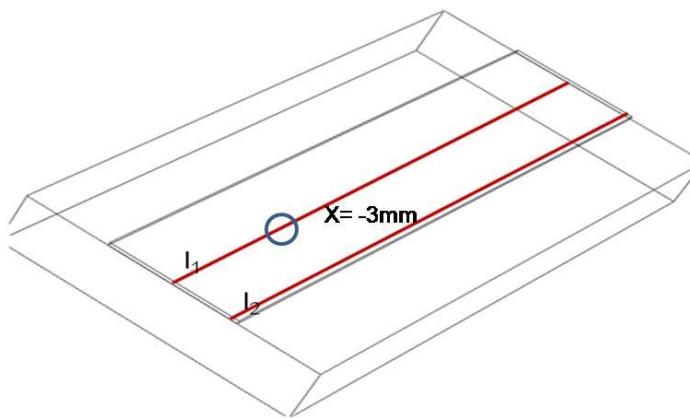
Fig 4.3: Positions of l_1 and l_2, and x= -3 mm, representing the centre and the edge regions of the ink track.

Transient Temperature Profile (x=-3)
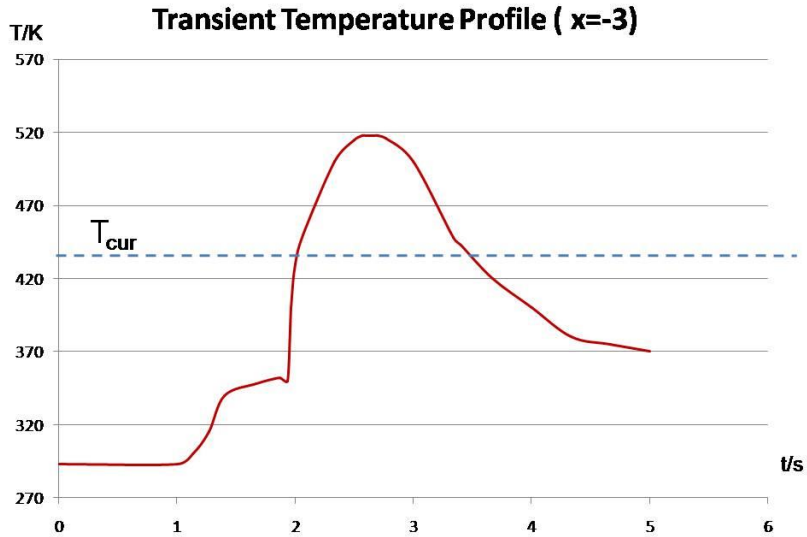
Fig 4.4: Temperature evolution at x=-3, as laser passes.

Temperature evolution along l_1 and l_2 at 4s
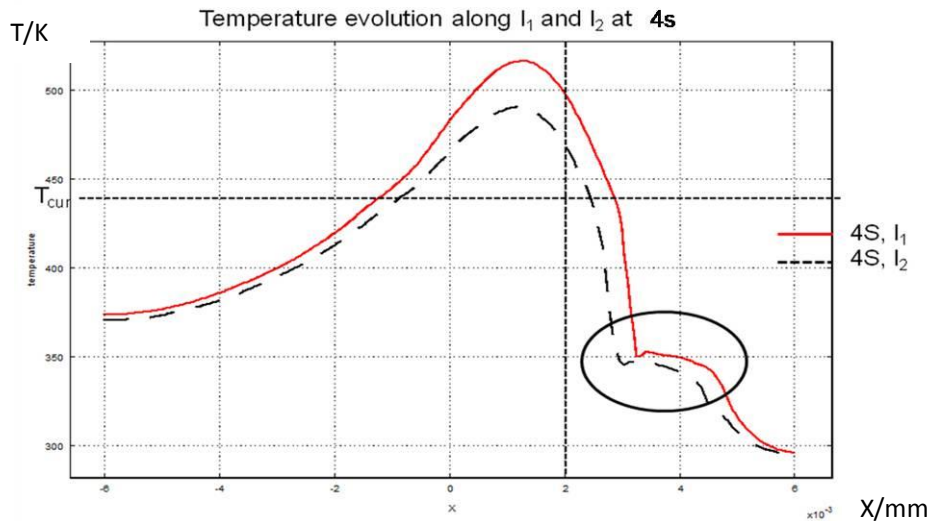
Fig 4.5: Temperature distribution along l_1 after 4 seconds.

Two types of linear analysis are illustrated:

1) The temperature evolution at one point over time during the curing process (Fig 4.4).

2) Temperature distribution along both lines at a particular time (Fig 4.5)

In Fig 4.4, temperature evolution at (x=-3, y=0) is plotted against time. It can be seen that the peak temperature is well above the curing temperature (433 K), suggesting that the centre of the track will be cured, following the moving beam. The point stays at room temperature

just after 1 s when the laser spot arrives. The temperature elevates to ~350 $^{\circ}$C (~1.3 s) and then the rate of temperature rise decreases due to the latent heat of the solvent, as programmed into the model; after the solvent is fully vaporised (~2 s), the temperature rises sharply again until the laser spot completely passes by (~ 2.77 s), and then the temperature drops gradually. This reflects the mechanism described in Chapter 2, as intended.

Now the temperatures of l_1 and l_2 after 4s were compared. By plotting temperature along each line for a series of points in time, it can be confirmed whether the ink is evenly cured across its full width. As a direct result of the Gaussian laser beam profile, the temperature at the track edge is always lower than that at the centre, as shown in Fig 4.5. Nevertheless, the edges are still cured, since the peak of the dashed curve is above T_{cur}. After 4s, the centre of the laser spot is at X=2mm (as marked with the vertical dashed line), while the peaks of the temperature curve lag behind at X~1mm. This is because temperature reflects the accumulated heat inflow and will therefore only occur at a point where the total beam centre has passed by. This phenomenon has also been noted by Wellburn [18]. The laser moves in the X+ direction, as a result, the curves are skewed to the left.

The circled region in Fig 4.5 displays the nonlinearity of the specific heat capacity of the ink, arose from its components. As previously mentioned in Chapter 2, once ink approaches T_v (353K), further heating will be used to evaporate the solvent, and upon complete evaporation, the ink temperature will again elevate at a sharper gradient.
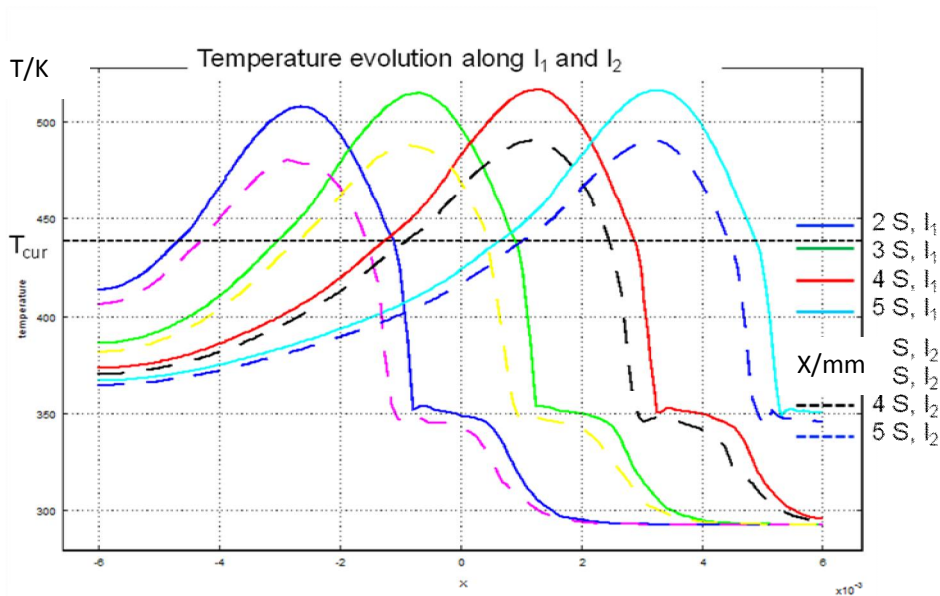
Fig 4.6: Temperature distribution along l_1 and l_2.

By combining the information presented in (Fig 4.4) and (Fig 4.5), the complete evolution of temperature curves for both the centre (l_1) and the edges (l_2) of the track are plotted in Fig 4.6. It is clear that both regions are cured as time passes. This means that in this model, once a set of parameters is found able to cure ink locally, its ability to cure with translational movement is also confirmed.

In the field of printable electronics, the vast majority of the inks used consist of a conductive powder agent (usually silver, gold or copper, for their non-oxidising properties), a polymer that cross-links upon heating, and a solvent for carrier viscosity reduction: Jung et al studied the process with an ink that consists of Ag nanoparticles, oleylamine, methanol and toluene [145]; Jo et al synthesised Sn-xAg particles dispersed in methanol to make conductive inks [149]; In other words, the thermal properties displayed by the generic ink modelled above represents the characteristics of typical conductive printable inks for this application [144, 146-148, 150-152].

4.2 Curing of D58 ink tracks on various substrates

The ink employed is less than 200 microns thick in most LADW applications. For such thin films, the minimum energy required to cure the ink is approximately proportional to its thickness. Normalised Intensity of Laser , I_n , can be defined as

$$I_n = \frac{I_{av}}{h} = (\frac{1}{h}) \frac{1}{\pi R^2} \oiint I \, dR \tag{4.1}$$

where h is the thickness of the ink and R is the half track width. I_n represents the average laser intensity per micron and thus one can compare curing processes carried out with ink tracks of different thicknesses as predicted by the model.

4.2.1 Parametric curing map

The LADW process now involves three free parameters: substrate thermal conductivity (k), normalised laser intensity profile (I_n) and traverse speed (v). The relationship between these parameters is shown in Fig 4.7 as a 3D surface graph plotted in MATLAB environment. The X-axis is k on a logarithmic scale, Y-axis is I_n and Z-axis is v on a logarithmic scale.

Applying the definitions of cured, undercured and overcured from Chapter 2, a surface is constructed with a matrix of data points generated by the model, each representing the maximum traverse speed one can use without undercuring the ink track for a particular substrate thermal conductivity k and normalised laser intensity I_n. The model therefore predicts that any combination of parameters that is represented by a point above this undercuring surface will not be able to successfully cure the ink track. In other words, the parametric under curing surface generated with the generic ink can now be used to predict processes done with the actual D58 ink.
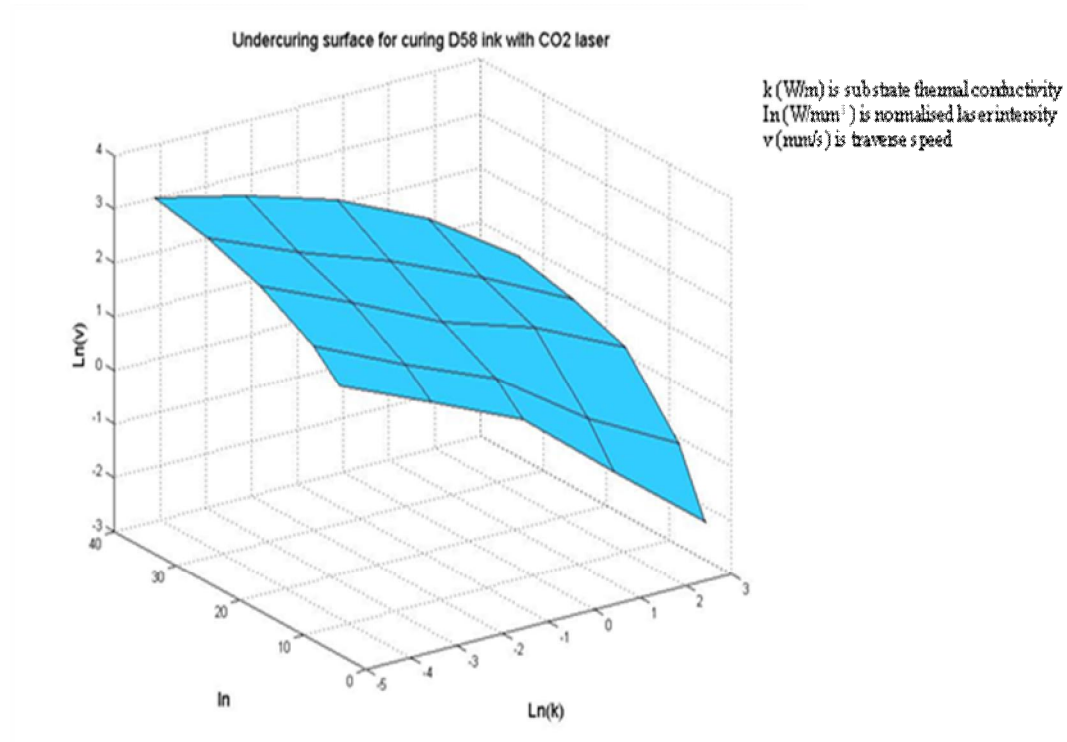
Fig 4.7. The undercuring surface for D58 ink with a CO_2 Laser.

The undercuring surface provides information that not only confirms previously gained experimental knowledge, but also offers quantitative understanding. As shown in Fig 4.7, for any fixed laser intensity profile, traverse speed has to be reduced if the ink is deposited onto a more thermally conductive substrate [132]; Also, for any particular substrate, higher normalised intensity would enable a faster curing process speed.

The projected surface contour in the X-Y Plane is shown in Fig 4.8. For any point on the plane, there is a curve passing through it exclusively. The number associated with the curve

corresponds to the highest traverse speed (logarithmic scale) that one can use to cure, for the conditions indicated by the point's coordinates. The directions of lines indicate that higher laser intensity is required for more a thermally conductive substrate to maintain the same processing efficiency.

In
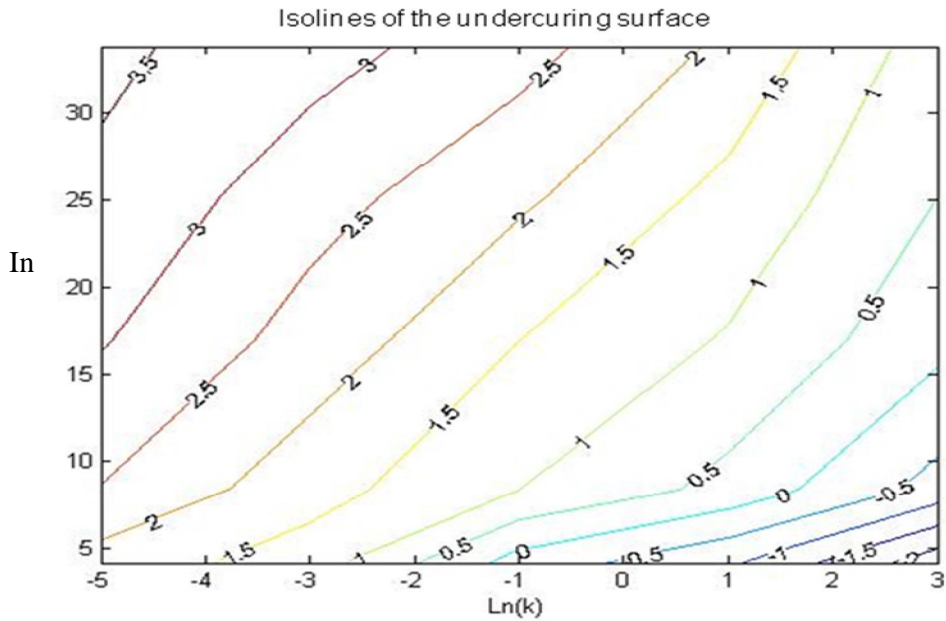
Fig 4.8. Contour projection (isolines) of the undercuring surfaces for D58 ink with a CO_2 Laser.

Parametric processing window for curing D58 ink with CO2 laser

k (W/m) is substrate thermal conductivity
In (W/mm²) is normalised laser intensity
v (mm/s) is traverse speed

In   Ln(k)
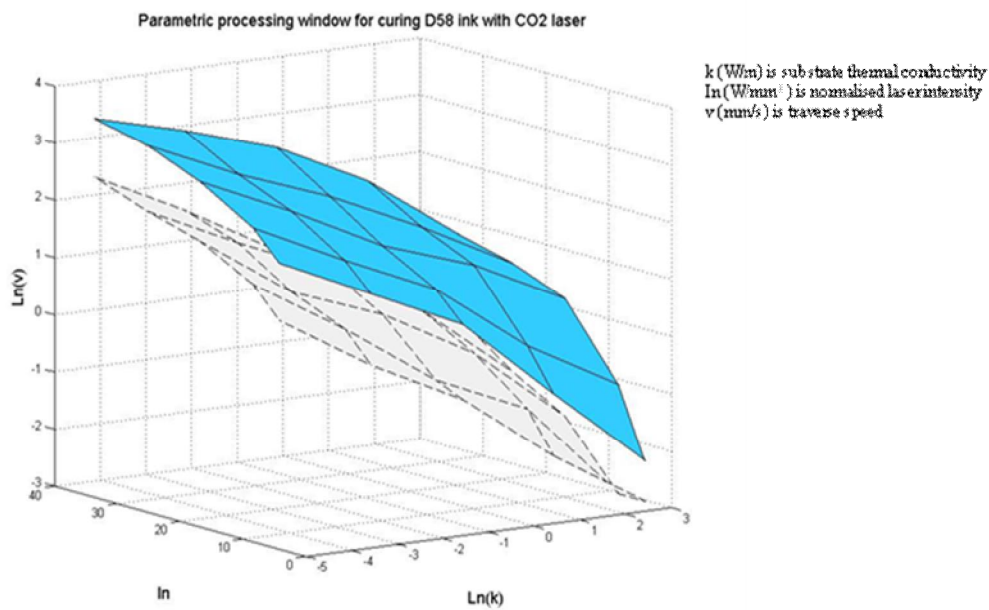
Fig 4.9. Processing window defined by the undercuring and overcuring surfaces for D58 ink with a CO_2 Laser.

In Fig 4.9 an overcuring surface (bounded with dashed edges) is constructed based on the same method. Points below this surface correspond to parameters at which one risks overcuring the ink track. The generic processing window is then defined by the set of parameter combinations which bounds the cured data from the uncured.

The overcuring surface lies below the undercuring surface without intersection and thus provides a processing window. This window suggests that to achieve optimised curing results one should aim to use parameters that lie between these two surfaces. Points close to the top surface would yield a higher throughput; while points close to the lower surface generally result in tracks with better electrical conductivity. In practice, engineers are often limited by the choice of materials and equipment available for curing; numerous experimental trials have to be conducted if one or more parameters require changing. With the aid of this method, ranges of parameters for investigation can be more accurately predicted.

Table 4.2 presents results of curing trials for D58 ink on PET substrates with varying laser power and traverse speed. Table 4.3 shows results obtained by Fearon et al [132], in which case the laser power is kept constant and different substrates are used.

Table 4.2: Curing results obtained for D58 ink on PET substrates, with varying CO_2 laser power and fixed beam radius of 1.1 mm. Bold italic font represents fully cured samples; undercured and overcured samples are represented by dashed and solid underscored numbers respectively.

Substrate	Laser Power (W)	Traverse Speed (mm/s)					
PET	3	***0.5***	***1***	2	3	5	8
	5	0.5	***1***	***2***	3	5	8
	7	0.5	1	2	***3***	5	8
	9	0.5	1	2	3	***5***	8

Table 4.3: Curing results obtained by Fearon et al for D58 ink, with fixed CO_2 laser power of 8W, beam radius of 1.1mm, and different substrates. Bold italic font represents fully cured samples; undercured and overcured samples are represented by dashed and solid underscored numbers

Substrate	Thermal Conductivity (W/mK)	Traverse Speed (mm/s)				
Alumina	18	*0.12*	*0.25*	0.5	0.75	1.00
CFC	0.059	*1*	*2*	*4*	6	8
PET	0.23	*1*	*2*	*3*	4	5
Polyaramid	0.04	*2*	*4*	*6*	8	10
Burn Paper	0.01	*10*	*12*	*14*	16	18

(a)
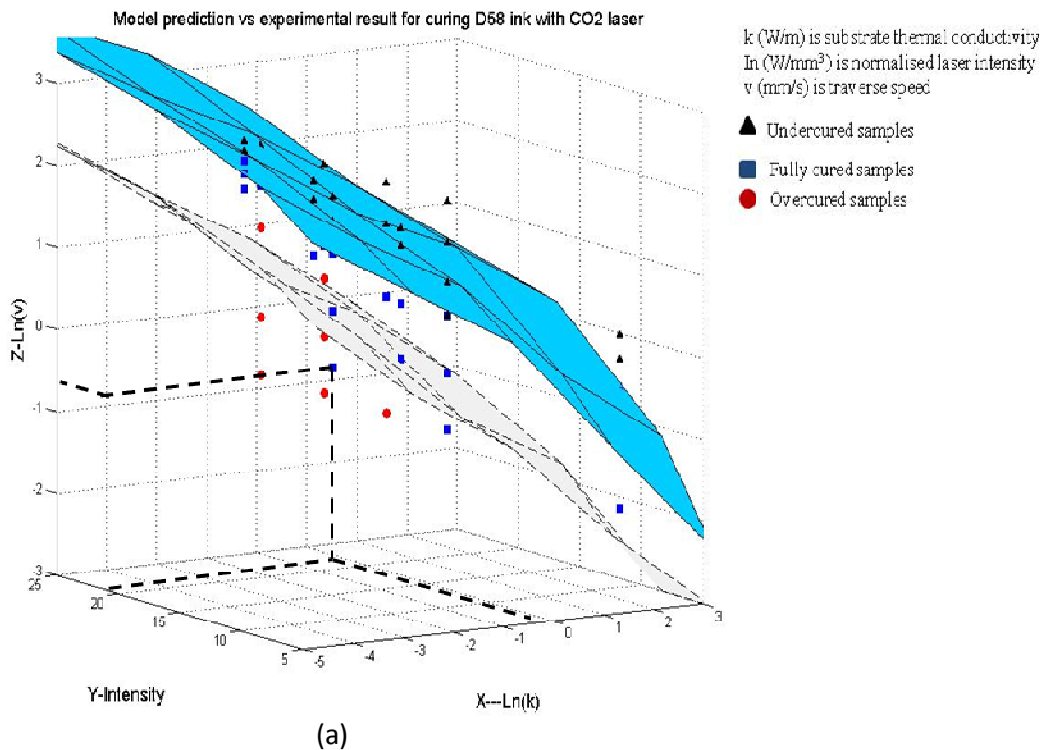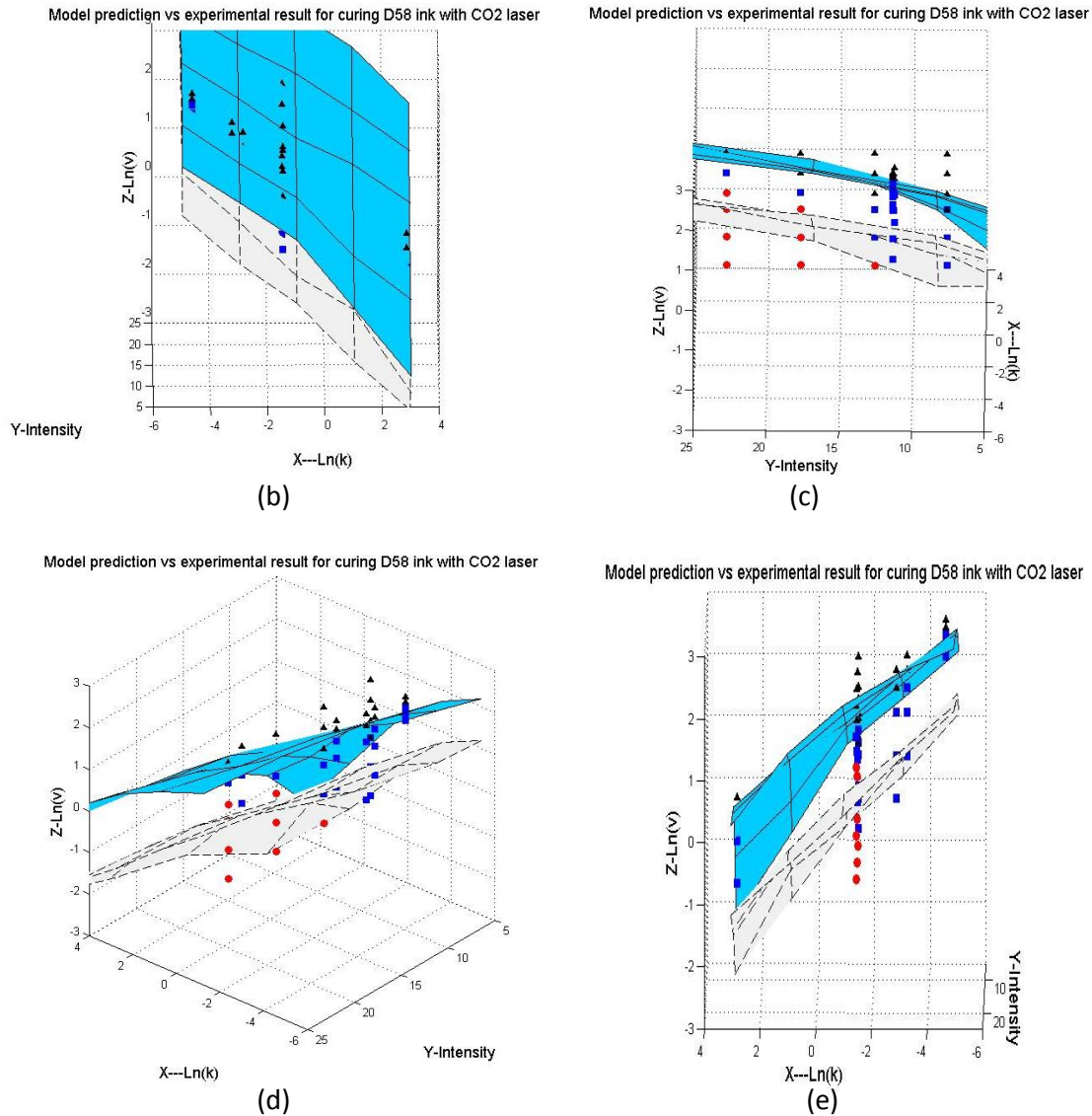
Fig 4.10 (a-e) Comparison between model prediction and experimental results for D58 ink with a CO_2 Laser. The X, Y and Z axis are for Ln(k), Normalised Intensity I_n, and Ln(v) respectively, where k is thermal conductivity of substrate and v is laser traverse speed. Dotted line in (a) marks the coordinate of a data point on the 3D map. The blue and grey surfaces are simulated undercuring and overcuring surfaces respectively; the data points are experimental parameters used.

The results from Table 1 and Table 2 are fitted on the processing window as scattered points (Fig 4.10 a-e). As illustrated in (a), the position of each point can be estimated with the intersections of extension lines and each axis. Squares represent cured samples; triangles represent undercured samples; and points are overcured samples. Most of the squares lie between the two surfaces, with points below the overcuring surface and the triangles above

the undercuring surface. This means that the model prediction and experimental results are in good agreement. There are small discrepancies in some particular cases. Fig 4.10 (b-e) shows the same map from different angles of view, to illustrates the positions of data points. The model uses a generic ink, which consists of silver micro particles, epoxy resin and ethanol. The actual ink used in the experiment had constituents with close thermal properties and mixing proportion to that used in the model, but not identical. The model could be further improved by the use of a series of genuine ink parameters.

Agreement between the model and experiments has been achieved for a wide range of laser intensity and substrate thermal conductivity, indicating good accuracy and wide applicability of the model. It is important to be aware that this map has freedom over the processing parameters, but is generated for a particular kind of ink. For an ink with very different thermal properties, one needs to regenerate the map by running the model. This however could involve significant computation time. Engineers will be able to cure any particular kind of ink very efficiently once facilitated with such a processing window as a guide.

Simone has used a similar approach to investigate the sintering of polymeric powder on metallic substrates [9]. In her study, õthe influence of the output power from the source, the focal length, and the scan speed have been investigated. The extreme limits of the parameters have been defined through a preliminary study to furnish the conditions that yield either an uncured or degraded coating.ö In other words, she studied the effect on curing caused by the Laser intensity and traverse speed, as in this work. She also defined a curing window qualitatively: õOn the basis of the experimental findings, an empirical model has been proposed and a map of the process has been built up. The 3D map constitutes a practical tool for technicians in industrial applications, and for scientists, it contributes to an understanding of the influence of the various parameters on the process.ö

It is worth noting that in Simoneøs work, epoxy-polyester hybrid resin was supplied in the form of coarse divided powder; the substrate used was stainless-steel sheets with dimensions of 50mm, 100mm, and 5mm; the laser used had 940 nm wavelength. Regardless of the drastic differences in material properties between her study and this work, both investigations confirm the relationship between traverse speed and laser power for a particular curing quality required. This work also accounted for the effect of substrate thermal conductivity, which is not studied by Simone.

A 3D curing map is produced in Simoneøs work (Fig 4.11).
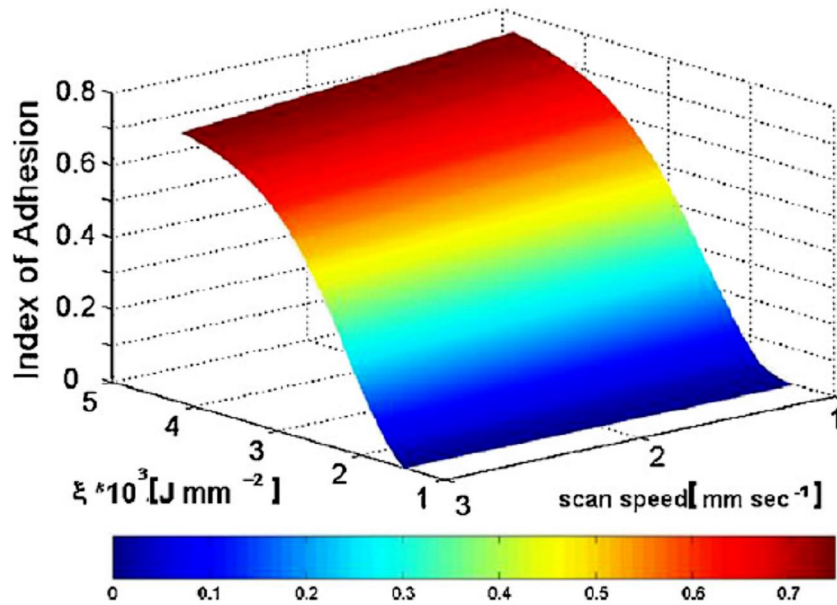
Fig 4.11. 3D Processing Map for Epoxy-polyester hybrid resin on Stainless steel substrate[9].

Similar to Fig 4.10, this map is only for a particular ink type. The difference between the two maps are that, Fig 4.10 is a true 3D map with 3 variables: Laser intensity, traverse speed and substrate thermal conductivity, whereas Fig 4.11 only has two variables with the substrate kept unchanged; The vertical axis in Fig 4.11 represents the õIndex of Adhesionö that marks the scratch resistance of the cured track. This property is illustrated in Fig 4.10 with different curing quality classes, which is more direct for engineers to work with.

Regardless to the differences, one can see the clear trend of reducing cure quality (Adhesion) with higher scan speed and lower laser power in Fig 4.11. This shows agreement with the map in Fig 4.10, as one may intuitively predict.

4.3 Curing D58 ink tracks with shaped beam profiles

This section presents the beam profiles obtained with the SunShaper; the simulation output obtained with such intensity distributions; and the experimental results of LADW with shaped beam modes.

4.3.1 Shaped beams obtained with the SunShaper

Fig 4.12 and Fig 4.13 present the results of beam shaping with the SunShaper, captured with the LaserDec beam profiler. The RayCi software allows visualisation of 2D intensity distributions (Fig 4.12). Data can also be exported to other softwares for quantified cross-sectional analysis, shown in Fig 4.13. The laser power is 13W in all three cases, in order to make direct comparison of the shaped beam profiles.

(a)   (b)   (c)
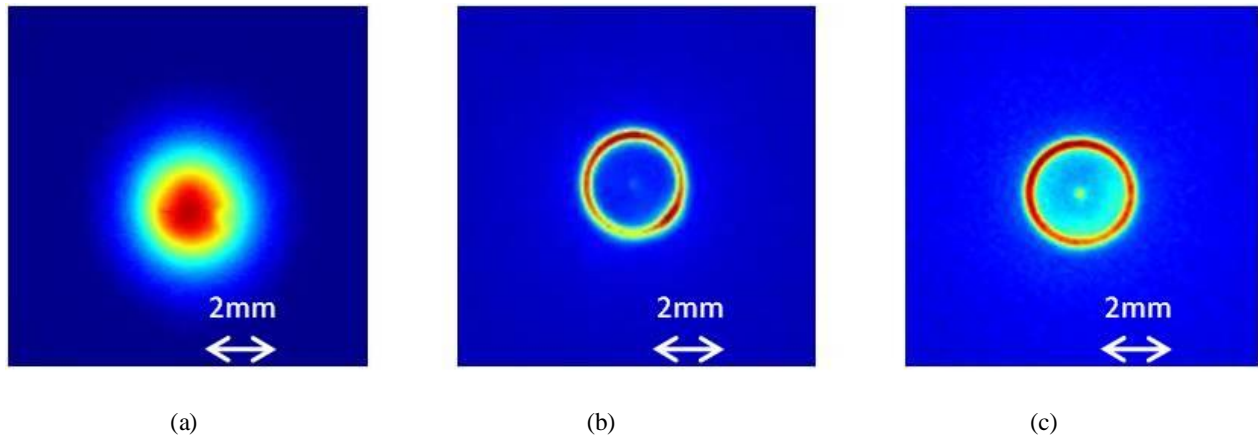
Fig 4.12. 2D intensity distribution of: a) Gaussian beam b) 15% plateau filled annular ring c) 35% filled annular ring

Fig 4.12 a) shows a Gaussian beam focused to a spot with beam diameter of 2.6 mm. b-c) show that of a 15% and 35% plateau filled annular rings: the intensity is evenly distributed in the ring, and the fill levels of the plateaus are approximately 15% and 35% of the ring intensity respectively.

Instead of 25% and 50%, the actual fill levels achieved are 15% and 35%. This is because the attenuator has reduced the size of the input beam from 9 mm diameter to ~8 mm, while the SunShaper is designed for a collimated beam with 9mm diameter.

Comparing the two shaped beams, the fill level is noticeably higher in (c), this appears both as a brighter central region in Fig 12.c) and a higher fill level in Fig 13.c). There is a small peak at the centre of the plateau in the case of 35% filled ring. This is due to a diffraction effect caused by the discontinuity on the surfaces of the optics in the SunShaper unit. This diffraction effect had been discounted in the design of the unit used; it will be eliminated in later modified versions of the SunShapers. However such small peak has negligible effect on any heat conduction dominated processing. Overall the SunShaper produces satisfactory shaped beam profiles

(a)   (b)   (c)
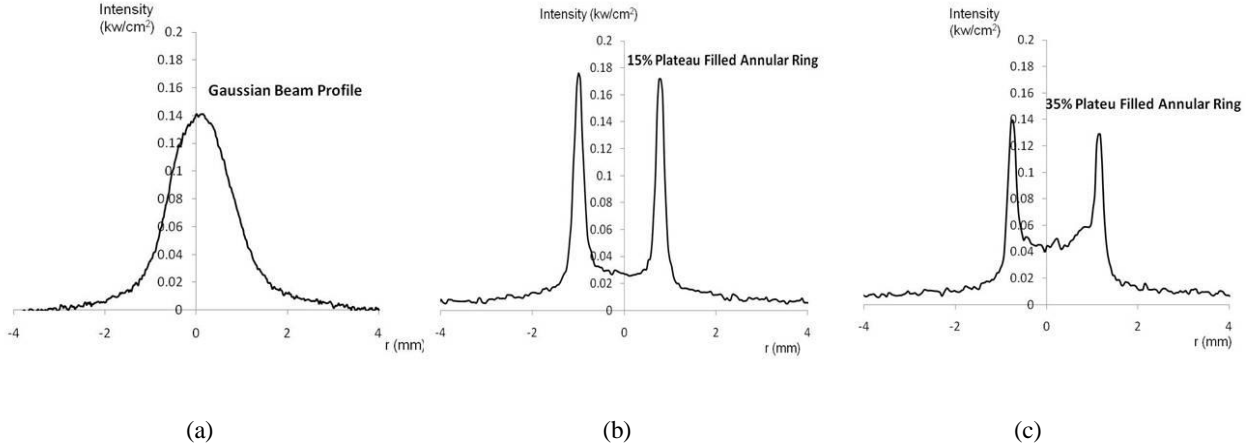
Fig 4.13 Cross-sectional intensity analysis of: a) Gaussian beam b) 15% plateau filled annular ring c) 35% filled annular ring.

4.3.2 The Peclet Number and its relevance to this work

In Wellburnøs work, he showed that in the case of surface heat treatment of sheet metal, assuming that , C_p and k are constant during the process, then the optimised uniformity achieved at any depth, corresponds to a particular Peclet number for any given beam profile. Certain beam profiles are able to achieve much better uniformity compared to other [18].

In order to explore the relevance of Peclet number in this study, the following argument is extended:

The dimensionless traverse speed can be represented by the Peclet number Pe, where

$$v^* = Pe = \frac{vR_0}{\alpha} \tag{4.2}$$

Where   is the diffusivity of material, and

$$\alpha = \frac{k}{\rho C_P} \tag{4.3}$$

With k being the thermal conductivity.

 , C_p and k are all non-linear functions of temperature, whose values changes dramatically around the curing temperature with D58 ink as a clear example (Fig 2.7 and Fig 2.8)

And therefore, referring to Fig 2.7-2.9 from Chapter 2

$$Pe = \frac{vR_0}{\alpha} = vR_0 \left(\frac{\rho_{(T)} C_{P(T)}}{k_{(T)}} \right) \tag{4.4}$$

where k, C_p and are all nonlinear functions of temerature T.

Equation (4.4) shows that, for any particular ink, and a constant beam radius R_0, the Peclet number is a function of temperature T and traverse speed v, with linear partial dependence on v and non-linear partial dependence on T.

Therefore a 3D surface can be constructed to demonstrate the Peclet number as a two variable function. In the case of D58 ink, the Peclet number surface is displayed in Fig 4.14

The traverse speed V is plotted on a logarithmic scale (0.05mm-12mm) as suggested by the curing surfaces (Fig 4.10), The temperature scale ranges from room temperature (293K) to the over-curing temperature (603K). Clearly, the Peclet number is a highly nonlinear functional surface. The high peak at T~355K is due to the spike in specific heat capacity in the ink; the lower peak at T~433K is a result of the cross-linking of polymer.
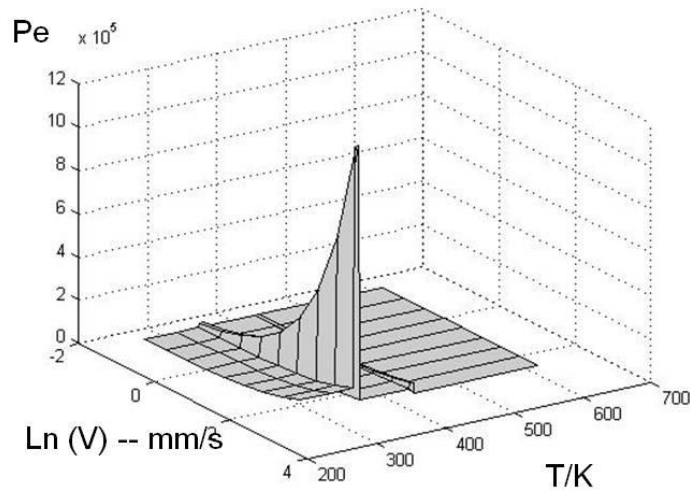
Fig 4.14   3D Peclet number surface

When a laser beam traverses along an ink track, different locations (marked with spots in Fig 4.15) on the track will have different temperature over time during the curing process. In other words, for any point on the ink track, its local Peclet number will vary over the surface shown in Fig 4.14 while being cured, and this variation is not fixed. Therefore it is inappropriate to analyse the uniformity of curing as a function of Peclet number, unlike in Wellburn's analysis [18].
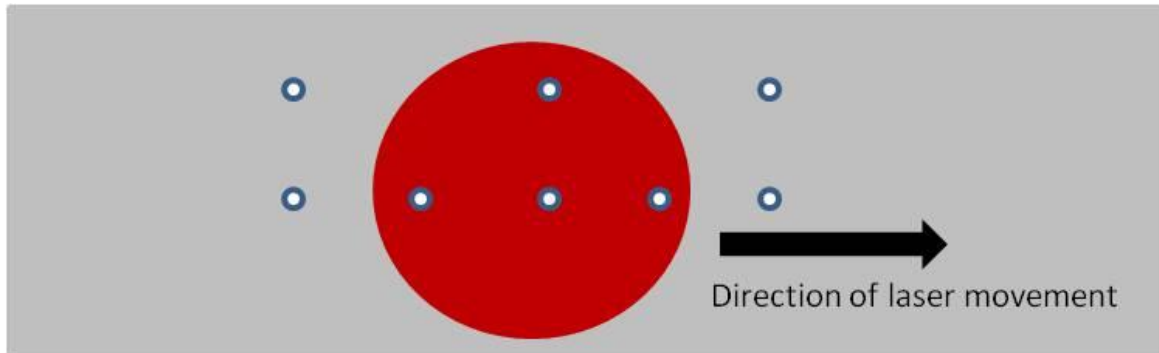
Fig 4.15   Evolution of local Peclet numbers during curing.

4.3.3 Temperature disparity

Uniformity study

In order to model which beam profile would provide better curing uniformity, simulations have been carried out using the generic ink parameters, for Gaussian, Top-hat, 15% filled annular ring and 35% filled ring intensity modes.
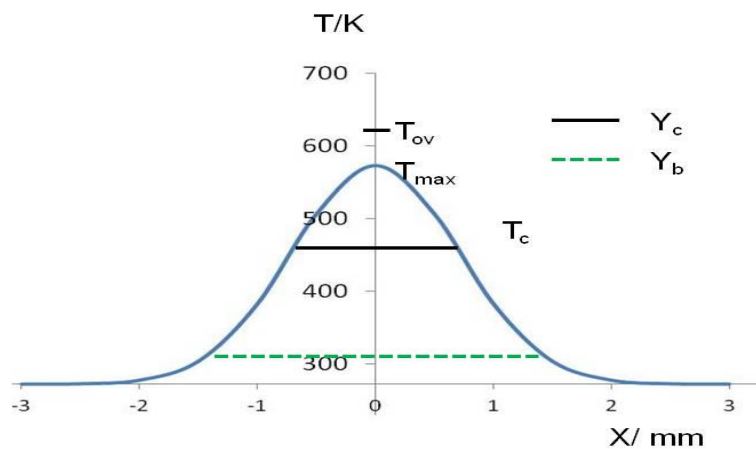
Fig 4.16 Measurement of temperature along the interface of a sample cross-section.

In Wellburnøs study [18], the measurement of uniformity was defined for metal surface heat treatment; a similar but different concept is defined here for curing of ink tracks.

Provided the ink track is not overcured, ie, the maximum temperature reached T_{max} is lower than the over curing temperature T_{ov}, the measure of curing uniformity is taken as

$$U = \frac{Y_c}{Y_b}$$

(4.5)

where Y_c is the width of the distribution which is above the curing temperature T_c, and Y_b is the width of the ink track, as shown in Fig 4.16 . For the purpose of this investigation, uniformity of 1 is ideal, for it represents the entire track cross-section is cured.

Beam profiles are compared at various simulated traverse speeds using this uniformity measurement, as shown in Fig 4.17. At low traverse speeds, all three beam profiles are able to cure the track; as speed increases, the performance starts to differentiate: uniformity produced by the Gaussian beam drops quickly, while the 35% filled ring profile shows superior uniformity over Top-hat and Guassian profiles. However, for traverse speeds of 1.2mm/s or higher, the 35% ring profile shows no advantage over the top-hat profile.
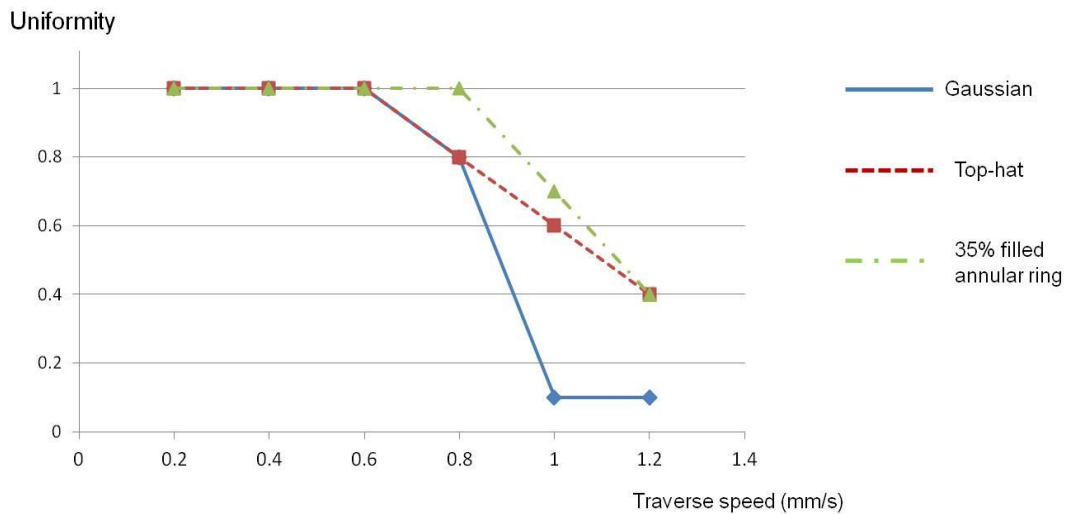
Fig 4.17   Simulation results of curing uniformity of 3 beam profiles as a function of traverse speed

The nonlinearity of temperature differential between the centre and the edge of an ink track, can also be compared for these profiles.

Temperature disparity for different beam profiles over a range of traverse speed
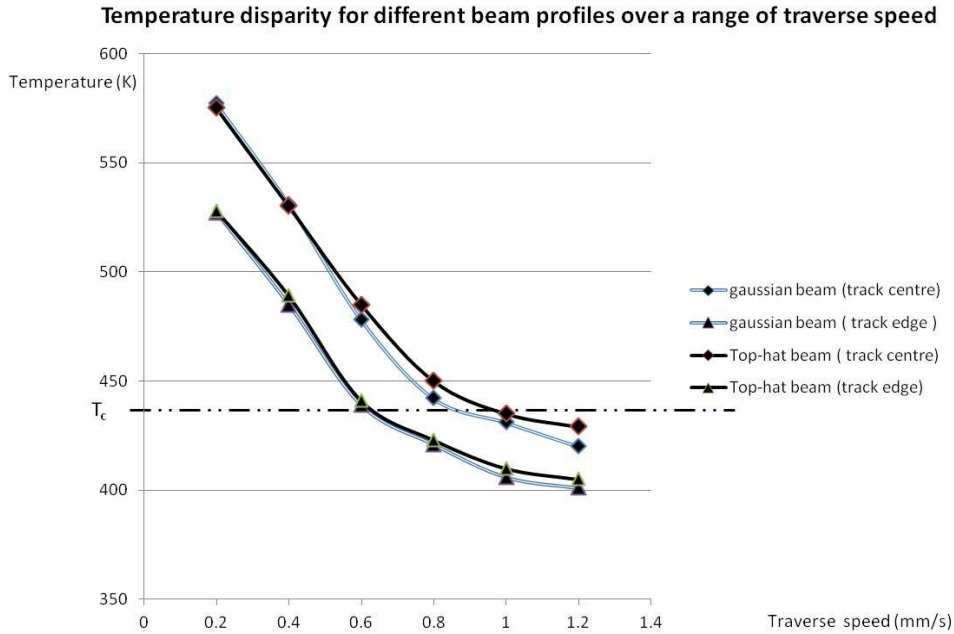
Fig 4.18. Temperature disparity during the curing process for Gaussian and Top-hat intensity distributions, over a range of curing traverse speed.

Fig 4.18 shows the simulated result of temperature disparity during the curing process for the Gaussian and Top-hat beam profiles, which is represented by the difference in the highest temperature experienced between the centre and the edge. The curing temperature T_C is also marked in the plot. For traverse speed less than 0.6mm/s, both beam profiles tested are capable of fully curing the ink track, and hence in this range the track behaves as a conductive material with linear thermal properties. The Top-hat beam profile produces almost identical disparity compared to the Gaussian beam. This is due to fact that the circular shape of the Top-hat beam will always heat the centre of a track more than the edges, as a Gaussian profile does. For higher speeds (> 0.6mm/s), the ink track becomes only partially cured or undercured [15], and the graph shows non-linear features in this region. Homogenised intensity allows more energy to be absorbed by the ink before being conducted away by the alumina substrate. Therefore, a Top-hat profile can achieve slightly higher temperature across the track, and hence slightly better curing than the Gaussian beam.

Temperature disparity for different beam profiles over a range of traverse speed
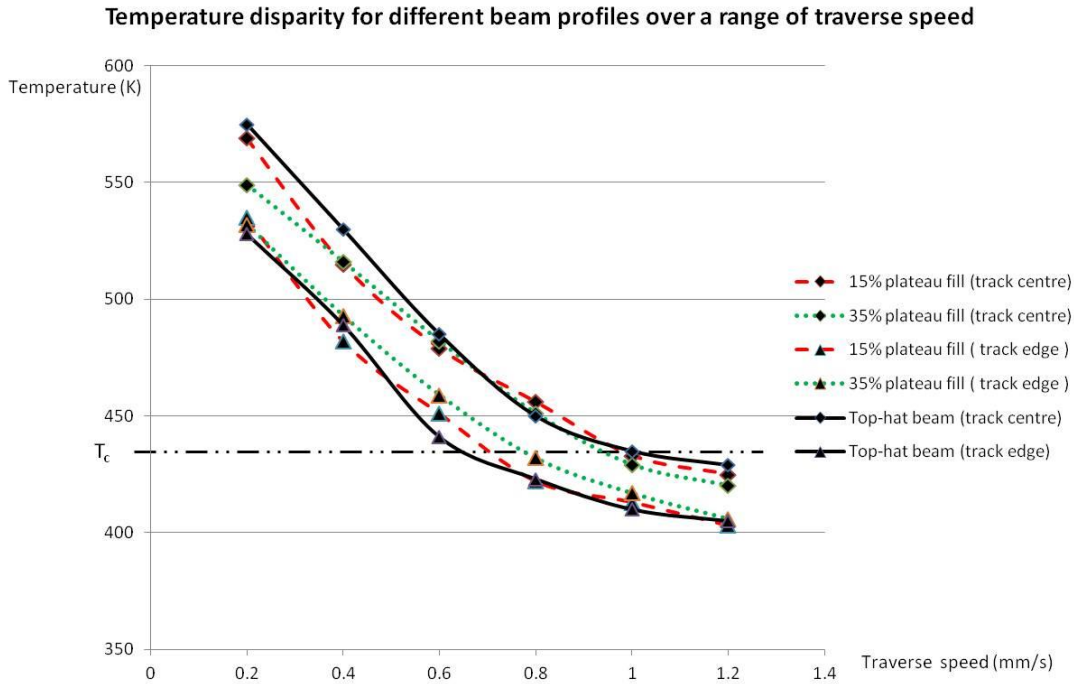
Fig 4.19. Temperature disparity during the curing process for Top-hat, 15% plateau filled annular ring and 35% plateau filled annular ring intensity distributions, over a range of curing

As shown in Fig 4.19, the graph can also be divided into a linear region (<0.6mm/s) and a non-linear region (>0.6mm/s). The plateau-filled ring profiles both show significant improvement over the Top-hat profile, in terms of less disparity.The 35% plateau filled ring has the smallest disparity, indicating its superior curing uniformity. The 35% filled ring profile also outperforms the 15% filled ring and Gaussian beam in terms of less temperature drop over a given increase in laser traverse speed. The model predicts that at 0.8mm/s, the 35% filled ring can still cure a track while the Gaussian beam would result in undercuring, and the 15% filled ring would only partially cure. Hence the model favours the 35% filled ring profile over 15% filled ring, Top-hat and Gaussian, for its better uniformity and larger curing speed range.

Low temperature disparity is extremely important for achieving a uniform curing.

Lewis described a model of Thermal Frontal Polymerization (TFP) in the study [21], which exhibits a localized reaction zone of higher temperature that propagates through the diffusion of heat into adjacent areas.

In this type of polymerization, a heat source or light is applied to a localized area, as shown in Fig 4.20. As the polymerization process occurs in this localized area, the heat produced from the exothermic polymerization reaction diffuses into the adjacent region, and this results in an autocatalytic polymerization, which propagates down the reaction vessel as a thermal wave.
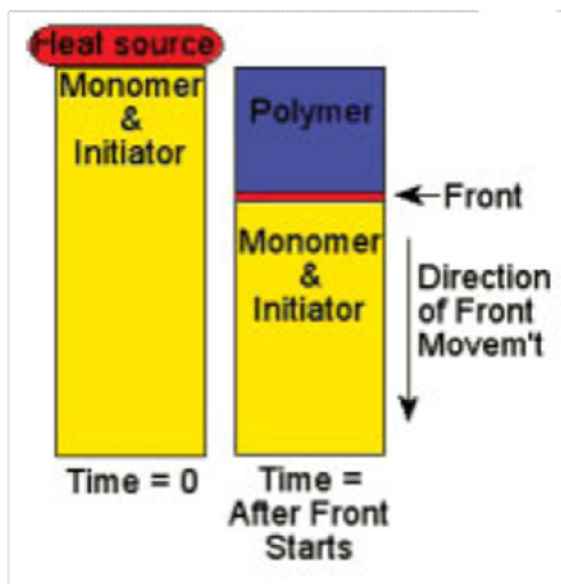
Fig 4.20. Illustration of the Thermal Frontal Polymerization mechanism [21]

Therefore if the laser produces non-uniform heating (ie, large temperature differential), a non-uniform thermal front will be generated across the ink track and is likely to give uneven curing.

4.3.4 Resistivity and hardness test results

Table 4.4 shows the result of the Wolff-Wilborn test (Chapter 3.2.7) for Gaussian, 15% filled ring and 35% filled ring intensities over a range of traverse speeds. The result suggests that, at every traverse speed, the 35% filled annular ring results in much better track hardness and adhesion to the substrate. 15% filled intensity profiles also give significant improvement compared to the commonly used Gaussian beam.

Table 4.4: Results of pencil hardness test for ink tracks cured with different beam profiles at different traverse speeds.

Laser curing traverse Speed(mm/s)	Gaussian	Annular Ring with 15% Plateau Fill	Annular Ring with 35% Plateau Fill
0.2	B	3H	5H
0.4	2B	HB	H
0.6	4B	HB	B
0.8	5B	2B	B
1	5B	3B	3B
1.2	6B	5B	5B
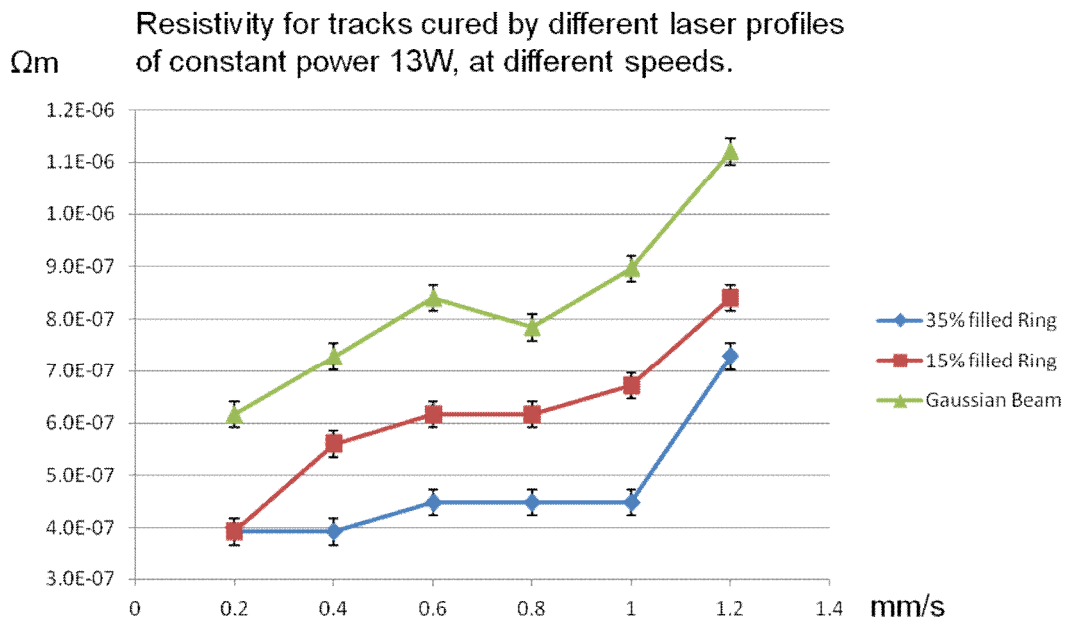
Fig 4.21. Resistivity of ink tracks cured under different laser beam profiles

Fig 4.21 displays the resistivity of the cured samples, with errors of $\pm 2.5 \times 10^{-8}$ á m (as a result of errors in resistance measurements taken with the Digimess RLC meter) . It is clear that the 35% filled beam profile provides better conductivity at every processing speed. The improvement is significant since the electrical conductivity achieved with this profile is almost twice as high as that achieved with the Gaussian profile, at every processing speed. Also the 15% filled profile gives much higher conductivity compared with the Gaussian beam.

This confirms that the better adhesion provided by the 35% filled ring profile mirrors its superiority in terms of conductance.

These experimental results agree with the model simulations using generic inks discussed in section 4.3.3, and show that the plateau filled annular ring beam profiles produced by using the SunShaper can indeed significantly improve curing performance. For this particular application the 35% filled profile gives better results than other intensity distributions.

Simone [9] found that õIn the range analyzed, both the adhesion and the curing of the polymer were found to correspond with the same operative conditions. Therefore, we have been able to optimize the adhesion index to guarantee a high performance of the process.ö This agrees with the result achieved in this study, which suggests that the 35% fill offers the best adhesion and conductance.

4.4 LADW process with Carbon based D1 ink

In this section curing processes for different inks are investigated, using the D1 ink and its individual components provided by GEM. Each material is firstly studied with STA analysis. The model is then adjusted from a generic ink parameter input set to accurately reflect the ink properties. The simulation results are then compared with actual curing results to verify the validity of the model for different types of inks.

4.4.1 Direct results of STA analysis

STA results for the following inks and components have been obtained with the Perkin Elmer STA 6000 system: D1 carbon ink, glycerol, methyl carbitol, trixene, trixene and epiko. Figs 4.22-24 show the results obtained from the STA system interface.
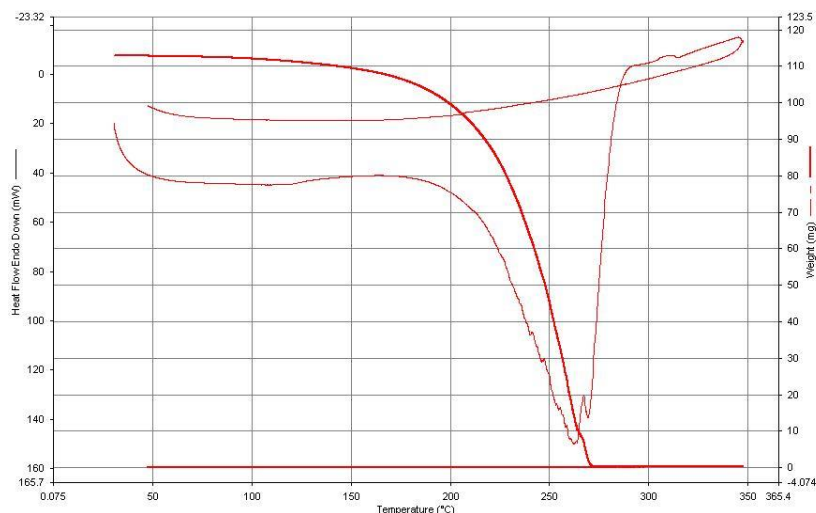
Fig 4.22 Weight change and heat flow of glycerol as function of temperature

Sample weight and heat flow evolution of glycerol are presented in Fig 4.22. Temperature is measured in ^{o}C. The thicker red line represents the weight of the sample as a function of temperature, showed by the scale on the right hand side vertical axis; Heat flow during the heating and cooling process is shown by the left hand side vertical axis and represented with the thinner line.

Glycerol starts to lose weight quickly once the temperature reaches 150 ^{o}C and is completely evaporated at 270 ^{o}C. The heat flow shown in this measurement includes the crucible that holds the sample; to obtain any normalised measurement of the sample the baseline heat flow has to be subtracted from the data, as shown in the next section.
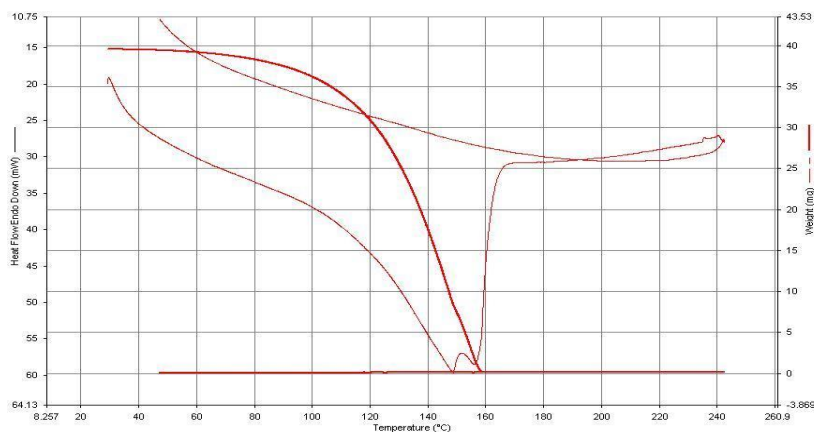
Fig 4.23 Weight change and heat flow of methyl carbitol as function of temperature.

It can be clearly seen in Fig 4.23 that methyl carbitol starts to evaporate around 80 ^{o}C and becomes completely vaporised at 160 ^{o}C.
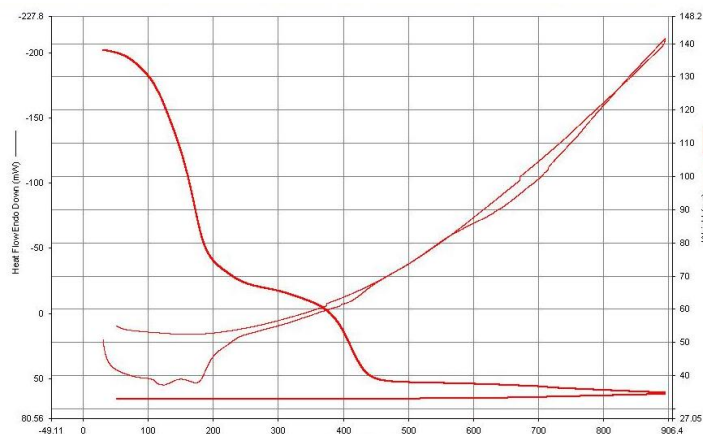
Fig 4.24 Weight change and heat flow of D1 Ink as function of temperature

Fig 4.24 displays the curves for D1 ink. The gradient of the curve changes significantly at ~200 ^{o}C and ~400 ^{o}C, indicating critical physical and chemical changes at these temperatures.

4.4.2. Weight loss and heat flow analysis

For better analysis and understanding of the thermal process, numerical data is exported and reinterpreted. Since the heating process applies only to the single pass LADW model, data of the cooling cycle is omitted for clarity. Weight and heat flow of samples are also normalised to 100mg for ease of direct comparison.

Empty Crucible
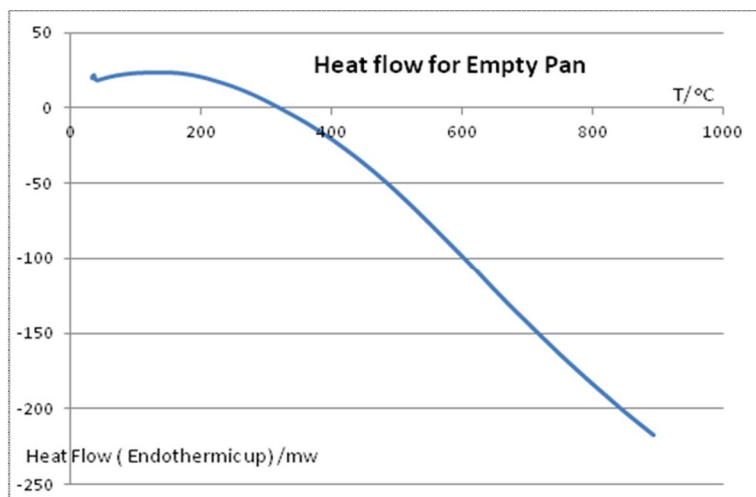
Fig 4.25 Heat flow of the empty reference crucible.

Fig 4.25 shows the heat flow involved for heating the empty reference crucible. This is the heating required to steadily increase the crucible temperature from 30 ^{o}C to 900 ^{o}C at a 5 ^{o}C/min rate. As shown, initially ~25mW is required, this gradually drops to 0 mW at 320 ^{o}C. The process then becomes increasingly exothermic as temperature rises. This reference calibration heat flow curve has to be deducted from all heat flow measurements, in order to reflect the true heat flow of samples. The mass of the crucible remains constant during the heat cycle as expected.

Trixene
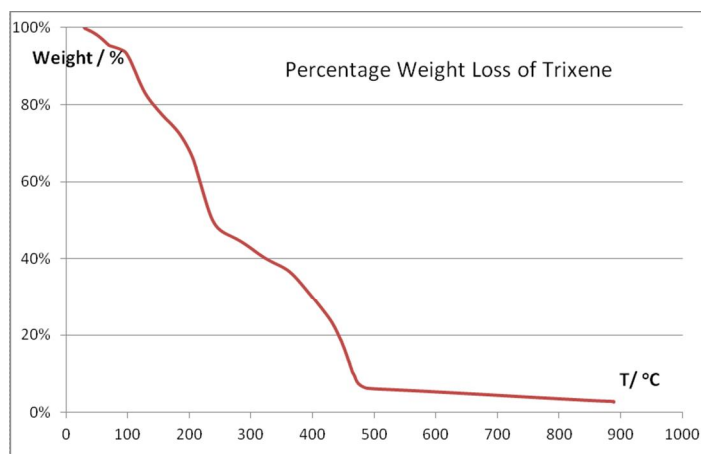
Fig 4.26 Percentage weight loss of Trixene as a function of temperature.

Trixene loses its mass at a relatively steady rate as temperature rises. Firstly, one can notice the activation of isocyanides at 90 ^{o}C. The polymer starts to break down gradually after ~270 ^{o}C. At 472 ^{o}C only 8% of its residue weight remains, and then slowly approaches zero as the temperature reaches 900 ^{o}C.
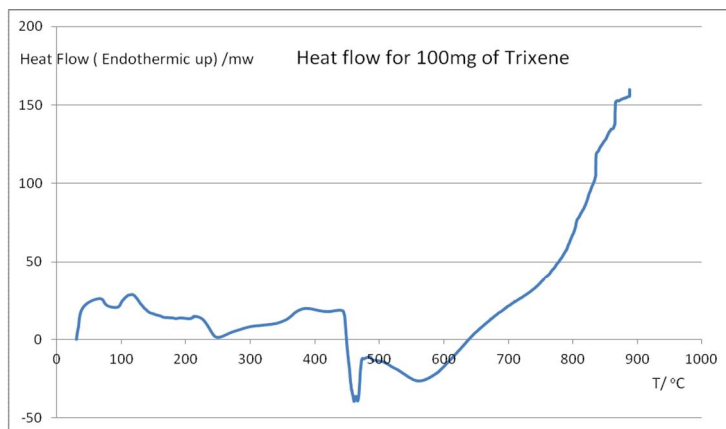
Fig 4.27 Heat flow of 100mg of trixene.

Fig 4.27 is the normalised heat flow curve for 100mg of Trixene. Over 472 ^{o}C, the flaming of the polymer triggers a major exothermic process. As this stage would already have been classified as overcured in an ink scenario, and therefore quantifications of this exothermic feature is irrelevant to the study.

Trixene + Epikote

Trixene and Epikote were mixed at one-to-one ratio before being heated. The weight loss curve and heat flow are plotted in Fig 4.28 and Fig 4.29. After activation at 90 ^{o}C, trixene becomes unblocked and react with the pendant hydroxyl in epikote, thus induce epikote to cross-link and pull the conductive particles into contact.
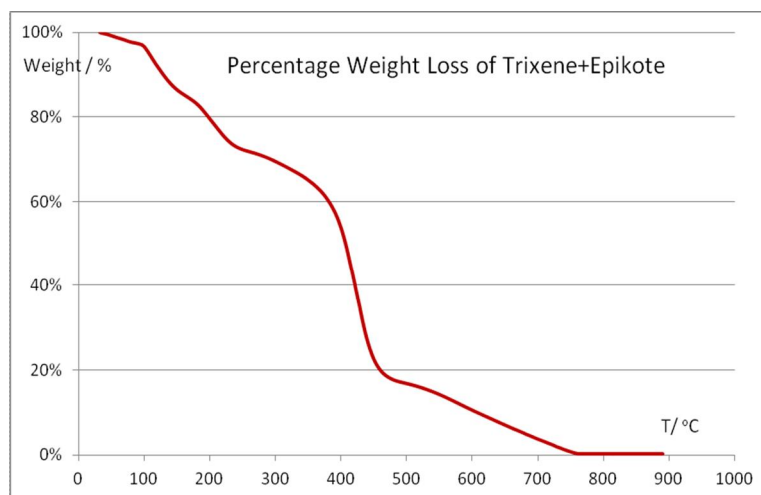
Fig 4.28 Percentage weight loss of Trixene+ Epicote as a function of temperature.

Epikote only starts to lose mass at T > 350 ^{o}C , resulting in the sharp fall of mass for 350 ^{o}C < T < 472 ^{o}C. At 472 ^{o}C most Trixene has been consumed. Epikote weight loss will dominate the gradient of the curve, where a clear decrease in weight loss rate can be seen. At 734 ^{o}C less than 1% mass remains. The overcuring temperature should be the temperature above which the cross-linking resin (Epikote) starts to break down, ie, the actual overcuring temperature should be 350 ^{o}C as suggested in Fig 4.28, which is very close to the model first estimate of 330 ^{o}C.
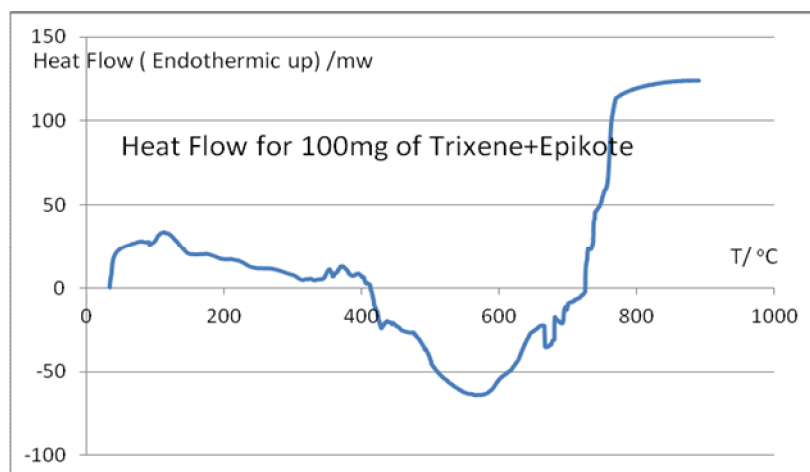
Fig 4.29 Heat flow of 100mg of Trixene+ Epicote.

Fig 4.29 shows endothermic reactions of decreasing heat flow took place, due to steadily reduced mass and exothermic features of polymer breakdown at higher temperature.

D1 ink

Fig 4.30 shows the weight loss curve of D1 ink. From this curve one can derive the exact mixing ratio of the individual components. Denoting the portion by mass of Methyl Carbitol, resin and carbon content with M_S, M_R and M_C respectively then:

$$M_S + M_R + M_C = 1 \qquad (4.6)$$

At 160 ^{o}C the total mass loss is 27%: It is known that methyl carbitol will have been completely vaporised at this temperature (Fig 4.21). Resin loses 15% of its mass.

$$M_S + 15\% M_R = 27\% \qquad (4.7)$$

At 734 ^{o}C only 26.2 % of D1 ink remains, which should be Carbon (including Timrex and Conductex SC), as all other components should have been consumed at this temperature (Fig 4.28.)

$$M_C = 26\% \qquad (4.8)$$

Solving eqn 4.5, 4.6 and 4.7 results $M_C = 26\%$, $M_S = 19\%$ and $M_R = 55\%$
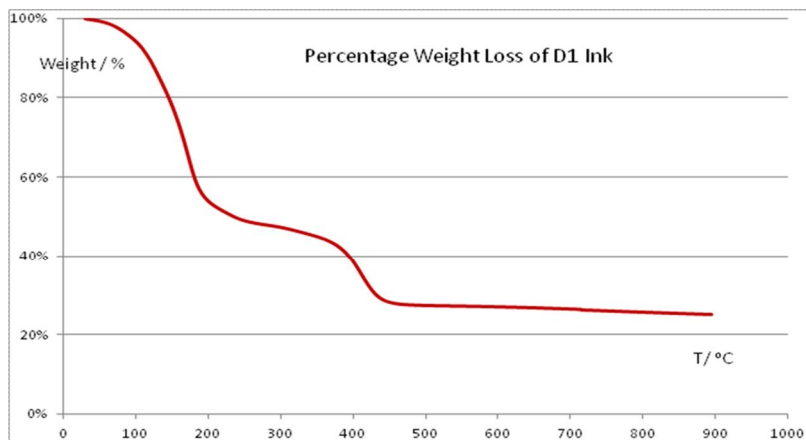
Fig 4.30 Percentage weight loss of D1 Ink as a function of temperature.
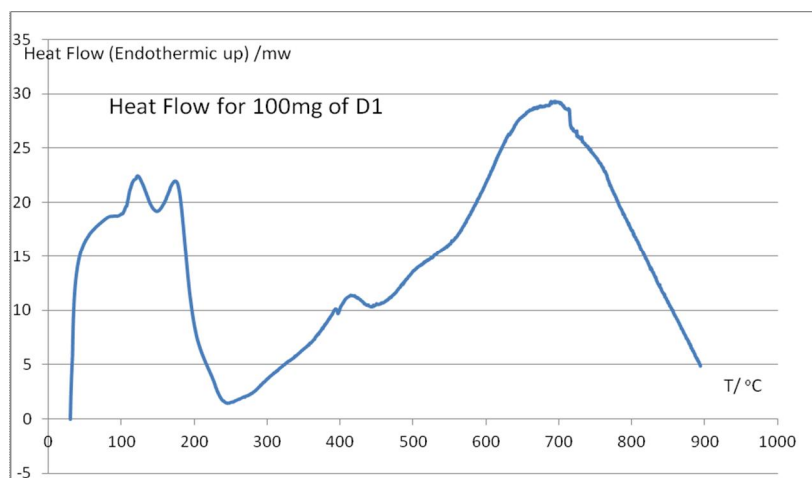
Fig 4.31 Heat flow of 100mg of D1.

In Fig 4.30 one can clearly see that the stages involved in the thermal curing process reflect the model proposed in chapter 2.5. Solvent becomes totally evaporated at 180 ^{o}C, after which the ink starts to cure with minor weight loss up to ~350 ^{o}C, after which the polymer starts to break down and the ink becomes overcured.

It is also very important to note that the integration of the area under the curve in Fig 4.31 up to 350 ^{o}C is very close to the integration of the area under the curve in Fig 2.7, thus again validates the accuracy of the original model.

4.4.3 Parameter modification of the Model for D1 ink

The result of DTA analysis suggests that the input parameters of the FEM model need to be modified from generic materials to reflect actual ink components and properties. In the case of the D1 ink, density, specific heat capacity, absorption and thermal conductivity need to be changed accordingly.

The analysis in section 4.4.2 suggests the actual ink contains 26% carbon, 19% methyl carbitol and 55% resin.

Therefore the density of the D1 ink is:

$$\rho_{ink} = \frac{1}{\dfrac{26\%}{\rho_{carbon}} + \dfrac{19\%}{\rho_{sol}} + \dfrac{55\%}{\rho_{res}}} = 1.26 \times 10^3 \, kg/m^3 \tag{4.9}$$

Since the carbon content is highly absorbing at CO_2 wavelength, the absorption coefficient is taken as A=1 for the track regardless of whether it is cured or not.

The thermal conductivity of cured ink is calculated based on the presumption of same packing factor as in the cured D58 ink:

$$\frac{k_{D1}}{k_C} = \frac{k_{D58}}{k_S} \tag{4.10}$$

$$k_{D1} = \frac{k_{D58}}{k_S} k_C = 2.8 w/m \tag{4.11}$$

where k_{D1}, k_C, k_{D58} and k_S are the thermal conductivity of cured D1 ink, pure graphite, cured D58 ink and silver, respectively.

And therefore k_{D1} will follow the curve shown below in Fig 4.32

The heat capacity of the ink is described by,

$$C_{Peff} = \frac{Ht}{m\Delta T} \tag{4.12}$$

where H is the heat flow, t is time of the process, T is the temperature increment and m is sample mass.

The heat flow is collected in the STA analysis and displayed in Fig, in this case,

$$m = 100mg = 10^{-4}\,kg \qquad (4.13)$$

$$\frac{t}{\Delta T} = 12S/^{o}\,C \qquad (4.14)$$
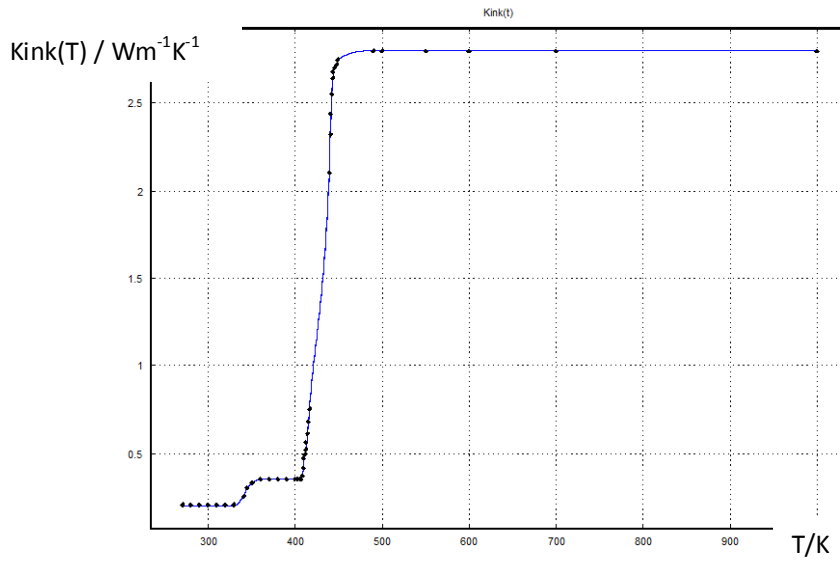
Fig 4.32 Modified conductivity function for D1 ink

H can be approximated with the following interpolation Fig 4.33.
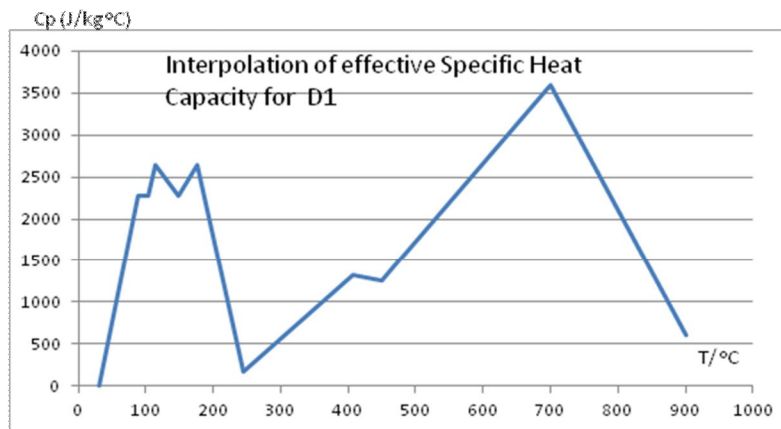
Fig 4.33 Modified specific heat capacity function for D1 ink

Thus, an interpolation for the heat capacity can be obtained and input into the FEM model.

4.4.4 Simulation and experimental results:

To investigate the actual curing performance of D1 ink, track samples were made using the õdoctorr bladeö method introduced in Chapter 3. The tracks are 100 micron thick, 2.8 mm wide; and are deposited on alumina substrates.

Since the thermal conductivity of the substrate is fixed, instead of parametric surfaces, two curves are generated with simulations as the process window for D1 ink, as shown in Fig 4.34
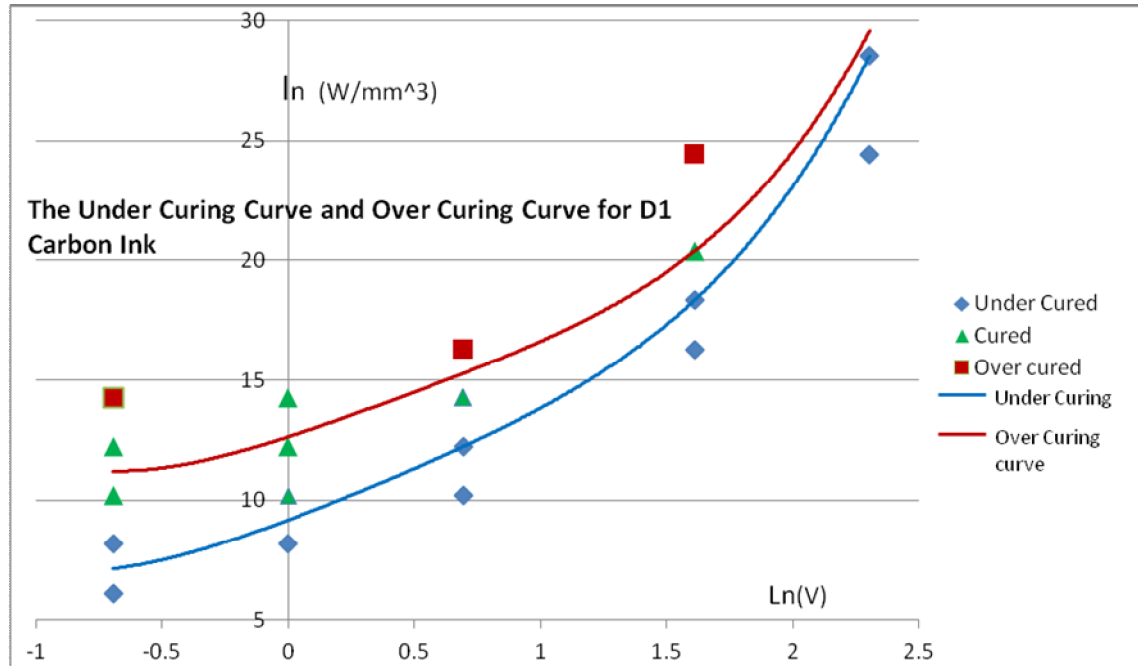
Fig 4.34 Simulation outcome compared with experimental results for D1 ink

In Fig 4.34, the vertical axis is the normalised intensity, and the horizontal axis is the traverse speed on a logarithmic scale. In this case only alumina was used, therefore the substrate thermal conductivity is fixed, and instead of the two surfaces shown in Fig 4.10, here there are two curves bounding the curing window. The model suggests that processes below the under curing curve or above the over curing curve would result in under curing or over curing.

The samples were cured with the Synrad laser system (Chapter 3) with a range of parameters, and the results were fitted onto Fig 4.34. On the graph there are only 3 anomalies out of 19 data points, indicating excellent agreement with the model.

Thus the model is shown to have validity for inks of different compositions and thermal properties.

In work by Friis-Pedersen [169], an epoxy resin containing dicyandiamide and an accelerator (diurone) was investigated under different cure cycles. The mathematical prediction of the degree of cure in a thermoset as a function of time and temperature was investigated and compared to measured data.

Modulated differential scanning calorimetry (DSC) was used to measure the changes in the heat capacity during curing, which was to some degree supported by measurements of the primary amine conversion and hydroxyl production. These findings agree with the results obtained through the DSC analysis in this study (though the materials are largely different, the chemical process of curing is largely similar). In Friis-Pedersen's study, the mathematical model did not incorporate these differences, and this had led to discrepancies between the predicted and actual values of the degree of curing; On the other hand, in this work the measured heat capacity is substituted into the original generic model, and obtained updated simulations that match experimental curing results.

In Frii-Pedersen's work, near-infrared analysis was used to measure the conversion of epoxy and primary amine and the production of hydroxyl. NIRS is a spectroscopic method that uses the near-infrared region of the electromagnetic spectrum (from about 800 nm to 2500 nm. Near-infrared spectroscopy is based on molecular overtone and combination vibrations. NIR can typically penetrate much farther into a sample than mid infrared radiation. Near-infrared spectroscopy can be very useful in probing bulk material with little or no sample preparation.

The molecular overtone and combination bands seen in the near IR are typically very broad, leading to a complex spectra; it can be difficult to assign specific features to specific chemical components [235-238]. However, NIRS analysis equipment was not available for this work.

This work is dedicated to single-pass laser curing. In reality, to avoid overly large temperature gradients during cure caused by the strong exothermic curing reactions (Fig 4.27 and Fig 4.29), the curing process of epoxy is performed with cure cycles [20, 192, 195, 219]. In this approach, some of the heat generated by the curing reactions is removed at moderate

temperatures, and this prevents a strong exothermic temperature peak. After a certain period, the temperature is then increased to obtain a fully cured material. With this approach, the large temperature gradients otherwise encountered at elevated curing temperatures can be avoided. However, because of the different reaction mechanisms at high and low temperatures, different cured material properties may be achieved, depending on the cure cycle.

4.5 Variations in processing conditions and parameters

In this chapter, the proposed model has been compared with experimental results, demonstrating validity over a range of processing parameters:

- different substrate specific heat capacity and thermal conductivity
- different ink composition, density, specific heat capacity, thermal conductivity and absorption coefficient.
- different laser traverse speed and fluence.

There are other factors which have been taken into account in the study; however the sensitivity of the process with variations in these factors need to be studied in the future:

- Change in beam size: A larger beam size will result in more heat absorbed by the substrate, thus elevating the temperature of the substrate and reduce the temperature differential across the interface with ink track. Therefore, given a fixed fluence, a larger beam size will slow down the temperature drop within the ink track.
- Change in substrate size: In this model, the substrate acts as a heat sink, therefore a larger (wider or thicker) substrate will offer less temperature rise after a cure cycle.
- Change in ambient temperature: a lower ambient temperature (or more active air cooling) would result in more heat loss through convection and radiation, from both the ink track and the substrate, and therefore less temperature rise, with all heating conditions fixed.
- Change in Laser wavelength: with this variation, a new mechanism is possibly involved and therefore is recommended as future work.

5. Conclusions and future work

A summary of the complete study is presented in this chapter, followed by a list of conclusions. Finally possible areas related to the topic of study are suggested, where future research of interest might be carried out.

5.1 Conclusion

This work studies Laser Assisted Direct Write technology with a novel parametric FEM model which simulates the thermal profile during the LADW process and gives indicative outputs that can be compared with a series of experimental results. The validity of the model was firstly verified in this study, then it was used to simulate curing processes with different parameters which are otherwise difficult to predict (such as curing with different intensity distributions and different inks).

5.1.1 Summary of work presented in this study

Firstly the current state of the art of additive manufacturing techniques were reviewed in a discussion of the comparative advantages of various deposition methods. The review was divided into two main parts namely õNon-laser basedö and õLaser basedö printing and deposition technologies, including a brief introduction to the principles of lasers.

The focus was then shifted to the advances of LADW technology over recent years, highlighting the applications of this technology and the need for the research work conducted in this study. The review also discussed in detail the research work done in the field of conductive inks, beam shaping and mathematical modelling of the LADW process.

The remainder of the literature review outlined the fundamental mathematical principles of Finite Element Method which is the pillar of the model construction throughout this work. Important concepts such as variational methods, basis, elements, functional space, Hilbert space, stiffness matrix were introduced and explained in the context of the study.

The second chapter detailed the theoretical formulation of LADW. Starting by laying out the configuration of a laser curing set-up, two key processing parameters were introduced in advance: the materials used in the process (for both ink and substrate), and the laser intensity distribution used for processing.

The theoretical formulation of LADW process was then introduced as the Curing Mechanism. The nonlinear nature of ink was analysed mathematically and characterised with three interpolated functions: effective specific heat capacity, absorption coefficient and thermal conductivity. A generic formulation was constructed based on the Fresnel heat equations, coupled with appropriate boundary conditions. The criteria for defining curing results were also determined, based on a set of assumptions.

The last part of Chapter 2 detailed the construction of the FEM model in the COMSOL 4.0 environment. A model architecture was derived from the curing mechanism formulation. After introduction of COMSOL and the hardware requirement, a step-by-step guide of model building was shown, including the physics PDEs, geometry build-up, boundary conditions, meshing, calculation and interpretation of results.

Chapter 3 listed the materials and equipment used in the experimental part of the study. The processing equipment include the Synrad Laser Marking system, fluid dispensing robot, the SunShaper unit, beam attenuator and Solsurf Laser processing system. The Laserdec beam analyser, Elcometer and Digimess RLC meter were used to analyse cured samples. The properties of inks and substrates were categorised and presented in further section, with ink thermal properties carefully analysed with the Perkin Elmer STA 6000 system.

The procedure of the experiments was interpreted: Sample tracks were made with either doctor blade method or using the CNC deposition robot. The finished ink tracks were then shifted on the Synrad system or the Solsurf system (in which case LADW with a shaped beam was investigated).

The content of experimental work firstly involved modelling the curing performance of a generic ink (which is made up to mirror D58 ink) and comparing the simulation outputs with the experimental curing results obtained by the author and others. Once the model was validated, investigation of the effect of beam shaping on the LADW process was carried out using the SunShaper. The last target study was to verify the model validity for inks of different composition and thermal property. To assist the study, GEM provided a carbon based D1 ink, individual components and the approximate mixing ratios. STA analysis was then conducted to obtain the thermal properties of the ink and each component during the thermal curing process. The data was then used to modify the model to match the conditions of curing of the D1 ink samples, thus verifying the model validity for different inks.

Chapter 4 presented the results of all theoretical simulations and experiments, along with analysis and discussion of these results. Firstly, the thermal evolution of the ink tracks during the LADW process was studied with simulations. Then a parametric curing window was produced for a range of traverse speeds, laser intensity and substrate materials. This window was shown to be valid by comparison with experimental results. Curing with different intensity profiles was then investigated. Experimental and model results agreed in suggesting that an annular filled ring profile provides considerable improvement compared to Gaussian beams.

In the final part of the study, model input parameters were modified to match the properties of D1 ink after running STA analysis for the ink and each component. Experimental data supported the model and showed its validity for different inks with different composition and thermal properties.

5.1.2 Conclusions of study

This theoretical and experimental study of LADW technology yields a series of valuable conclusions as listed below:

I. The mechanism of a single pass LADW process can be regarded as a non-linear heating cycle, illustrated in Fig 2.6 and formulated by Eqn 2.5-2.10. The specific thermal behaviour of the ink depends on its components and their relative mixing ratios. For any particular combination of components, the ink non-linear thermal-physical properties (including effective specific heat capacity, thermal conductivity and optical absorption coefficient) can be calculated using Eqn 2.11-2.23.

II. To incorporate the mechanism in to a FEM model, the following factors need to be achieved:

i) Solid 3D geometry with dimensions matching the physical sample.

ii) Materials and properties correctly defined to each geometrical domain.

iii)The governing PDE is Eqn 2.24, with appropriate conducting and insulating boundary conditions as shown with Eqn 2.25-2.28.

iv) Simulate a time dependent study that outputs the temperature field.

III. Model outputs are categorised by applying a curing criterion, which classifies the process results as cured, undercured and overcured.

IV. The temporal studies of simulation results clearly demonstrate the non-linear thermal properties of the ink.

V. A 3D curing map was constructed and accurately projects a parametric window in which successful curing can be achieved. The map is shown as two non-intersecting surfaces that define a parametric subspace. Experimental results were tested to support the model.

VI. Different laser intensity profiles can be easily incorporated into the model. The model predicts that a 35% filled annular ring would result in superior curing quality over Gaussian and top-hat intensity profiles, provided other parameters are unchanged. This argument was validated with experimental results.

VII. STA analysis offers numerical data of the thermal properties of real ink components, which has been loaded into the model for improvement of accuracy.

VIII. The model simulation for D1 ink was tested against experimental result. A curing window was created for alumina substrate, and the model was validated.

In general, the proposed FEM model can simulate a LADW process to a very good degree of accuracy, provided the information of processing conditions and basic properties of the materials are used. The model can be used to generate a range of suitable processing parameters for a particular curing application. Also, it can predict the effect of different beam intensity profile on the process. Coupled with empirical data obtained from STA analysis, the model is able to give accurate predictions for various inks accordingly.

5.2 Future work

5.2.1 FEM Model for Multi-pass LADW processes

The FEM Model presented in this work focuses on single pass curing process. In practice, engineers often choose to achieve the desired curing conditions with multiple passes. In such a process both solvent evaporation and polymer cross-linking take place over a number of heating cycles induced by each pass, therefore the modelling of this involves a more complex theoretical formulation, which can be based on the foundation presented in this study, though significant development will be required.

5.2.2 Thermal stress generated during LADW

It has been found that when curing with a laser beam, the heat distribution generates thermal stress in the substrate and thus can sometimes lead to fracture (in the case of alumina) or plastic deformation (in the case of PET). Hence it is very important to be able to predict the level of stress generated and modify the parameters to prevent substrate damage.

Thermal stress can be induced by one or more of the following:

- Temperature gradient: caused by cooling on the surface, unevenly distributed heat source, etc.

- Thermal expansion mismatch: anisotropy in thermal expansion coefficient within the material.

- Volume changes caused by phase transformations.

In the laser curing process, temperature gradient is the primary source of any thermal stress, which is described with the following equation:

$$\underline{\sigma} - \underline{\sigma}_0 = \underline{\underline{D}}[\underline{\varepsilon} - \alpha (T - T_0) - \underline{\varepsilon}_0]$$

where   is the stress vector, D is the elasticity matrix,   is the strain vector,   is the linear thermal expansion coefficient and T is the temperature reached.

Building an accurate model that can calculate the stress induced in the substrate during the laser curing process, to indicate whether the laser power used may cause any damage in the substrate is therefore crucially useful in the use of the LADW method on pre-existing geometries, for example, aircraft wings.

5.2.3 Formulation of the Chemistry involved in the process

This work investigates the LADW process from a purely thermal-physical aspect. Formulation of the detailed microscopic chemical reactions is beyond the author's knowledge. More detailed understanding of the chemistry can potentially greatly improve the model.

5.2.4 Validation of models by temperature monitoring

Thermal imaging cameras can be employed to monitor the thermal evolution of the ink track during LADW processes, thus validating model simulations.

6. References

1. Abraham, M. and H. Helvajian, *Laser direct write for release of SiO2 MEMS and nano-scale devices*, in *Fifth International Symposium on Laser Precision Microfabrication*, I.H.H.I.K.K.F.O.A. Miyamoto and K. Sugioka, Editors. 2004. p. 543-550.
2. Anagnostou, D.E., G. A.A, and A. A.K, *A direct-write printed antenna on paper-based organic substrate for flexible displays and WLAN applications.* IEEE/OSA Journal of Display Technology, 2010. **6**(11): p. 558-564.
3. Gabureac, M.S., et al. *High spatial resolution Hall nano-sensors by tuned direct-write Co/C-FEBID*. 2011.
4. Han, S.I. and S.H. Jeong, *Laser-assisted chemical vapor deposition to directly write three-dimensional microstructures.* Journal of Laser Applications, 2004. **16**(3): p. 154-159.
5. Hest, M.F.A.M.V., H. S.E, and U. J.M, *Direct write metallization for photovoltaic cells and scaling thereof*, in *Conference Record of the IEEE Photovoltaic Specialists Conference*2010: Honolulu, HI. p. 3626-3628.
6. Hoey, J.M., R. M.T, and H. A, *Rapid prototyping RFID antennas using direct-write.* IEEE Transactions on Advanced Packaging, 2009. **32**(4): p. 809-815.
7. Ivan, M., et al. *Direct Laser Write (DLW) as a versatile tool in manufacturing templates for imprint lithography on flexible substrates.* in *Proceedings of SPIE - The International Society for Optical Engineering*. 2009.
8. Kattamis, N.T., et al., *Laser direct write printing of sensitive and robust light emitting organic molecules.* Applied Physics Letters, 2009. **94**(10).
9. Simone, G., *An experimental investigation on the laser cure of thermosetting powder: An empirical model for the local coating.* Progress in Organic Coatings, 2010. **68**(4): p. 340-346.
10. Khan, A., R. N, and M. V. *Laser sintering of direct write silver nano-ink conductors for microelectronic applications.* in *SPIE - The International Society for Optical Engineering*. 2008. San Jose, CA.
11. Lee, M.-T., et al., *Rapid selective metal patterning on polydimethylsiloxane (PDMS) fabricated by capillarity-assisted laser direct write.* Journal of Micromechanics and Microengineering, 2011. **21**(9).
12. Longtin, J., et al., *Sensors for Harsh Environments by Direct-Write Thermal Spray.* IEEE Sensors Journal, 2004. **4**(1): p. 118-121.
13. Mathews, S.A., R.C.Y. Auyeung, and A. Pique, *Use of Laser Direct-Write in Microelectronics Assembly.* Journal of Laser Micro Nanoengineering, 2007. **2**(1): p. 103-107.
14. Sato, T., et al., *Laser-assisted Direct Write for aerospace applications.* Proceedings of the Institution of Mechanical Engineers, Part G: Journal of Aerospace Engineering.
15. Shang, S., et al., *A predictive thermal dynamic model for parameter generation in the laser assisted direct write process.* Journal of Physics D: Applied Physics, 2011. **44**(43).
16. Swider-Lyons, K.E., et al., *Direct write microbatteries for next-generation microelectronic devices*, in *Electroactive Polymers and Rapid Prototyping*, Y.Z.Q.M.F.E.B.S.C.D.B.D.S.C. BarCohen, Editor 2002. p. 265-273.
17. Wang J., A., K. H, and C. N.A, *Three-dimensional printing of interconnects by laser direct-write of silver nanopastes.* Advanced Materials, 2010. **22**(40): p. 4462-4466.
18. Wellburn, D., *Circular Laser Beam Intensity Profile Shaping for Uniform Surface Treatments*, in *Laser Group*2010, University of Liverpool.
19. Caricato, A.P. and A. Luches, *Applications of the matrix-assisted pulsed laser evaporation method for the deposition of organic, biological and nanoparticle thin films: a review.* Applied Physics a-Materials Science & Processing, 2011. **105**(3): p. 565-582.
20. de Angelis, M., et al., *Axially symmetric hollow beams using refractive conical lenses.* Optics and Lasers in Engineering, 2003. **39**(3): p. 283-291.

21. Lewis, L.L., et al., *Isothermal frontal polymerization: Confirmation of the mechanism and determination of factors affecting the front velocity, front shape, and propagation distance with comparison to mathematical modeling.* Journal of Polymer Science Part a-Polymer Chemistry, 2005. **43**(23): p. 5774-5786.

22. Edited by Mazumder, J.C., O; Villar, R; Steen, W, *Laser Processing: Surface Treatment and Film Deposition.* Series E: Applied Science. Vol. 307. 1994, Dordrecht/ Boston/ London: Kluwer Academic Publishers.

23. Edited by Mazumder, J.C., O; Villar, R; Steen, W, *Proceedings of the NATO Advanced Study Institute on Laser Processing: Surface Treatment and Film Deposition*1994, Dordrecht, The Netherlands: Kluwer Academic Publishers.

24. Harris, M.L., et al., *Recent progress in CAD/CAM laser direct-writing of biomaterials.* Materials Science & Engineering C-Biomimetic and Supramolecular Systems, 2008. **28**(3): p. 359-365.

25. Pique, A., *Direct Write Technology for Rapid Prototyping Applications.* Academic Press.

26. Ahmad, Z., et al., *Novel electrically driven direct-writing methods with managed control on in-situ shape and encapsulation polymer forming.* International Journal of Material Forming, 2011: p. 1-8.

27. Alemohammad, H., E. Toyserkani, and Asme, *MECHANICAL AND ELECTRICAL PROPERTIES OF MICRO-LINES FABRICATED BY LASER-ASSISTED MASKLESS MICRODEPOSITION.* Imece2008: Proceedings of the International Mechanical Engineering Congress and Exposition - 2008, Vol 62009. 11-16.

28. Bhattacharya, S., M. V, and *Simple, inexpensive, and reliable, high density interconnect technology for flexible electronics applications.* in *2009 Flexible Electronics and Displays Conference and Exhibition, FLEX 2009.* 2009.

29. Imperiale, S. and P. Joly, *MATHEMATICAL AND NUMERICAL MODELLING OF PIEZOELECTRIC SENSORS.* Esaim-Mathematical Modelling and Numerical Analysis-Modelisation Mathematique Et Analyse Numerique, 2012. **46**(4): p. 875-909.

30. Liang, J., C. Y, and X. Y, *Toward all-carbon electronics: Fabrication of graphene-based flexible electronic circuits and memory cards using maskless laser direct writing.* ACS Applied Materials and Interfaces, 2010. **2**(11): p. 3310-3317.

31. Sameshima, T., *Laser crystallization for large-area electronics.* Applied Physics a-Materials Science & Processing, 2009. **96**(1): p. 137-144.

32. Trocha, P. and J. Barnas, *Large enhancement of thermoelectric effects in a double quantum dot system due to interference and Coulomb correlation phenomena.* Physical Review B, 2012. **85**(8).

33. Yao, K., et al., *Screen-printed piezoelectric ceramic thick films with sintering additives introduced through a liquid-phase approach.* Sensors and Actuators, A: Physical, 2005. **118**(2): p. 342-348.

34. Yoon, B., et al., *Inkjet printing of conjugated polymer precursors on paper substrates for colorimetric sensing and flexible electrothermochromic display.* Advanced Materials, 2011. **23**(46): p. 5492-5497.

35. Zunino, J., S. D.P, and P. A.M. *Inkjet printed devices for armament applications.* in *Nanotechnology 2010: Electronics, Devices, Fabrication, MEMS, Fluidics and Computational - Technical Proceedings of the 2010 NSTI Nanotechnology Conference and Expo.* 2010. Anaheim, CA.

36. Wijshoff, H. *Free surface flow and acousto-elastic interaction in piezo inkjet.* 2004.

37. Beroz, J., et al., *Four degree of freedom liquid dispenser for direct write capillary self-assembly with sub-nanoliter precision.* The Review of scientific instruments, 2012. **83**(1): p. 015104.

38. Buyukhatipoglu, K., et al., *Bioprinted Nanoparticles for Tissue Engineering Applications.* Tissue Engineering Part C-Methods, 2010. **16**(4): p. 631-642.

39.   Chang, R., Y. Nam, and W. Sun, *Direct cell writing of 3D microorgan for in vitro pharmacokinetic model.* Tissue Engineering Part C-Methods, 2008. **14**(2): p. 157-166.

40.   Lin, L.-F., et al., *Role of Endoscopic Ultrasound-guided Fine-needle Aspiration in Lung and Mediastinal Lesions.* Journal of the Chinese Medical Association, 2010. **73**(10): p. 523-529.

41.   B Li, K.C., *Active mixing and depositing /patterning of materials*.

42.   *Inkjet technologies.* AP Australian Printer Magazine, 2003(AUG.): p. 50-51.

43.   Barret, M., S. Sanaur, and P. Collot, *Inkjet-printed polymer thin-film transistors: Enhancing performances by contact resistances engineering.* Organic Electronics, 2008. **9**(6): p. 1093-1100.

44.   Chen, T. and Sist, *Inert Piezoelectric Inkjet Print Head Technology for Alkaline Etch Process in Solar Cell Fabrication.* Nip 25: Digital Fabrication 2009, Technical Program and Proceedings2009. 635-638.

45.   Hopkins, A.R., D.C. Straw, and K.C. Spurrell, *Influence of surface chemistry on inkjet printed carbon nanotube films.* Thin solid films, 2011. **520**(5): p. 1541-1545.

46.   Jeong, S., S. H.C, and L. W.W, *Preparation of aqueous Ag ink with long-term dispersion stability and its inkjet printing for fabricating conductive tracks on a polyimide film.* Journal of Applied Physics. **108**(10).

47.   Karpour, A. and S.R. Wenham. *The importance of surface roughness in the adhesion of electroless-plated metal in inkjet printed grooves*. 2010.

48.   Chen, T., *Novel inkjet print head for manufacturing processes*, in *International Conference on Digital Printing Technologies*2008: Pittsburgh, PA. p. 113-116.

49.   Lee, J.K., et al., *Direct writing of semiconducting polythiophene and fullerene derivatives composite from bulk heterojunction solar cell by inkjet printing.* Thin solid films, 2011. **519**(16): p. 5649-5653.

50.   Lim, J.A., et al., *Inkjet-Printed Single-Droplet Organic Transistors Based on Semiconductor Nanowires Embedded in Insulating Polymers.* Advanced Functional Materials, 2010. **20**(19): p. 3292-3297.

51.   Martin, G.D., et al., *Inkjet printing - the physics of manipulating liquid jets and drops*, in *Engineering and Physics - Synergy for Success*2008.

52.   Miettinen, J., et al., *Inkjet printed System-in-Package design and manufacturing.* Microelectronics Journal, 2008. **39**(12): p. 1740-1750.

53.   Orecchini, G., et al., *Inkjet Printed Organic Transistors for Sustainable Electronics*, in *2010 Proceedings 60th Electronic Components and Technology Conference*2010. p. 985-989.

54.   P Calvert, e.a., *Inkjet printing for materials and devices* Chem.Matter.

55.   Rida, A., et al., *Low Cost Inkjet-printing Paper-Based Modules for RFID Sensing and Wireless Applications*. Euwit: 2008 European Wireless Technology Conference2008. 294-297.

56.   Sim, W.-C., S.-J. Park, and J. Joung, *Performance analysis of an industrial inkjet printing head using the 1D lumped model.* International Journal of Precision Engineering and Manufacturing, 2008. **9**(2): p. 50-53.

57.   Tien, C.-H., C.-H. Hung, and T.-H. Yu, *Microlens Arrays by Direct-Writing Inkjet Print for LCD Backlighting Applications.* Journal of Display Technology, 2009. **5**(4-6): p. 147-151.

58.   van Hest, M.F.A.M., et al., *INKJET PRINTED CONTACTS FOR USE IN PHOTOVOLTAICS*, in *2009 34th Ieee Photovoltaic Specialists Conference, Vols 1-3*2009. p. 109-111.

59.   Yun, Y.H., et al., *Polymer Inkjet Printing: Construction of Three-Dimensional Structures at Micro-Scale by Repeated Lamination.* Macromolecular Research, 2009. **17**(3): p. 197-202.

60.   Finch, R.G., *Thick film materials.* Thin solid films.

61.   Zhang, G., et al., *Research on the quality of screen printing based on the UV ink*, 2012. p. 121-124.

62.   Do, J.S., S.H. Yu, and S.F. Cheng, *Thick-film nickel-metal-hydride battery based on porous ceramic substrates.* Journal of Power Sources, 2003. **117**(1-2): p. 203-211.

63. Kadara, R.O., et al., *Manufacturing electrochemical platforms: Direct-write dispensing versus screen printing.* Electrochemistry Communications, 2008. **10**(10): p. 1517-1519.

64. Xu, G., et al., *Research on solidification characteristics of resin in high-resolution Stereolithography system*, 2010. p. 3989-3992.

65. Harke, B., et al., *Photopolymerization Inhibition Dynamics for Sub-Diffraction Direct Laser Writing Lithography.* Chemphyschem, 2012. **13**(6): p. 1429-1434.

66. Darling, R.B. *Photolithography*. [http://www.ee.washington.edu/research/microtech/cam/PROCESSES/PDF%20FILES/Photolithography.pdf].

67. Ahn, K., B.W. Wessels, and S. Sampath, *Spinel humidity sensors prepared by thermal spray direct writing.* Sensors and Actuators, B: Chemical, 2005. **107**(1 SPEC. ISS.): p. 342-346.

68. Li, J., et al., *Interdigital capacitive strain gauges fabricated by direct-write thermal spray and ultrafast laser micromachining.* Sensors and Actuators a-Physical, 2007. **133**(1): p. 1-8.

69. Longtin, J.P., et al., *Direct-Write Thermal spray for sensors and electronics: An overview*. Digital Fabrication 2006, Final Program and Proceedings2006. 116-119.

70. Theophilou, T.S., et al., *Integrated heat-flux sensors for harsh environments using thermal-spray technology.* IEEE Sensors Journal, 2006. **6**(5): p. 1126-1133.

71. Tong, T., et al., *Ultrafast laser micromachining of thermal sprayed coatings for microheaters: Design, fabrication and characterization.* Sensors and Actuators, A: Physical, 2004. **114**(1): p. 102-111.

72. Morgan, R., et al., *Analysis of cold gas dynamically sprayed aluminium deposits.* Materials Letters, 2004. **58**(7-8): p. 1317-1320.

73. Novoselova, T., et al., *Experimental study of titanium/aluminium deposits produced by cold gas dynamic spray.* Surface and Coatings Technology, 2006. **200**(8): p. 2775-2783.

74. Boughaba, S., G. Auvert, and Y. Pauleau, *GROWTH-KINETICS OF MICROMETER-SIZE SILICON LINES PRODUCED BY DECOMPOSITION OF SILANE USING A LASER DIRECT-WRITING TECHNIQUE.* Journal of Applied Physics, 1994. **75**(7): p. 3635-3642.

75. Ben Naceur, J., et al., *Annealing effects on microstructural and optical properties of Nanostructured-TiO2 thin films prepared by sol-gel technique.* Current Applied Physics, 2012. **12**(2): p. 422-428.

76. Kim, K., S. Kim, and S.Y. Lee, *Effect of excimer laser annealing on the properties of ZnO thin film prepared by sol-gel method.* Current Applied Physics, 2012. **12**(2): p. 585-588.

77. Raghu, P., et al., *Sol-gel immobilized biosensor for the detection of organophosphorous pesticides: A voltammetric method.* Bioelectrochemistry, 2012. **83**(1): p. 19-24.

78. Seeni Meera, K.M., et al., *Sol-gel network silica/modified montmorillonite clay hybrid nanocomposites for hydrophobic surface coatings.* Colloids and Surfaces B: Biointerfaces, 2012. **90**(1): p. 204-210.

79. *Sol Gel Technology*.

80. Tsai, S.D., M.B. Suresh, and C.C. Chou, *Improvement in ferroelectric properties of PZT thick films prepared by a modified sol-gel technique using low temperature laser annealing.* Physica Scripta, 2007. **T129**: p. 175-179.

81. Yasuda, T., K. Nishikawa, and S. Furukawa, *Structural colors from TiO2/SiO2 multilayer flakes prepared by sol-gel process.* Dyes and Pigments, 2012. **92**(3): p. 1122-1125.

82. Zhu, C. and J.E. Smay, *Catenary shape evolution of spanning structures in direct-write assembly of colloidal gels.* Journal of Materials Processing Technology, 2012. **212**(3): p. 727-733.

83. Elijah Kannatey-Asibu, J., *Principles of laser materials processing*2009: John Wiley & Sons, Inc.

84. Rofin. *CO2 Lasers*. Available from: http://www.rofin.com/en/products/co2_lasers/.

85. Dong, J., et al., *Clinical efficacy of flumetasone/salicylic acid ointment combined with 308-nm excimer laser for treatment of psoriasis vulgaris.* Photodermatology Photoimmunology & Photomedicine, 2012. **28**(3): p. 133-136.

6. References

86.   Hsu, K.-Y., et al., *Diode-Laser-Pumped Glass-Clad Ti:Sapphire Crystal-Fiber-Based Broadband Light Source.* Ieee Photonics Technology Letters, 2012. **24**(10): p. 854-856.

87.   Li, Y.L., L.X. Zhang, and Y.C. Zhang, *All-solid-state CW intracavity frequency-doubling Nd:Lu2O3/LBO red laser at 679.5 nm.* Laser Physics, 2012. **22**(5): p. 839-841.

88.   Mavi, H.S., et al., *Raman-Study of Stress-Relieved Silicon-on-Sapphire Films Prepared by Cw-Laser Annealing.* Journal of Applied Physics, 1991. **69**(11): p. 7815-7819.

89.   Sato, T., et al., *Laser-Induced Backside Wet Etching Employing Green DPSS Laser and Liquid Metallic Absorber.* Journal of Laser Micro Nanoengineering, 2011. **6**(3): p. 204-208.

90.   Yang, X., L. Song, and L.X. Zhang, *All-solid-state continuous-wave frequency-doubling Nd:LuVO4/GBCOB laser at 533 nm.* Laser Physics, 2012. **22**(5): p. 836-838.

91.   Yang, X., L. Song, and Y.H. Zhang, *All-solid-state CW Nd:GdVO4-LBO red laser under direct 912 nm pumping.* Laser Physics, 2012. **22**(5): p. 832-835.

92.   Lasers, S. *SPI fibre lasers*. Available from: http://www.spilasers.com/products.aspx.

93.   Coherent. *Talisker ultrafast lasers*. Available from: http://www.coherent.com/products/?1620/Talisker-Family-of-Fiber-Based-Lasers.

94.   Kuang, Z., et al. *Multiple beam ultrashort pulse laser microprocessing*. 2010.

95.   Alemohammad, H. and E. Toyserkani, *Laser-assisted additive fabrication of micro-sized coatings*. Advances in Laser Materials Processing: Technology, Research and Applications, ed. J.P.J.L.D.K.Y.T.E. Lawerence2010. 735-762.

96.   Barron, J.A., et al., *Application of laser printing to mammalian cells.* Thin solid films, 2004. **453**: p. 383-387.

97.   Biswas, A., et al., *Laser surface treatment of Ti-6Al-4V for bio-implant application.* Lasers in Engineering, 2007. **17**(1-2): p. 59-73.

98.   Bonss, S.S., M; Brenner, B; Beyer, E. *Precise hardening with high power diode lasers using beam shaping mirror optics*. in *High-Power Diode Laser Technology and Applications, Proceedings of the SPIE*. 2003. SPIE.

99.   Lee, J., et al., *Application of Nano-Pulsed Nd:YAG Laser to Crystallization of Amorphous Si Thin Films for Next Generation Flat-panel Display.* International Journal of Precision Engineering and Manufacturing, 2012. **13**(4): p. 587-591.

100.   Melissinaki, V., et al., *Direct laser writing of 3D scaffolds for neural tissue engineering applications.* Biofabrication, 2011. **3**(4).

101.   Pique, A., et al., *Laser processing of polymer thin films for chemical sensor applications.* Surface & Coatings Technology, 2003. **163**: p. 293-299.

102.   Pique, A., et al., *Applications of laser direct-write for embedding microelectronics - art. no. 66060R*, in *Advanced Laser Technologies 2006*, D.C.D.M.K.V.I. Dumitras, Editor 2007. p. R6060-R6060.

103.   Triantafyllidis, D., L. Li, and F.H. Stott, *Investigation of the effects of nonconventional beam geometries in laser surface treatment of ceramics: Theoretical analysis.* Journal of Laser Applications, 2006. **18**(2): p. 161-168.

104.   Leung, M.K.H., H.C. Man, and J.K. Yu, *Theoretical and experimental studies on laser transformation hardening of steel by customized beam.* International Journal of Heat and Mass Transfer, 2007. **50**(23-24): p. 4600-4606.

105.   Farson, D.F., et al., *Femtosecond laser bulk micromachining of microfluid channels in poly(methylmethacrylate).* Journal of Laser Applications, 2006. **18**(3): p. 210-215.

106.   Miller, T.M., et al., *Fabrication of a micro-scale, indium-tin-oxide thin film strain-sensor by pulsed laser deposition and focused ion beam machining.* Sensors and Actuators, A: Physical, 2003. **104**(2): p. 162-170.

107.   Kuang, Z., et al., *Diffractive multi-beam ultra-fast laser micro-processing using a spatial light modulator.* Zhongguo Jiguang/Chinese Journal of Lasers, 2009. **36**(12): p. 3093-3115.

108.   Cheng, J., et al., *Single-pulse drilling study on Au, Al and Ti alloy by using a picosecond laser.* Applied Physics A: Materials Science and Processing, 2009. **95**(3): p. 739-746.

109. Cheng, J., et al., *Ablation mechanism study on metallic materials with a 10 ps laser under high fluence.* Applied Surface Science, 2009. **255**(18): p. 8171-8175.

110. Chrisey, D.B., K.S. Grabowski, and M.S. Osofsky, *Pulsed laser deposition of YBa2Cu3O7-δ in an oxygen background and discharge.* Physica C: Superconductivity and its applications, 1989. **162-164**(PART 1): p. 129-130.

111. Hakola, A., et al., *Ni-Mn-Ga films on Si, GaAs and Ni-Mn-Ga single crystals by pulsed laser deposition.* Applied Surface Science, 2004. **238**(1-4 SPEC. ISS.): p. 155-158.

112. Eisenhawer, B., et al., *Growth of axial SiGe heterostructures in nanowires using pulsed laser deposition.* Nanotechnology, 2011. **22**(30).

113. Piqué, A., et al., *Growth of organic thin films by the matrix assisted pulsed laser evaporation (MAPLE) technique.* Thin solid films, 1999. **355**: p. 536-541.

114. Piqué, A., et al., *Processing of functional polymers and organic thin films by the matrix-assisted pulsed laser evaporation (MAPLE) technique.* Applied Surface Science, 2002. **186**(1-4): p. 408-415.

115. Riggs, B.C., et al., *Matrix-assisted pulsed laser methods for biofabrication.* Mrs Bulletin, 2011. **36**(12): p. 1043-1050.

116. Piqúe, A., et al., *Laser processing of polymer thin for chemical sensor applications.* Surface and Coatings Technology, 2003. **163-164**: p. 293-299.

117. Lewis, B.R., et al., *Planar laser imaging and modeling of matrix-assisted pulsed-laser evaporation direct write in the bubble regime.* Journal of Applied Physics, 2006. **100**(3).

118. Lin, Y., et al., *BUBBLE FORMATION MODELING IN MATRIX-ASSISTED PULSED-LASER EVAPORATION DIRECT WRITE.* Msec 2008: Proceedings of the Asme International Manufacturing Science and Engineering Conference 2008, Vol 22009. 497-504.

119. Lin, Y., Y. Huang, and D.B. Chrisey, *Droplet formation in matrix-assisted pulsed-laser evaporation direct writing of glycerol-water solution.* Journal of Applied Physics, 2009. **105**(9).

120. Pique, A., *The Matrix-Assisted Pulsed Laser Evaporation (MAPLE) process: origins and future directions.* Applied Physics a-Materials Science & Processing, 2011. **105**(3): p. 517-528.

121. Schultze, V. and M. Wagner, *Laser-induced forward transfer of aluminium.* Applied Surface Science, 1991. **52**(4): p. 303-309.

122. Hon, K.K.B., L. Li, and I.M. Hutchings, *Direct writing technology-Advances and developments.* CIRP Annals - Manufacturing Technology, 2008. **57**(2): p. 601-620.

123. Yamada, H., *optimisation of laser-induced forward transfer process of metal thin films.* Applied surface science.

124. Zergioti, I., et al., *Microdeposition of metal and oxide structures using ultrashort laser pulses.* Applied Physics A: Materials Science and Processing, 1998. **66**(5): p. 579-582.

125. Baron, J.A., *Biological Laser Printing: a novel technique for creating Hetrogeneous 3-Dimensional Cell Patterns.* Biomedical Microdevices.

126. Chen, S.H. and F.H. Liu, *Ceramic prototype fabrication using selective laser sintering.* Hsi-An Chiao Tung Ta Hsueh/Journal of Xi'an Jiaotong University, 2011. **45**(11): p. 116-120.

127. Liu, B., P. Bai, and Y. Li, *Post treatment process and selective laser sintering mechanism of polymer-coated mo powder.* Open Materials Science Journal, 2011. **5**: p. 194-198.

128. Song, B., et al., *Process parameter selection for selective laser melting of Ti6Al4V based on temperature distribution simulation and experimental sintering.* International Journal of Advanced Manufacturing Technology, 2011: p. 1-8.

129. Sundaram, R. and J. Choi, *A slicing procedure for 5-axis laseraided DMD process.* Journal of Manufacturing Science and Engineering, Transactions of the ASME, 2004. **126**(3): p. 632-636.

130. Delgado, J., J. Ciurana, and C.A. Rodriguez, *Influence of process parameters on part quality and mechanical properties for DMLS and SLM with iron-based materials.* International Journal of Advanced Manufacturing Technology, 2012. **60**(5-8): p. 601-610.

131. Sato, T., *Laser Assisted Ink Consolidation for Direct Write component Fabrication*, in *Laser Group*2011, university of Liverpool.

132.   Fearon, E., T. Sato, and D. Wellburn. *Thermal effects of substrate materials used in the laser curing of particulate silver inks*. in *Proceedings of the LANE* 2007. Erlangen, Germany.

133.   Mao, Q., L. Bian, and M. Huang, *Study of the visible light curing of vinyl ester resins using in situ Raman spectroscopy.* Journal of Polymer Research, 2011. **18**(6): p. 1751-1756.

134.   Souza-Junior, E.J., et al., *The effect of curing light and chemical catalyst on the degree of conversion of two dual cured resin luting cements.* Lasers in Medical Science, 2012. **27**(1): p. 145-151.

135.   Cao, Y., et al., *High-photosensitive resin for super-resolution direct-laser-writing based on photoinhibited polymerization.* Optics Express, 2011. **19**(20): p. 19486-19494.

136.   Kim, Y.-O., et al., *Diode-pumped solid-state laser for bonding orthodontic brackets: effect of light intensity and light-curing time.* Lasers in Medical Science, 2011. **26**(5): p. 585-589.

137.   Shin, D.-H., et al., *Influence of DPSS Laser on Polymerization Shrinkage and Mass Change of Resin Composites.* Photomedicine and Laser Surgery, 2011. **29**(8): p. 545-550.

138.   Mirsasaani, S.S., M.M. Atai, and M.M. Hasani-Sadrabadi, *Photopolymerization of a dental nanocomposite as restorative material using the argon laser.* Lasers in Medical Science, 2011. **26**(5): p. 553-561.

139.   Shahbazi, J., et al., *Sutureless Sealing of Penetrating Corneal Wounds Using a Laser-Activated Thin Film Adhesive.* Lasers in Surgery and Medicine, 2011. **43**(6): p. 490-498.

140.   Mori, A., et al., *Formation of micro lens by laser polymerization.* Electronics and Communications in Japan, 2012. **95**(2): p. 59-67.

141.   Holbrook, K.A., O. G.A, and S. C.J, *CO2 Laser-Induced Deposition.* International Journal of Chemical Kinetics, 1993. **25**(4).

142.   Panitz, M., H. D.C, and S. T, *The opportunities and challenges associated with wireless interconnects in aircraft.* Journal of Aerospace Engineering, 2010. **224**(4): p. 459-470.

143.   Anthony, K., D.-H.O. Amert, and a.N.-S. Kim, *A simulation and experimental study on packing of nanoinks to attain better conductivity.* Journal of Applied Physics. **108**(10).

144.   Tai, Y.-L. and Z.-G. Yang, *Preparation of stable aqueous conductive ink with silver nanoflakes and its application on paper-based flexible electronics.* Surface and Interface Analysis, 2012. **44**(5): p. 529-534.

145.   Jung, I., et al., *A Simple Process for Synthesis of Ag Nanoparticles and Sintering of Conductive Ink for Use in Printed Electronics.* Journal of Electronic Materials, 2012. **41**(1): p. 115-121.

146.   Khan, A., et al., *Direct printing of copper conductive micro-tracks by multi-nozzle electrohydrodynamic inkjet printing process.* Journal of Materials Processing Technology, 2012. **212**(3): p. 700-706.

147.   Das, A., et al., *Superoleophobic and conductive carbon nanofiber/fluoropolymer composite films.* Carbon, 2012. **50**(3): p. 1346-1354.

148.   Kim, Y., et al., *Use of copper ink for fabricating conductive electrodes and RFID antenna tags by screen printing.* Current Applied Physics, 2012. **12**(2): p. 473-478.

149.   Jo, Y.H., et al., *Synthesis and characterization of highly conductive Sn-Ag bimetallic nanoparticles for printed electronics.* Journal of Nanoparticle Research, 2012. **14**(4).

150.   Lee, H.M., et al., *A Novel Solution-Stamping Process for Preparation of a Highly Conductive Aluminum Thin Film.* Advanced Materials, 2011. **23**(46): p. 5524-+.

151.   Tobjork, D., et al., *IR-sintering of ink-jet printed metal-nanoparticles on paper.* Thin solid films, 2012. **520**(7): p. 2949-2955.

152.   Roberson, D.A., R.B. Wicker, and E. MacDonald, *Microstructural characterization of electrically failed conductive traces printed from Ag nanoparticle inks.* Materials Letters, 2012. **76**: p. 51-54.

153.   Kar, A. and M.D. Langlais, *Optothermal effects of laser modes in laser materials processing.* Optical and Quantum Electronics, 1995. **27**(12): p. 1165-1180.

154.   Sharp, M.C., *Mathematical Modelling of Continuous Wave CO2 Laser Processing of Materials*, 1986, University of London: London.

155. Cole, C.E.N., S.C; Tyrer, *The Application of Diffractive Optical Elements in High Power Laser Material Processing*, in *17th ICALEO*1998, Laser Institute of America: Orlando,FL.

156. Gibson, M.T.J.H., R, *Novel Computer Generated Diffractive Optics Modifying Beam Characteristics To Improve The Microstructures Of Directly Deposited Inconel*, in *27th ICALEO*2008, Laser Institute of America: Temecula, CA.

157. Kell, J.T., J; Higginson, R; Thomson, R; Jones, J; Noden, S, *Holographic Diffractive Optical Elements Allow Improvements In Conduction Laser Welding Of Steels*, in *25th ICALEO*2006, Laser Institute of America.

158. Victor, B.R., S; Walters, C. T, *Custom Beam Shaping For High-Power Fiber Laser Welding*, in *27th ICALEO*2008, Laser Institute of America: Temecula, CA.

159. Bitterli, R.e.a., *Refractive Statistical Concave 1D Diffusers for Laser Beam Shaping*, in *Laser Beam Shaping IX*2008, SPIE.

160. Forbes, A.L., C. S; Litvina, I; Loveday, P. W; Belyi, V and Kazak, N. S, *Variable flattened Gaussian beam order selection by dynamic control of an intracavity diffractive mirror*, in *Laser Beam Shaping IX, Proceedings of SPIE* 2008, SPIE.

161. Herrit, G.H., A; Reedy, H, *Novel Focusing Optics For IR Lasers*, in *24th ICALEO*2005, Laser Institute of America.

162. Miyamoto, I.M., H, *Novel Laser Beam Shaping Optics: LSV Optics Applications to Transformation Hardening and Ceramic Joining*, in *11th ICALEO*1992, Laser Institute of America.

163. Steen, W.M., *Laser Material Processing*. 3rd ed2003, London: Springer-Verlag.

164. Zeng, D., W.P. Latham, and A. Kar, *Shaping of annular laser intensity profiles and their thermal effects for optical trepanning*, 2006.

165. Crafer, R.C.O., P. J, *Heat Treatment of Workpiece by Laser*, E.P. Office, Editor 1982: EU EP 0062 517.

166. Almarzouk, K., *Generation of a Uniform Line Source Using a Binary Filter.* Optics Communications, 1980. **35**(2): p. 161-163.

167. Simmons, W.W., Leppelme.Gw, and B.C. Johnson, *Optical Beam Shaping Devices Using Polarization Effects.* Applied Optics, 1974. **13**(7): p. 1629-1632.

168. Belvaux, Y. and S.P.S. Virdi, *Method For Obtaining A Uniform Non-Gaussian Laser Illumination.* Optics Communications, 1975. **15**(2): p. 193-195.

169. Friis-Pedersen, H., H. L.P, and S. B.K, *Online near-infrared measurements of an epoxy cure process compared to mathematical modeling based on differential scanning calorimetry measurements.* Journal of Applied Polymer Science, 2008. **110**(4): p. 2184-2194.

170. TM, L., I. A.I, and K. J, *A cure kinetics model for the non-isothermal curing of polyimide*, in *Technical Papers, Regional Technical Conference - Society of Plastics Engineers*2008: Milwaukee, WI. p. 1930-1934.

171. Rahiotis, C., et al., *Curing efficiency of various types of light-curing units.* 2004. **112**(1): p. 89-94.

172. Christensen, R., P. T.M, and P. B.J, *Resin polymerization problems--are they caused by resin curing lights, resin formulations, or both?*, in *Compendium of continuing education in dentistry*, N.J. Jamesburg, Editor 1995. p. S42-54.

173. Leonard, D., C. D.G, and R. H.W, *Polymerization efficiency of LED curing lights.* Journal of Esthetic and Restorative Dentistry, 2002. **14**(5): p. 286-295.

174. Powell, G., A. J.R, and B. R.J, *Laser and curing light induced in vitro pulpal temperature changes.* Journal of Clinical Laser Medicine and Surgery, 1999. **17**(1): p. 3-5.

175. Semiatin, S.L., et al., *The role of modeling in the development of advanced processes for metallic aerospace alloys.* Metals and Materials International, 2004. **10**(6): p. 589-603.

176. Yilbas, B.S., S.S. Akhtar, and C. Karatas, *Laser surface treatment of Inconel 718 alloy: Thermal stress analysis.* Optics and Lasers in Engineering, 2010. **48**(7-8): p. 740-749.

177. Yilbas, B.S., A.F.M. Arif, and C. Karatas, *Laser treatment of silicon at nitrogen ambient: thermal stress analysis.* Surface Engineering, 2011. **27**(6): p. 436-444.

178. Yilbas, B.S., et al., *Laser treatment of aluminum surface: Analysis of thermal stress field in the irradiated region.* Journal of Materials Processing Technology, 2009. **209**(1): p. 77-88.

179. Makun, et al., *The three dimensions reconstruction of laser heat treatment temperature field*, in *High-Power Lasers and Applications Iii*, D.U.K.I.L.J. Fan, Editor 2004. p. 192-198.

180. Galantucci, L.M., L. Tricario, and Cirp, *An experimental and numerical study on the influence of not uniform beam energy distribution in laser steel hardening.* Cirp Annals 1999 - Manufacturing Technology1999. 155-158.

181. Ben Rhima, A., et al., *An idealisation of the residual stresses genesis in heat treatments by a laser moving source.* International Journal of Thermal Sciences, 2003. **42**(8): p. 759-776.

182. Bessrour, J., et al., *Heat transient model for surface treatment by a moving laser source.* International Journal of Thermal Sciences, 2002. **41**(11): p. 1055-1066.

183. Antonov, V. and I. Iordanova, *Development and application of analytical and numerical models for characterization of thermal fields during surface laser treatment*, in *15th International School on Quantum Electronics: Laser Physics and Applications*, T.T.E.B.E.S.A. Dreischuh, Editor 2008.

184. Arif, A.F.M. and B.S. Yilbas, *Laser melting of HVOF coating: effect of base material on residual stress formation.* Surface Engineering, 2009. **25**(3): p. 249-256.

185. Deng, D. and S. Kiyoshima, *Numerical simulation of residual stresses induced by laser beam welding in a SUS316 stainless steel pipe with considering initial residual stress influences.* Nuclear Engineering and Design, 2010. **240**(4): p. 688-696.

186. Hofman, J.T., et al., *FEM modeling and experimental verification for dilution control in laser cladding.* Journal of Materials Processing Technology, 2011. **211**(2): p. 187-196.

187. Rossia, F., et al., *Temperature control during diode laser welding in a human cornea - art. no. 663215*, in *Therapeutic Laser Applications and Laser-Tissue Interaction III*, A. Vogel, Editor 2007. p. 63215-63215.

188. Exner, H. and U. Loschner, *Contactless laser bending of silicon nucrostructures*, in *Smart Sensors, Actuators, and Mems, Pts 1 and 2*, J.C.V.V.K.C.C. Chiao, Editor 2003. p. 383-392.

189. Loschner, U. and H. Exner, *FEM calculations on laser bending of silicon with a moving laser source*, in *Mems, Moems, and Micromachining*, H.E.A. Urey, Editor 2004. p. 407-414.

190. Carey, C., et al., *Towards a rapid, non-contact shaping method for fibre metal laminates using a laser source.* International Journal of Advanced Manufacturing Technology, 2010. **47**(5-8): p. 557-565.

191. Edwardson, S.P., et al., *Geometrical influences on multi-pass laser forming.* Journal of Physics D-Applied Physics, 2006. **39**(2): p. 382-389.

192. Edwardson, S.P., et al., *Towards Controlled Three-Dimensional Laser Forming.* Lasers in Engineering, 2012. **22**(5-6): p. 393-399.

193. Edwardson, S.P., et al., *Temperature Gradient Mechanism: Overview of the Multiple Pass Controlling Factors*, in *Laser Assisted Net Shape Engineering 6, Proceedings of the Lane 2010, Part 1*, M.V.F.G.M. Schmidt, Editor 2010. p. 53-63.

194. Edwardson, S.P., et al., *Laser forming: overview of the controlling factors in the temperature gradient mechanism.* Proceedings of the Institution of Mechanical Engineers Part C-Journal of Mechanical Engineering Science, 2010. **224**(C5): p. 1031-1040.

195. Griffiths, J., et al., *Finite Element Modelling of Laser Forming at Macro and Micro Scales*, in *Laser Assisted Net Shape Engineering 6, Proceedings of the Lane 2010, Part 2*, M.V.F.G.M. Schmidt, Editor 2010. p. 371-380.

196. Anon. *From rapid prototyping to rapid manufacturing*. in *Design engineering London*. 1994.

197. Anon, *Laser-base methods speed up modelmaking.* Advanced Materials and Processes, 1990. **138**(1): p. 51-53.

198. Jacob Fish, T.B., *A First Course in Finite Elements*. Vol. 1. 2007: Wiley.

199.   R.Buchanan, G., *Finite Element Analysis*1995: Mcgraw Hill.

200.   O.C.Zienkiewicz, *The Finite Element Method Its Basis & Fundamentals*. Vol. 1. 2008: Elsevier.

201.   Burman, E. and A. Ern, *IMPLICIT-EXPLICIT RUNGE-KUTTA SCHEMES AND FINITE ELEMENTS WITH SYMMETRIC STABILIZATION FOR ADVECTION-DIFFUSION EQUATIONS.* Esaim-Mathematical Modelling and Numerical Analysis-Modelisation Mathematique Et Analyse Numerique, 2012. **46**(4): p. 681-707.

202.   Bournaveas, N. and G.E. Zouraris, *THEORY AND NUMERICAL APPROXIMATIONS FOR A NONLINEAR 1+1 DIRAC SYSTEM.* Esaim-Mathematical Modelling and Numerical Analysis-Modelisation Mathematique Et Analyse Numerique, 2012. **46**(4): p. 841-874.

203.   Juarez, G. and A.G. Ayala, *Finite element variational formulation for beams with discontinuities.* Finite Elements in Analysis and Design, 2012. **54**: p. 37-47.

204.   Wei, D. and Y. Liu, *Analytic and finite element solutions of the power-law Euler-Bernoulli beams.* Finite Elements in Analysis and Design, 2012. **52**: p. 31-40.

205.   Zeng, G., et al., *The Finite Difference Methods and Their Extrapolation for Solving Biharmonic Equations.* Journal of Computational Analysis and Applications, 2012. **14**(6): p. 1038-1048.

206.   Wu, X.-H., et al., *An analysis of the convection-diffusion problems using meshless and meshbased methods.* Engineering Analysis with Boundary Elements, 2012. **36**(6): p. 1040-1048.

207.   Yoon, G.H., *Toward a multifrequency quasi-static Ritz vector method for frequency-dependent acoustic system application.* International Journal for Numerical Methods in Engineering, 2012. **89**(11): p. 1451-1470.

208.   Kaveh, A. and M.J.T. Kian, *Efficient finite element analysis using graph-theoretical force method with brick elements.* Finite Elements in Analysis and Design, 2012. **54**: p. 1-15.

209.   Johnson, C., *Numerical Solution of Partial Differential Equations by the Finite Element Method*2009: Dover.

210.   Yaakoubi, M., M. Kchaou, and F. Dammak, *Simulation of the thermomechanical and metallurgical behavior of steels by using ABAQUS software.* Computational Materials Science, 2013. **68**: p. 297-306.

211.   Shukla, P.P. and J. Lawrence, *Examination of temperature distribution and the thermal effects on Si3N4 engineering ceramics during fibre laser surface treatment.* Optics and Lasers in Engineering, 2011. **49**(7): p. 998-1011.

212.   Postacioglu, N., P. Kapadia, and J. Dowden, *A Mathematical-Model of Heat-Conduction in a Prolate Spheroidal Coordinate System with Applications to the Theory of Welding.* Journal of Physics D-Applied Physics, 1993. **26**(4): p. 563-573.

213.   Robert, A. and T. Debroy, *Geometry of laser spot welds from dimensionless numbers.* Metallurgical and Materials Transactions B-Process Metallurgy and Materials Processing Science, 2001. **32**(5): p. 941-947.

214.   Rosenthal, D., *Mathematical theory of heat distribution during welding and cutting.* Weld J, 1941. **20**(5): p. 220-234.

215.   Carslaw, H.J., J, *Conduction of Heat in Solids*. 2nd ed1959, Oxford.

216.   Eagar, T.W.a.T., N. S, *Temperature fields produced by traveling distributed heat sources.* Welding Journal, 1983. **62**(12): p. 346-355.

217.   GEM. *Comopany web page*. [http://www.gwent.org/gem_index.html].

218.   website,   J.c. [http://www.janomeie.com/main_content.asp?sitename=janome&pagename=home].

219.   Wellburn, D., *LASER BEAM INTENSITY PROFILE MODULATOR*, 2011: GB.

220.   technology, C. *Web page*. [http://www.cybamantech.co.uk/cybaman].

221.   Rofin.   *Company   web   page*. [http://www.rofin.com/en/products/co2_lasers/sealed_off_co2_laser/sc_series/?PHPSESSID=d70b2a79bfd1fdfcd887bbc7fb94975d].

222.   Aerotech, *company web page*.

223. Optics, U. *company webpage*. Available from: http://ulooptics.com/.

224. CINOGY. *Web Page*. [http://www.cinogy.com/html/co2-beam_profiler_laserdec.html].

225. ASTM, *Standard Test Method for Film Hardness by Pencil Test*, in *D3363 - 05(2011)e1*.

226. Company, F.M. *company web page*. Available from: http://www.ferro.com/.

227. Chemicals, C. *company web page*. Available from: www.columbianchemicals.com.

228. TIMCAL. *company web page*. Available from: http://www.timcal.com/scopi/group/timcal/timcal.nsf/pagesref/SCMM-7EVDQL?OpenDocument&Lang=en.

229. Resin, K. *company product data sheet*. Available from: http://www.kianresin.com/TDS/Resins/EPIKOTE1001.pdf.

230. company, D.C. *company web page*. Available from: www.dow.com.

231. Collins, S., *Differential Scanning Calorimetry*.

232. Shen, J., et al., *Synthesis and thermal properties of poly(methyl methacrylate)-poly(L-lactic acid)-poly(methyl methacrylate) tri-block copolymer.* Journal of Applied Polymer Science, 2012. **124**(5): p. 3905-3911.

233. Morancho, J.M., et al., *Thermal analysis of enhanced poly(vinyl alcohol)-based proton-conducting membranes crosslinked with sulfonation agents for direct methanol fuel cells.* Journal of Applied Polymer Science, 2012. **124**: p. E57-E65.

234. Jayasuriya, M.M. and D.J. Hourston, *The effect of composition and the level of crosslinking of the poly(methylmethacrylate) phase on the properties of natural rubber-poly(methylmethacrylate) semi-2 interpenetrating polymer networks.* Journal of Applied Polymer Science, 2012. **124**(5): p. 3558-3564.

235. Kartal, S., M.S. Aday, and C. Caner, *Use of microperforated films and oxygen scavengers to maintain storage stability of fresh strawberries.* Postharvest Biology and Technology, 2012. **71**: p. 32-40.

236. Duan, J., et al., *Determination of 27 chemical constituents in Chinese southwest tobacco by FT-NIR spectroscopy.* Industrial Crops and Products, 2012. **40**: p. 21-26.

237. Niu, X., et al., *A feasibility study on quantitative analysis of glucose and fructose in lotus root powder by FT-NIR spectroscopy and chemometrics.* Food Chemistry, 2012. **133**(2): p. 592-597.

238. Jiang, H., et al., *Rapid determination of pH in solid-state fermentation of wheat straw by FT-NIR spectroscopy and efficient wavelengths selection.* Analytical and bioanalytical chemistry, 2012. **404**(2): p. 603-11.

7. Appendix

This appendix briefly discusses the principles of using Finite Element Methods to solve partial differential equations. The generalised forms of 2nd order PDEs are firstly discussed; FEM for 2nd order PDE is then demonstrated in 1D, 2D and 3D cases respectively; Generalised concepts of Variational Form and Hilbert Space are then applied and explained; This chapter finally discusses how to use FEM to solve the time dependent problem involved in this study.

7.1 Types of partial differential equations

The most general second order partial differential equation can be written as

$$A(q_1, q_2)\frac{\partial^2 f}{\partial q_1^2} + B(q_1, q_2)\frac{\partial^2 f}{\partial q_1 \partial q_2} + C(q_1, q_2)\frac{\partial^2 f}{\partial q_2^2} = g\left(\frac{\partial f}{\partial q_1}, \frac{\partial f}{\partial q_2}, q_1, q_2\right) \qquad (7.1\text{---}1)$$

where A, B and C are known functions of the coordinates. The function g can also depend on derivatives of lesser order. Notice that equation (7.1---1) has a similar structure to the quadratic equation,

$$ax^2 + bxy + cy^2 = d \qquad (7.1\text{---}2)$$

Solutions of this equation fall into three classes, depending on the relationships between a, b, and c. When $b^2 < 4ac$, the equation describes an ellipse; $b^2 > 4ac$ describes a hyperbola. A special case arises when $b^2 = 4ac$. In this case, the resulting shape is a parabola.

Using the classification of the quadratic equation as a guide, we can break partial differential equations into three groups, elliptical, parabolic and hyperbolic. Specifically: **a PDE is elliptical if $B^2(q_1, q_2) < 4A(q_1, q_2)C(q_1, q_2)$, parabolic if $B^2(q_1, q_2) = 4A(q_1, q_2)C(q_1, q_2)$, and hyperbolic if $B^2(q_1, q_2) > 4A(q_1, q_2)C(q_1, q_2)$.**

The stationary heat equation is an elliptic problem and the time dependent heat equation is a parabolic problem.

In this chapter the stationary heat conduction problem (Poisson equation) is used to demonstrate the concepts of FEM. Then account is extended to parabolic problems with time dependence.

7.2. Solving one-dimensional problem with FEM

This section firstly explains why FEM is used for solving PDE problems by proving the equivalence between the classical boundary value problem, the minimisation problem and the variational problem.

7.2.1 Variational formulation for one-dimensional problems

It is not always possible to solve a differential equation in its *classical form*, while a systematic method for solution exists if the problem is converted into one of its variational equivalencies.

Let us first consider the classical one dimensional two point boundary condition problem (D1) as an example.

(D1) $-u''(x) = f(x)$ for 0<x<1,   (7.2.1---1)

                $u(0) = u(1) = 0$ (7.2.1---2)

where u$\emptyset\emptyset$ is the second derivative of u with respect to x.

Equation (7.2.1---1) may represent many different kinds of physics: (D1) may describe the motion of an elastic cord subjected to load f and has displacement u; alternatively it may represent one-dimensional heat conduction with heat source f and temperature u; or even the probability wave generated by a particle confined in an infinite õQuantum Wellö. Regardless to the different physical meanings, numerically the problem is unchanged and one can find the solutions with the same method.

(D1) can be easily solved by integration. However we are going to demonstrate how to use the variational formulation of (D1), and extend to complicated situations where analytical methods become inapplicable in later sections.

Firstly, we introduce the notation $(v, w) = \int_0^1 v(x)w(x)dx$ (7.2.1---3)

We now define a linear space V such that

  V= {v: v is a continuous function on [0,1], v$\emptyset$ is continuous and bounded on [0,1], and v(0)=v(1)=0}   (7.2.1---4)

V is by definition an infinite set of continuous functions defined on [0,1], matching the domain and boundary conditions of (D1). It is easy to see that any solution of (D1) u must be a member of V.

A mapping operation F is a *functional* of V if

$\quad$ F: V $\quad$ R $\quad$ ie, $F(v) \in R$ $\hspace{6cm}$ (7.2.1---5)

$$F(v) = \frac{1}{2}(v',v') - (f,v) \hspace{5cm} (7.2.1\text{---}6)$$

Now we have a *minimisation problem* (M1) and *variational problem* (V1):

(M1) $\quad$ find $u \in V$ such that $F(u) \le F(v) \quad \forall v \in V$ $\hspace{3cm}$ (7.2.1---7)

(V1) $\quad$ find $u \in V$ such that $(u',v') = (f,v) \quad \forall v \in V$ $\hspace{2.5cm}$ (7.2.1---8)

The problem (M1) and (V1) are variational formulations of problem (D1).

It can be proven that the classical boundary value problem (D1), minimisation problem (M1) and variational problem (V1) are essentially equivalent, ie,

$(D1) \Leftrightarrow (V1) \Leftrightarrow (M1)$ $\hspace{6cm}$ (7.2.1---9)

$\quad$ Thus we can solve (D1) by seeking a solution for (V1) or (M1).

To prove (7.2.1---9):

1) Let us first show that a solution of (D1) is also a solution of (V1). To see this, multiply the equation (7.2.1---1) by an arbitrary test function $v \in V$ and integrate over (0,1) which gives

$\quad -(u'',v) - (f,v)$ $\hspace{6cm}$ (7.2.1---10)

Now integrate the left hand side by parts and have

$\quad (u'',v) = \quad u'(1)v(1) \mid u'(0)v(0) \mid (u',v') = (u',v')$ $\hspace{2cm}$ (7.2.1---11)

And we can thus conclude

$(u',v') = (f,v) \quad \forall v \in V$ $\hspace{6cm}$ (7.2.1---12)

Therefore u is a solution of (V1) and $(D1) \rightarrow (V1)$ $\hspace{3cm}$ (7.2.1---13)

2) Next it is shown that (V1) and (M1) have the same solutions.

Suppose that u is a solution of (V1), and for $v \in V$ set $w - v - u$ and $w \in V$

Then

$$F(v) = F(u + w) = \frac{1}{2}(u' + w', u' + w') - (f, u + w) = \frac{1}{2}(u', u') - (f, u) +$$
$$(u', w') - (f, w) + \frac{1}{2}(w', w') = F(u) + [(u', w') - (f, w)] + \frac{1}{2}(w', w') \geq F(u)$$

$$(7.2.1\text{---}14)$$

And this shows u is also a solution of (M1) and hence $(V1) \rightarrow (M1)$ $\quad\quad (7.2.1\text{---}15)$

3) Now it is shown that a solution of (M1) is also a solution of (V1)

If u satisfies (M1) then

$$F(u) \leq F(u + \varepsilon v) \quad \forall v \in V \text{ and } \varepsilon \in R \quad\quad (7.2.1\text{---}16)$$

$$F(u + \varepsilon v) = \frac{1}{2}(u', u') + \varepsilon(u', v') + \frac{\varepsilon^2}{2}(v', v') - (f, u) - \varepsilon(f, v) \quad\quad (7.2.1\text{---}17)$$

since (7.2.1---16) holds, then $\frac{\partial F(u + \varepsilon v)}{\partial \varepsilon} = 0 \text{ at } \varepsilon = 0$ $\quad\quad (7.2.1\text{---}18)$

And $(u', v') - (f, v) = 0$ and therefore $(M1) \rightarrow (V1)$ $\quad\quad (7.2.1\text{---}19)$

4) Finally, it is shown how a solution of (V1) also satisfies (D1)

(V1) suggests that $\int_0^1 u' v' dx - \int_0^1 f v \, dx = 0 \quad \forall v \in V$ $\quad\quad (7.2.1\text{---}20)$

Integrating the first term by parts we have

$$-\int_0^1 (u'' + f) v dx = 0 \quad \forall v \in V \quad\quad (7.2.1\text{---}21)$$

and this means that $u'' + f = 0$, ie, $(V1) \rightarrow (D1)$ $\quad\quad (7.2.1\text{---}22)$

Now it can be concluded that $(D1) \leftrightarrow (V1) \leftrightarrow (M1)$ and one can seek a solution of the variational formulations (V1) and (M1) to solve the classical problem (D1).

7.2.2 Discretisation of variational formulations

Now define a finite dimensional subspace V_h of the space V described by equation (7.2.1---4). Let partition $I_j = (x_j, x_{j-1})$ divide [0,1] into $0 = x_0 Ö x_1 Ö x_2 Ö \ Ö x_M Ö x_{M+1} = 1$, and set $h = \max(x_j, x_{j-1})$. Then

$V_h = \{v: v$ is linear on each interval of I_j, continuous on [0,1] and $v(0) = v(1) = 0\}$.   (7.2.2---1)

V_h is a subspace of V, ie, $V_h \subset V$. An example of v V_h is shown in Fig 7.1, one can see that the quantity h defines the fineness of this partition.
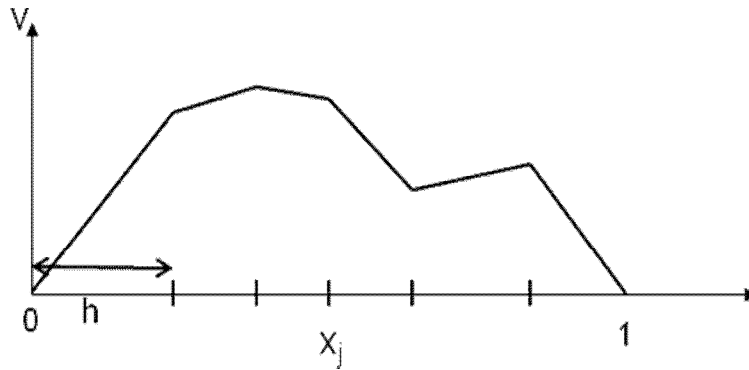
Fig 7.1 A function in the space V_h

Now introduce basis functions $\phi_j(x)$ V_h such that

$$\phi_j(x_i) = \begin{cases} 1 & \text{If i=j} \\ 0 & \text{If i≠j, i,j=1,2,3...M} \end{cases} \qquad (7.2.2\text{---}2)$$

For $x \tilde{N} x_j$ on [0,1], ϕ_j is continous and piecewise linear; in other words, ϕ_j is a set of functions that peak at node x_j with value 1, then linearly decrease to 0 at adjacent nodes, and are equal to 0 everywhere else in the domain, as illustrated in Fig 7.2
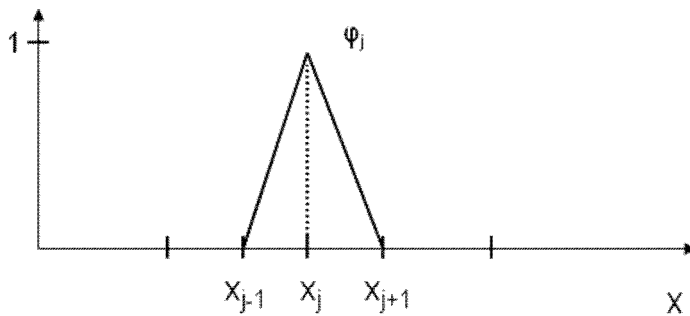

Fig 7.2 A basis function ϕ_j in the space V_h

It is clear that each ϕ_i is linearly independent from each other, hence for any function v V_h have the unique representation

$$v(x) = \sum_1^M \eta_i \phi_i(x) \qquad x\ [0.1] \qquad (7.2.2\text{---}3)$$

where $\phi_i = v(x_i)$ at each node x_i. Each $v \in V_h$ can be written as a linear combination of the functions ϕ_i. This means V_h is a **linear functional space of dimension M** with **basis** $\{\phi_i\}$, and each ϕ_i is a basis function.

The classical boundary problem (D1) can now be formulated as variational forms on V_h

(M_h1) find $u_h \in V_h$ such that $F(u_h) \leq F(v)$ $\forall v \in V_h$ (7.2.2---4)

(V_h1) find $u_h \in V_h$ such that $(u_h', v') = (f, v)$ $\forall v \in V_h$ (7.2.2---5)

7.2.3 Obtaining a solution with Galerkin's method

Obtaining a solution by solving the Problem (V_h1) is usually referred to as the **Galerkin's method** and by solving (M_h1) is usually referred to as the **Ritz's method**. We firstly discuss the Galerkin's method.

 If u_h satisfies (V_h1) then it also holds for

$(u_h', \phi_j') = (f, \phi_j)$ (7.2.3---1)

and $u_h(x)$ can be written in the form

$$u_h(x) = \sum_1^M \varepsilon_i \phi_i(x) \qquad \text{where } \varepsilon_i = u_h(x_i)$$ (7.2.3---2)

By substituting (7.2.3---2) into (7.2.3---1), we have

$$\sum_1^M \varepsilon_i (\phi'_i, \phi'_j) = (f, \phi_j) \qquad j = 1,2,3\text{í } M$$ (7.2.3---4)

The integral (ϕ'_i, ϕ'_j) is essentially in a matrix form, and (f, ϕ_j) is a vector

Therefore equation (7.2.3---4) is a linear system of M equations with M unknowns ε_i, which can be written as

$A\underline{\varepsilon} = \underline{b}$ (7.2.3---5)

where A is a MxM matrix, with each element $a_{ij} = (\phi'_i, \phi'_j)$, $\underline{\varepsilon} = [\varepsilon_i]$ and $\underline{b} = [b_i]$, with $b_i = (f, \phi_i)$, as shown in (7.2.3---6)

$$A = \begin{bmatrix} a_{11} & \cdots & a_{1M} \\ \vdots & \ddots & \vdots \\ a_{M1} & \cdots & a_{MM} \end{bmatrix} \qquad \underline{\varepsilon} = \begin{bmatrix} \varepsilon_1 \\ \vdots \\ \varepsilon_M \end{bmatrix} \qquad \underline{b} = \begin{bmatrix} b_1 \\ \vdots \\ b_M \end{bmatrix} \qquad \text{(7.2.3---6)}$$

The Matrix A and vector $\underline{b}$ are usually referred to as the ***stiffness matrix*** and ***load vector*** respectively. This convention comes from early applications of FEM in structural mechanics.

The integral of the product of two basis functions is non-zero if and only if the basis functions are based on adjacent nodes. This means A is symmetric and most of the elements in A will be zero, and hence A is ***Sparse***.

One can now solve the problem by

$$\underline{\varepsilon} = A^{-1}\underline{b} \qquad \text{(7.2.3---7)}$$

The approximation solution u_h can then be found by substituting _into (7.2.3---2).

7.2.4 An error estimation for FEM

Define the ***norm*** of a function for all   R

$$\|w\| = (w, w)^{1/2} = (\int_0^1 w^2 dx)^{1/2} \qquad \text{(7.2.4---1)}$$

And we then have Theorem (1)

$$|u(x) - u_h(x)| \le h \max|u''| \qquad \text{(7.2.4---2)}$$

Theorem (1) indicates that the error of approximation is directly limited by the discretisation size h since uøø is always bounded; smaller h generally results in smaller errors.
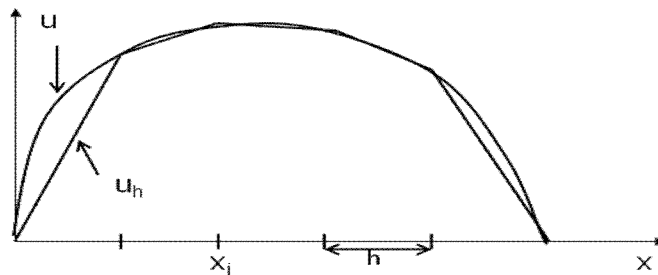

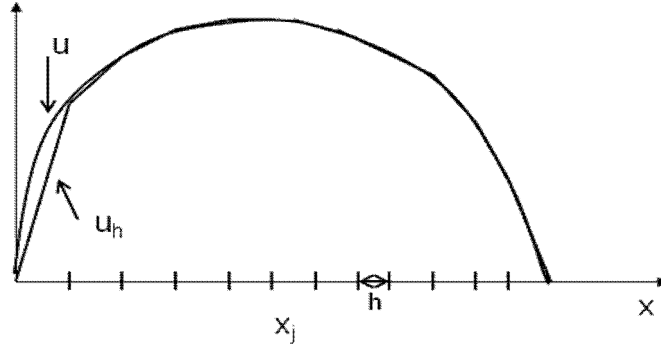Fig 7.3 Error in the case of coarser element discretisation

Fig 7.4 Error in the case of finer element discretisation

To illustrate this, Fig 7.3 and Fig 7.4 show the errors of the same function under different discretisation. In Fig 7.4 the domain is divided into finer elements and the errors are much smaller than that in Fig 7.3. Therefore we can see that the error is limited by the fineness of the discretisation. In practise, the choice of element size is influenced by the variational formulation and accuracy requirements.

7.2.5 The Ritz method for FEM

Now we look at how to solve (D1) by finding a solution for (M$_h$1) using the Ritz method. Recalling the problem

(M_h1) Find $u_h \in V_h$ such that $F(u_h) \le F(v) \quad \forall v \in V_h$ (7.2.2---4)

where $F(v) = \dfrac{1}{2}(v',v') - (f,v)$

Expanding F explicitly we have

$$F = \frac{1}{2}(u',u') + (f,u) = \frac{1}{2}(\sum_i \varepsilon_i \phi_i' + \sum_j \varepsilon_j \phi_j') + (f, \sum_j \varepsilon_j \phi_j)$$
$$= \frac{1}{2}\sum_i \sum_j \varepsilon_j \varepsilon_i \phi_i' \phi_j' + \sum_j \varepsilon_j (f,\phi_j)$$

(7.2.5---1)

The functional F is minimised at the solution u$_h$, and therefore

$$\frac{\partial F}{\partial \varepsilon_j} = \frac{1}{2}\sum_i \varepsilon_i (\phi_i', \phi_j') - (f,\phi_j) = 0$$

(7.2.5---2)

_ can then be solved, and also u_h.

It is a quite interesting fact that the Ritz method named after Walter Ritz, originated from Quantum Mechanics (QM) as a fundamental and extensively used approach to solve the energy equation. The stiffness matrix A is commonly known as the Hamiltonian operator $\hat{H}$ in QM.

For the rest of this chapter only Galerkinøs method will be discussed for solution.

7.3. FEM for elliptical problems in higher dimensions

7.3.1 Poisson problems in 2D and higher dimensions.

Consider the 2D boundary value problem for Poisson equation;

(D2) $-\Delta u = f$ in   (7.3.1---1)

    $u = 0$ on

    where $\Delta = \nabla \cdot \nabla = \dfrac{\partial^2}{\partial x_1{}^2} + \dfrac{\partial^2}{\partial x_2{}^2}$

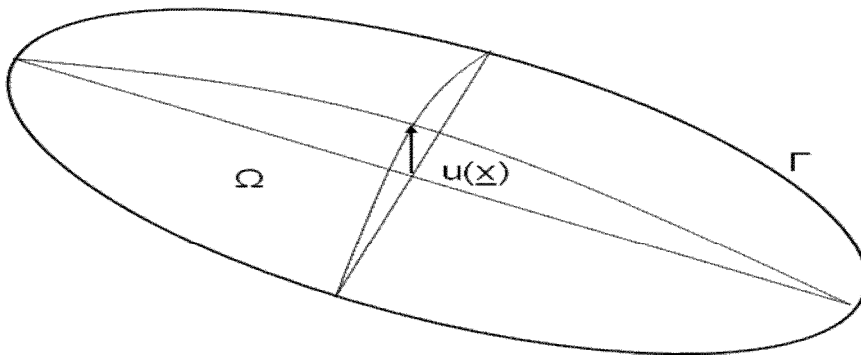The domain and boundary are illustrated in Fig 7.5

Fig 7.5 The Poisson problem in 2D

Now extend the concepts and methods developed for 1D FEM into higher dimensions. Define functional problem space V on the 2D domain   as

---

V={ v: v is continuous on   , $\dfrac{\partial v}{\partial x_1}$ and $\dfrac{\partial v}{\partial x_2}$ are piecewise continuous on   and v=0 on   }

(7.3.1---2)

And the variational problem (V) becomes

 (V2) find u   V such that a(u,v)=(f,v) $\forall\ v\ \in\ V$ (7.3.1---3)

where $a(u,v) = \int\limits_{\Omega} \nabla u \cdot \nabla v dx$ $(f,v) = \int\limits_{\Omega} fv dx$

And the minimisation problem becomes

(M2) find u   V such that F(u)ÖF(v), $\forall\ v\ \in\ V$ (7.3.1---4)

where $F(v) = \dfrac{1}{2}a(v,v) - (f,v)$

The equivalence between (D2), (V2) and (M2) can also be proved analogously to the one-dimensional case using Greenøs theorem.

For the purpose of demonstration, assume   is a polygonal boundary. A triangulation partition (or meshing) of the domain is made by subdividing   into a set T_h =K$_1$, K$_2$, í K$_M$ of non-overlapping triangles, as illustrated in Fig 7.6:

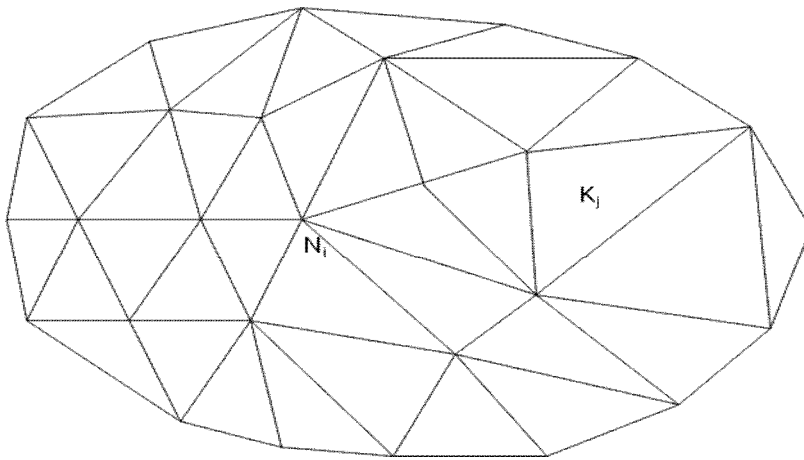$\Omega = \bigcup\limits_{K \in T_h} K = K_1 \cup K_2 \cup \cdots K_M$ (7.3.1---5)

Fig 7.6 Meshing of domain in a 2D problem.

The fineness of the discretisation is determined by h.

 h is h=max diam(K), diam(K) is the largest side of K.

Now define subspace V_h based on the discretisation h as follows:

  V_h={ v: v is continuous on , v is linear on K for K T_h, v=0 on }   (7.3.1---6)

As in the 1D situation, let each intersection point to be a ***node*** N_i.

Unlike the one-dimensional situation, in 2D one has to number the nodes of each element in a systematic way. In general it is accepted to number the nodes in anticlockwise order as illustrated in Fig 7.7
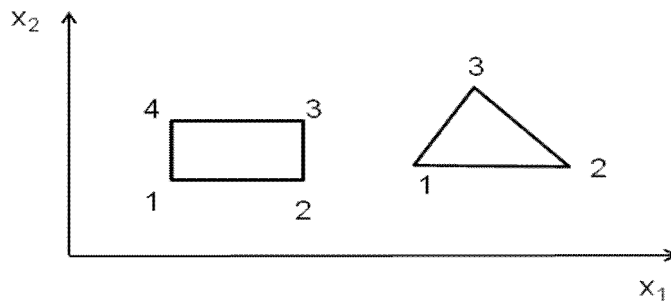

Fig 7.7 Examples of nodes numbering convention.

 The value of any basis function at this node is

$$\phi_j(N_i) = \delta_{ij} = \begin{cases} 1 & \text{If i=j} \\ 0 & \text{If i≠j} \quad \text{i,j =1,2,3...M} \end{cases} \qquad (7.3.1---7)$$

Fig 7.8 illustrates the basis functions. It is important to know that apart from piece-wise linear basis functions, there are also higher order basis functions, as illustrated in Fig 7.9. Different types of basis functions may have relative advantages according to the specific application. However in this work discussion is restricted to the piece-wise linear basis functions and space shown in Fig7.8.
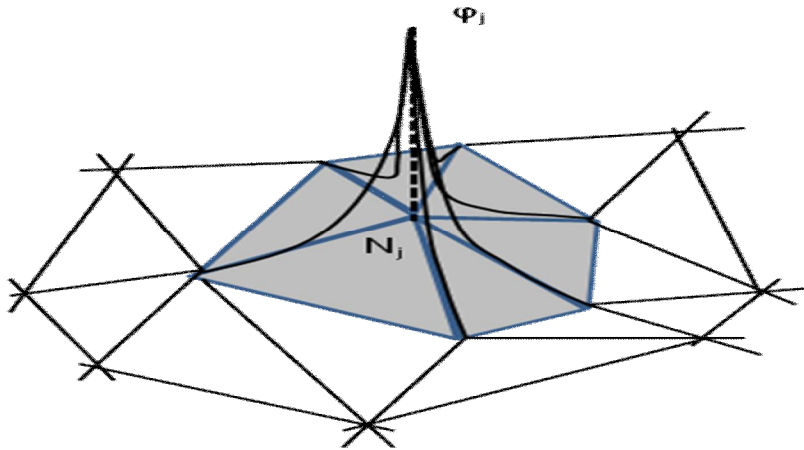
Fig 7.8 A linear basis function in the 2D functional space.

The *support* of φ_j is the region where $\varphi_j \tilde{\neq} 0$. In this case the support consists of triangles with a common node j, as shown with the shaded area in Fig 7.8 and Fig 7.9.
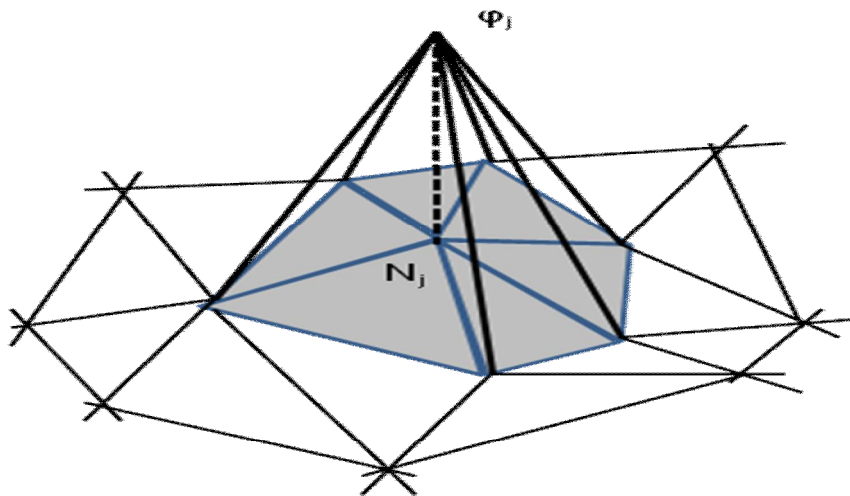

Fig 7.9 A higher order basis function in the 2D functional space.

To find a solution for (7.3.1---3), extend the Galerkin method to 2D.

Firstly, in the space V_h the variational problem (V2) takes the form

$(V_h 2)$ Find u_h such that $(u_h \varnothing, v \varnothing) = (f, v)$ $\forall v \in V_h$ (7.3.1---8)

Express v as

$$v(\underline{x}) = \sum_{1}^{M} \eta_i \phi_i(\underline{x}) \quad \text{where} \quad \eta_i = v(N_i) \text{ for } \underline{x} \tag{7.3.1---9}$$

And by substituting

$$u_h(x) = \sum_{1}^{M} \varepsilon_i \phi_i(x) \quad \text{where} \quad \varepsilon_i = v(N_i) \text{ for } x \tag{7.3.1---10}$$

Into (7.3.1---8), again

$$A\underline{\varepsilon} = \underline{b} \tag{7.2.3---5}$$

where $\underline{\varepsilon} = \{\varepsilon_i\}$, $\underline{b} = \{b_i\}$ and $A = \{a_{ij}\}$

and $a_{ij} = a(\phi_i, \phi_j)$ $\varepsilon_i = u_h(N_i)$, $b_i = (f, \phi_i)$, $a_{ij} = 0$ unless N_i and N_j are nodes of the same triangle, therefore A is again sparse.

One can prove that

$$\|u - u_h\| = \left(\int_{\Omega} (u - u_h)^2 \, dx \right)^{1/2} \leq Ch^2 \tag{7.3.1---11}$$

where C is a constant that depends on the size of the second derivative of u.

The error is limited by the norm $\|u - u_h\|$, which rapidly goes to zero as h tends to zero.

7.3.2 Local stiffness matrix and global stiffness matrix

In the case of a local triangle element K with vertices N_i, N_j and N_k. The *local stiffness matrix* (also referred to as *element matrix*) is

$$a_K = \begin{bmatrix} a_K(\phi_i, \phi_i) & a_K(\phi_i, \phi_j) & a_K(\phi_i, \phi_k) \\ & a_K(\phi_j, \phi_j) & a_K(\phi_j, \phi_k) \\ sym & & a_K(\phi_k, \phi_k) \end{bmatrix} \tag{7.3.2---1}$$

The *global stiffness matrix* A can be constructed by summing up the local stiffness matrices of each element according to

$$a(\phi_i, \phi_j) = \sum_{K \in T_h} a_K(\phi_i, \phi_j) \tag{7.3.2---2}$$

$$b = \sum_{K \in T_h} (f, \phi_j)$$

The equivalence of equation (7.2.3---5) for the global system will take the form

$$\begin{bmatrix} \boxed{a_1} & & & & \\ & \boxed{a_2} & & & \\ & & \boxed{a_{M-1}} & & \\ & & & \boxed{a_M} & \end{bmatrix} \begin{bmatrix} \varepsilon_1 \\ \varepsilon_2 \\ \vdots \\ \varepsilon_M \end{bmatrix} = \begin{bmatrix} b_1 \\ b_2 \\ \vdots \\ b_M \end{bmatrix}$$

(7.3.2---3)

The global stiffness matrix has M×M elements, this means the amount of algebraic calculation increases geometrically for larger M. It has already been shown that for a fixed domain, finer discretisation will generally result less error, in other words, one faces a trade-off relationship between calculation speed and accuracy when implementing discretisation for a FEM calculation.

7.4 Hilbert space and weak formulation

7.4.1 The Hilbert space

It is very useful to work in a space that is slightly larger than the space of piece-wise linear and continuous functions V. It is also very useful to enhance V with various types of scalar products related to the boundary value problems.

Before defining the Hilbert space, consider a few other properties on space.

If V is a linear space, the operation L is a *linear form* on V if and only if

$$L(\beta v + \theta w) = \beta L(v) + \theta L(w) \qquad \forall v, w \in V$$

(7.4.1---1)

Similarly, call a(v,w) a **bilinear form** on VxV, if for all v,w   V, a(v,w) is linear in each argument. That is,

$$a(u, \beta v + \theta w) = \beta a(u,v) + \theta a(u,w) \qquad (7.4.1\text{---}2)$$

$$a(\beta u + \theta v, w) = \beta a(u,w) + \theta a(v,w)$$

Also the bilinear form a is **symmetric** if

$$a(v,w) = a(w,v) \qquad (7.4.1\text{---}3)$$

And a symmetric bilinear form on VxV is said to be a **scalar product** if

$$a(v,v) > 0 \quad \forall v \in V \qquad (7.4.1\text{---}4)$$

The norm associated with this particular scalar product is then denoted as

$$\|v\|_a = (a(v,v))^{1/2} \qquad (7.4.1\text{----}5)$$

A **Hilbert space** is a complete linear space with a scalar product.

7.4.2 The weak formulation:

Now, consider the variational problems in a Hilbert space:

For an interval domain $=R^d$, d=2 or 3, bounded by   , firstly, define a space of õsquare integrable functionsö on   as

$$L_2(\Omega) = \{v : \int_\Omega v^2 dx < \infty\} \qquad (7.4.2\text{---}1)$$

L_2 is the set of functions with finite and integrable squared values

Then the Hilbert space H^1_0 is

$$H^1_0(\ ) = \{v: v \text{ and } \frac{\partial v}{\partial x_i} \text{ belongs to } L_2(\ ), \text{and } v=0 \text{ on } \} \qquad (7.4.2\text{---}2)$$

$$(D3) \quad -\Delta u = f \text{ in} \qquad (7.4.2\text{---}3)$$

$$u = 0 \qquad \text{on}$$

$$(V3) \text{ find } u \quad H^1_0(\ ) \text{ such that } a(u,v)=(f,v) \qquad \forall v \in H^1_0(\Omega) \qquad (7.4.2\text{---}4)$$

(M3) find u $H^1_0(\ )$ such that $F(u) \ddot{O} F(v)$, $\forall\ v \in H^1_0(\Omega)$ (7.4.2---5)

where $F(v) = \dfrac{1}{2}a(v,v) - (f,v)$ $a(u,v) = \displaystyle\int_{\Omega} \nabla u \cdot \nabla v dx$ $(f,v) = \displaystyle\int_{\Omega} fv dx$

It can be seen that both (V3) and (M3) involve the term a(u,v) and therefore it is essential for a(u,v) to be defined on H^1_0. Hence the Hilbert space is defined based on L_2.

The formulation (V3) is called the **weak formulation** of the classical problem (D3), and the solution of (V3) is called the **weak solution**. The advantage mathematically of the weak formulation (V3) is that it is relatively easy to prove the existence of a solution to (V3) while itøs hard to prove the existence of a classical solution to (D3).

It is evident that $V_h \subset H^1_0(\Omega)$. Hence, if u_h satisfies (V2), it will also satisfy (V3), and one can solve the problem based on the Galerkin method or Ritz method.

The solution u_h will satisfy

$$\left\| u - u_h \right\|_{H^1(\Omega)} \leq \left\| u - v \right\|_{H^1(\Omega)} \qquad \forall v \in V_h \qquad\qquad (7.4.2\text{---}6)$$

In other words, there is no other function in V_h with errors smaller than u_h when measured in the Hilbert norm.

7.4.3 Variational forms for the Neumann problem:

Differential equations can be divided into three categories in terms of boundary conditions: Dirichlet, Neumann and Mixed.

A Dirichlet boundary conditions fixes the boundary as stationary constants.

A Neumann boundary conditions does not specify the value for v on the boundary; instead it restricts its normal derivative on the boundary. A mixed boundary problem can be decomposed into Dirichlet and Nuemann problems and solved accordingly.

The problems described so far all have Dirichlet boundary conditions where $u=u_0$ on .

Now consider a Neumann boundary problem:

(D4) $-\Delta u + u = f$ in   (7.4.3---1)
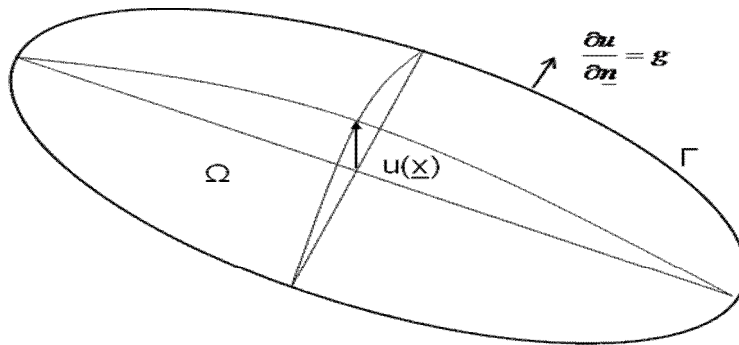
$$\frac{\partial u}{\partial \underline{n}} = g \qquad \text{on}$$

Fig 7.10 Boundary conditions in a 2D problem.

The variational forms in Hilbert space H ( ) for this problem are shown below

(V4) find u   H^1( )   such that a(u,v)=(f,v)+ <g,v> $\forall\ v \in H^{-1}(\Omega)$ (7.4.3---2)

(M4) find u   H^1( )   such that F(u)ÖF(v), $\forall\ v \in H^{-1}(\Omega)$ (7.4.3---3)

where $a(u,v) = \int\limits_{\Omega}[\nabla u \cdot \nabla v + uv]dx \qquad (f,v) = \int\limits_{\Omega}fvdx \quad \langle g,v\rangle = \int\limits_{\Gamma}gvds$

and $F(v) = \frac{1}{2}a(v,v)-(f,v)-\langle g,v\rangle$

The problem can then be discretised and solved with either the Galerkin method or the Ritz method.

The error estimate for this type of problem is

$$\left\| u - u_h \right\|_{H^1(\Omega)} \leq \left\| u - v \right\|_{H^1(\Omega)} \leq Ch \qquad \forall v \in V_h \tag{7.4.3---4}$$

where C is a constant and $C \propto \max\limits_{\Omega}(u'')$

7.5 Parabolic problems

7.5.1 Classical parabolic problems

The particular problem to be investigated in this work is the 3D heat conduction problem:

$$\rho C_p \frac{\partial T}{\partial t} + \nabla \left(- k \nabla T \right) = 0 \qquad\qquad (7.5.1\text{---}1)$$

$$- k \nabla T \bullet \underline{n} = H \left(T - T_0 \right) \qquad\qquad (7.5.1\text{---}2)$$

$$- k \nabla T \bullet \underline{n} = I + H \left(T - T_0 \right) \qquad\qquad (7.5.1\text{---}3)$$

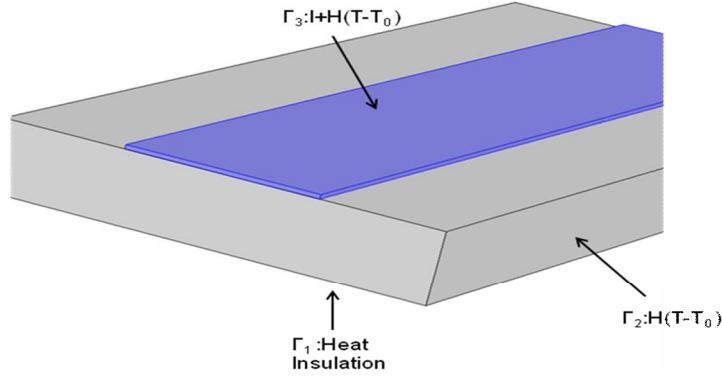The application of boundary values are shown in Fig 7.11

Fig 7.11 Boundary conditions in the case of the curing simulation

For consistency, rewrite the heat conduction problem of investigation in the following form:

$$(D5) \quad \lambda \dot{u} - div(\mu \nabla u) = f \qquad \text{in } \Omega \times I \qquad\qquad (7.5.1\text{---}4)$$

$$\mu \frac{\partial u}{\partial \underline{n}} = 0 \qquad\qquad \text{on } \Gamma_1 \times I$$

$$\mu \frac{\partial u}{\partial \underline{n}} = H(u - u^0) \qquad\qquad \text{on } \Gamma_2 \times I$$

$$\mu \frac{\partial u}{\partial \underline{n}} = I(\underline{x}, t) + H(u - u^0) \qquad \text{on } \Gamma_3 \times I$$

$$u(\underline{x}, 0) = u^0(\underline{x}) \qquad\qquad \underline{x} \in \Omega$$

where u=T, $\lambda = \rho C_p$, $\mu = k$

Here   represents the geometry of study, during the time interval t **I**.

---

u^0 is the initial value of the system. Neumann boundary conditions are accounted on $_1$, $_2$ and $_3$.

To solve this, discretize the problem not only by using FEM in the space, but in time also.

7.5.2 Fully discretization of parabolic problem in space and time.

Let V=H^1( )

Consider the variational formulation (V5)

$$(V5) \quad (\dot{u}(t),v) + a(u(t),v) = (f(t),v) \qquad \forall v \in V \quad t \in I \tag{7.5.2---1}$$

$$(u(0),v) = (u^0,v)$$

Now replacing the space V by a finite dimensional subspace V_h, upon discretisation we have the semi-discrete analogue:

(V$_h$5) Find u$_h$(t) such that

$$(\dot{u}_h(t),v) + a(u_h(t),v) = (f(t),v) \qquad \forall v \in V_h \quad t \in I \tag{7.5.2---2}$$

$$(u_h(0),v) = (u_h^0,v) \quad \forall v \in V_h$$

Here two common methods for full discretization, the **backward Euler method** and **Crank-Nicolson method** are considered.

In the backward Euler method $u_h^n \in V_h$, u(x, t$_n$) and n= 1,2,3í N. $V_h \subset H^1(\Omega)$ is sought as stated in the previous cases.

such that

$$(\frac{u_h^n - u_h^{n-1}}{k_n},v) + a(u_h^n,v) = (f(t_n),v) \qquad \forall v \in V_h \quad n = 1,2\cdots N \tag{7.5.2---3}$$

$$(u_h^0,v) = (u^0,v) \quad \forall v \in V_h$$

where k$_n$=t$_n$-t$_{n-1}$ is the local time step.

In the Crank-Nicolson method, $u_h^n \in V_h$ is sought such that

$$\left(\frac{u_h^n - u_h^{n-1}}{k_n}, v\right) + a\left(\frac{u_h^n + u_h^{n-1}}{2}, v\right) = \left(\frac{f(t_n) + f(t_{n-1})}{2}, v\right) \qquad \forall v \in V_h \quad n = 1,2 \cdots N \quad (7.5.2\text{---}4)$$

$$(u_h^n, v) = (u^0, v) \quad \forall v \in V_h$$

The fully discrete problems can be solved by substituting

$$u_h^n = \sum_1^M \varepsilon_i^n \phi_i \qquad \text{for } n = 1,2,3 \cdots N \tag{7.5.2---5}$$

Into (7.5.2---3) and (7.5.2---4) to discretise in space, as in the Galerkin method.

The problem needs to be solved for each time step n. A solver then iterates in n, therefore when solving for u^n, u^{n-1} is already solved, and thus a complete solution can be obtained after all iteration steps.

Suppose U_h is the solution for (7.5.2---2), then there's a constant C such that

$$\|u(t) - U_h(t)\| \le C \left(\max_{t \in I} k_n \left\|\dot{u}\right\| + \max_{t \in I} h^2 \|u(t)\|_{H^2(\Omega)} \right) \tag{7.5.2---6}$$

And we can conclude that the error is bounded by both the time step and the spatial element size.

And it can be concluded that the error is bounded by both the time step and the spatial element size.